University of Zurich[UZH]

Glacial dynamics on Disko Island, Greenland: Origin and Timing of erratic boulders deposition

GEO 511 Master's Thesis

Author
Sebastian Schaffner
17-735-119

Supervised by
Dr. Gerald Raab (gerald.raab@dal.ca)

Faculty representative
Prof. Dr. Markus Egli

31.01.2023
Department of Geography, University of Zurich

Abstract

This master's thesis focuses on the glacial dynamics in central-west Greenland, namely Disko Island. Enhanced interest in Greenland arises from the influence of global warming on the whole arctic region due to the phenomenon called Arctic Amplification. The high latitudes are affected more strongly than other parts of the globe. For a better understanding of how arctic amplification and the warming climate affect ice sheets like the Greenland Ice Sheet (GrIS), a look at past dynamics can be helpful.

For this master's thesis, 14 new ^{10}Be ages from erratic boulders (EBs) are reported from southern Disko Island in central-west Greenland. Previously only 3 EBs from Disko Island have been dated by Kelley et al. (2013). The here reported ages look to improve the deglaciation chronology of the Disko Bugt and provide key insights into the maximum thickness of the GrIS in the Last Glacial Maximum (LGM), with samples from different elevations.

Three of those 14 ages are located on the basaltic plateau of Disko Island. The three plateau samples yield ages of 104.1 ± 7 kyrs, 40.4 ± 2.8 kyrs, and 86.0 ± 5.9 kyrs. The lowest of these samples is located at 720 m.a.s.l., which puts a maximum thickness constraint of the GrIS during the LGM on this elevation, as they clearly predate the LGM.

Furthermore, the geochemistry of 28 sampled EBs is looked at to constrain the ice flow direction of the GrIS during the LGM. The origin of the samples from the western coast of Greenland supports an east-west flow direction with slight southern deflection around Disko Island during the LGM.

This master's thesis provides new results for forthcoming regional ice sheet modelling in the Disko Bugt with a maximum thickness constraint of 720 m.a.s.l. and an implication on flow direction through surface exposure dating and geochemistry analysis of EBs from southern Disko Island. With these findings, the reaction of the GrIS to past climate forcing can be better modelled, and therefore projections for future ice dynamics could be improved.

For future studies, the application of a second cosmogenic nuclide, to constrain shielding and erosional factors of exposure ages can be advised, especially when studying ages that could predate the LGM.

List of Abbreviations

AA	Arctic Amplification
AMS	Accelerator Mass Spectrometry
CAG	Continental Arc Granitoids
CCG	Continental Collision Granitoids
CEUG	Continental Epeirogenic Uplift Granitoids
CN	Cosmogenic Nuclide
EB	Erratic Boulder
ETH	Swiss Federal Institute of Technology Zurich
GeV	Giga Electron Volt
GrIS	Greenland Ice Sheet
IAG	Island Arc Granitoids
LGM	Last Glacial Maximum
LIP	Laboratory for Ion Beam Physics
LOI	Loss on Ignition
MCA	Multi-Channel Analyser
MORB	Mid-Ocean Ridge Basalts
POG	Post-Orogenic Granitoids
RRG	Rift-Related Granitoids
SED	Surface Exposure Dating
TAS	Total Alkali vs Silica
TCN	Terrestrial Cosmogenic Nuclide
UZH	University of Zurich
VAG	Volcanic Arc Granitoids
XRF	X-Ray Fluorescence

Table of Contents

1. Introduction

1.1. Motivation

Global warming has its influences in all possible spheres and regions. The arctic region however is reportedly warming much faster than the rest of the world. This is due to the process of Arctic Amplification (AA). The enhanced warming in the arctic region has various causes. One of the causes is the ice-albedo feedback of sea ice. With melting sea ice, the albedo of the region decreases drastically, which increases the amount of absorbed energy, which again increases sea ice melt (Previdi et al., 2021; Rantanen et al., 2022).

AA and the enhanced warming of the arctic lead to a big interest in the arctic region, and therefore also in the Greenland Ice Sheet (GrIS).

The GrIS is the largest currently existing ice sheet in the northern hemisphere and is projected to highly contribute to future sea-level rise (Søndergaard et al., 2020; Young & Briner, 2015).

To better understand the behaviour of the GrIS in the current climate, long-term perspectives are needed to improve our knowledge of all the main drivers for ice sheet dynamics for future projections (Hogan et al., 2016; Kelley et al., 2013; Kjær et al., 2022; Roberts et al., 2009; Young et al., 2020).

Cosmogenic nuclide analysis can provide a multi-millennial perspective into the dynamics of landscapes, as well as glaciers and ice sheets in the past. Knowing the age of landscapes or parts of them can help reconstruct the dynamics of the landscape. Depending on the scope of the research and the available material, one can choose from several cosmogenic nuclides (CNs) (Darvill, 2013; Ivy-Ochs & Kober, 2008). CNs can be produced either in-situ (in the mineral grain) or meteoric (in the atmosphere). For geochronological applications, such as the dating of exposure events, mostly in-situ produced CNs are studied (Cerling & Craig, 2003; Cockburn & Summerfield, 2004).

One of the most important factors for studying ice dynamics is the ice thickness. Thickness constraints for past glaciations of the western GrIS were previously inferred from trimlines. Here, exposure dating using CNs provides a possibility to directly date different elevation heights, and constrain the maximum elevation extent of the ice sheet (Roberts et al., 2009).

The regional ice sheet modelling done in Disko Bugt was chronologically and also geologically poorly constrained, at the time, when the deglaciation chronology relied mainly on radiocarbon dating (Roberts et al., 2009). Along with the thickness, the ice flow direction is also very important for the modelling of the ice flow. With increased knowledge about the geology of the deposited erratic boulders (EBs), the ice flow direction from point A (origin of EBs) to point B (deposition of EBs) can be incorporated into a model.

1.2. Regional Setting

The study site for this master's thesis is situated in central-west Greenland, on Disko Island. Disko is a small island in the Disko Bugt, the marine embayment where Jakobshavn Isbrae runs into. Jakobshavn Isbrae is the biggest outlet glacier of the Greenland Ice Sheet (GrIS), draining approximately 7 % of the inland ice (Kelley et al., 2013; Long et al., 2003). This brings an enhanced focus to this region when researching the retreat of the GrIS since the Last Glacial Maximum (LGM). Furthermore, the maximum extent of the GrIS out of the Disko Bugt is not clearly and fully researched yet (Hogan et al., 2016; Ingólfsson et al., 1990).

Disko Island receives around 400 mm of precipitation per year with a mean annual air temperature of -3.9 °C (Hansen et al., 2006; Humlum, 1998b). 75 % of all precipitation falls in the second half of the year from June to December (Humlum, 1998a). Disko is mainly composed of Cretaceous-Palaeogene tertiary basalts and sandstones (Kalsbeek & Christiansen, 1992; Weidick & Bennike, 2007), as can be seen in Figure 1.

How the GrIS exactly affected the island of Disko is not fully known (Raab, 2021). Southern and southeastern Disko Island were reportedly more affected by the inland ice during the last glaciation, than western and northern Disko, as crystalline erratics are most frequent south and east of Disko (Ingólfsson et al., 1990). Such EBs contain the possibility to be dated with ^{10}Be, due to their high quartz content. Both, the availability of quartz and the half-life of ^{10}Be being 1.387 ± 0.012 million years (Korschinek et al., 2010), support a ^{10}Be analysis for further research on the ice retreat on Disko Island.

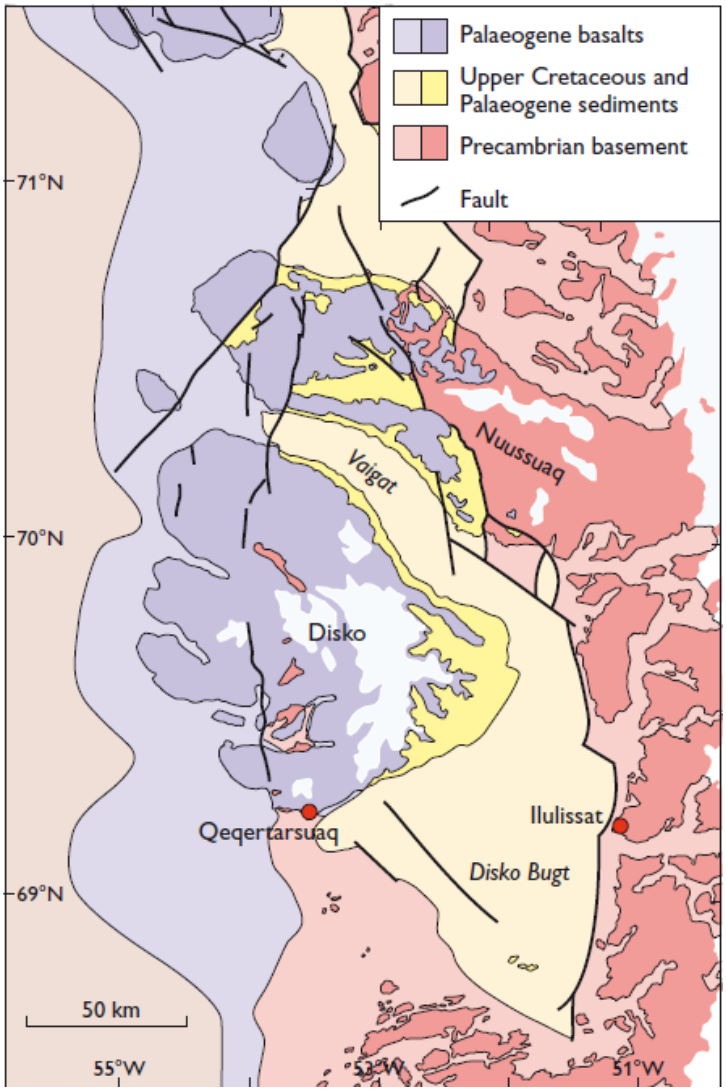

Figure 1: Bedrock geology of the Disko-Nussuaq area. Taken from Weidick & Bennike (2007).

The deglaciation of Disko Bugt has been summarised by Weidick & Bennike (2007) and then updated by Kelley et al. in 2013. The retreat of the ice sheet in western Greenland reportedly started around 13.8 kyrs B.P. on the western shelf. The ice then proceeded to retreat into Disko Bugt, where the small islands of Nunarssuaq were ice-free at 10.8 ± 0.5 kyrs, as shown in Figure 2. By 10.0 kyrs southern Disko Island was ice-free, which is supported by bivalves dating as well as ^{10}Be ages (Kelley et al., 2013). Central Disko Bugt was dated to be ice-free at 10.2 ± 0.1 kyrs. This age is only a minimum age due to the possibility of more unknown sediment below the drilling depth of this sediment core (Lloyd et al., 2005).

Many sites on northeastern Disko Bugt indicate deglaciation at 10.0 ± 0.2 kyrs, while southeastern Disko Bugt was probably deglaciated later at 9.2 ± 0.2 kyrs (Kelley et al., 2013; Weidick & Bennike, 2007).

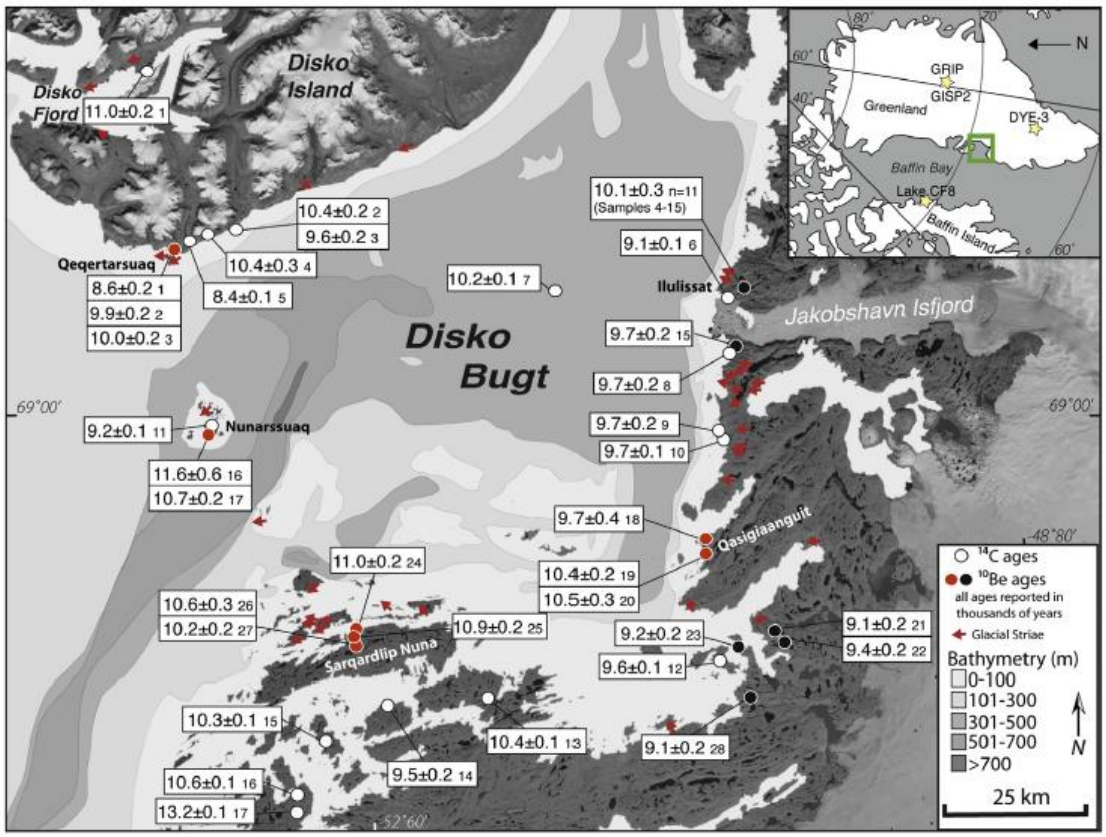

Figure 2: Summarised age reports for deglaciation chronology of Disko Bugt, directly taken from Kelley et al. (2013).

Having ^{10}Be ages, which constrain the deglaciation is more exact than radiocarbon dates of marine organisms because the time necessary for the marine organisms to colonize the ice-free seafloor is unknown. Therefore ^{10}Be ages report the timing of deglaciation more direct (Kelley et al., 2013).

1.3. Research Goals

The main goal of this master's thesis is to determine the deposition age and the origin of erratic boulders from both the southern slope and the basaltic plateau on southern Disko Island.

The first hypothesis set for my research is aiming at the deposition age. The sampled basaltic plateau on Disko lies above 800 m.a.s.l. Exploring the ages of EBs on this plateau might offer crucial insight into the question if the GrIS has completely overrun Disko during the LGM. Glacial remnants of older glacials deposited on the plateau would limit the ice thickness during the LGM.

H1: "The plateaus show remnants of glacial periods prior to the LGM."

The corresponding Null-Hypothesis H0 is: "The GrIS has overflown the whole of Disko and removed all remnants from previous glaciations."

The second part of my research, the origin determination, looks to see where these EBs originate from to constrain the flow direction of the GrIS.

H1: “The erratic boulders originate from the western mainland coast of Greenland.”

There the Null-Hypothesis H0 is: “The erratic boulders originate from local island sources.”

To be able to achieve these research goals and accept or reject the set hypotheses, my supervisor Dr. Gerald Raab sampled many EBs on the southern slope and the basaltic plateau of Disko. The samples were then sent to the University of Zurich, where I was able to start my master’s thesis with these rock samples. All the samples that were used and analysed in this thesis are displayed in Figure 3. They can be categorized into three sub-sections, one on the eastern slope including the plateau, one just above Qeqertarsuaq in the north, and a few samples on the western slope.

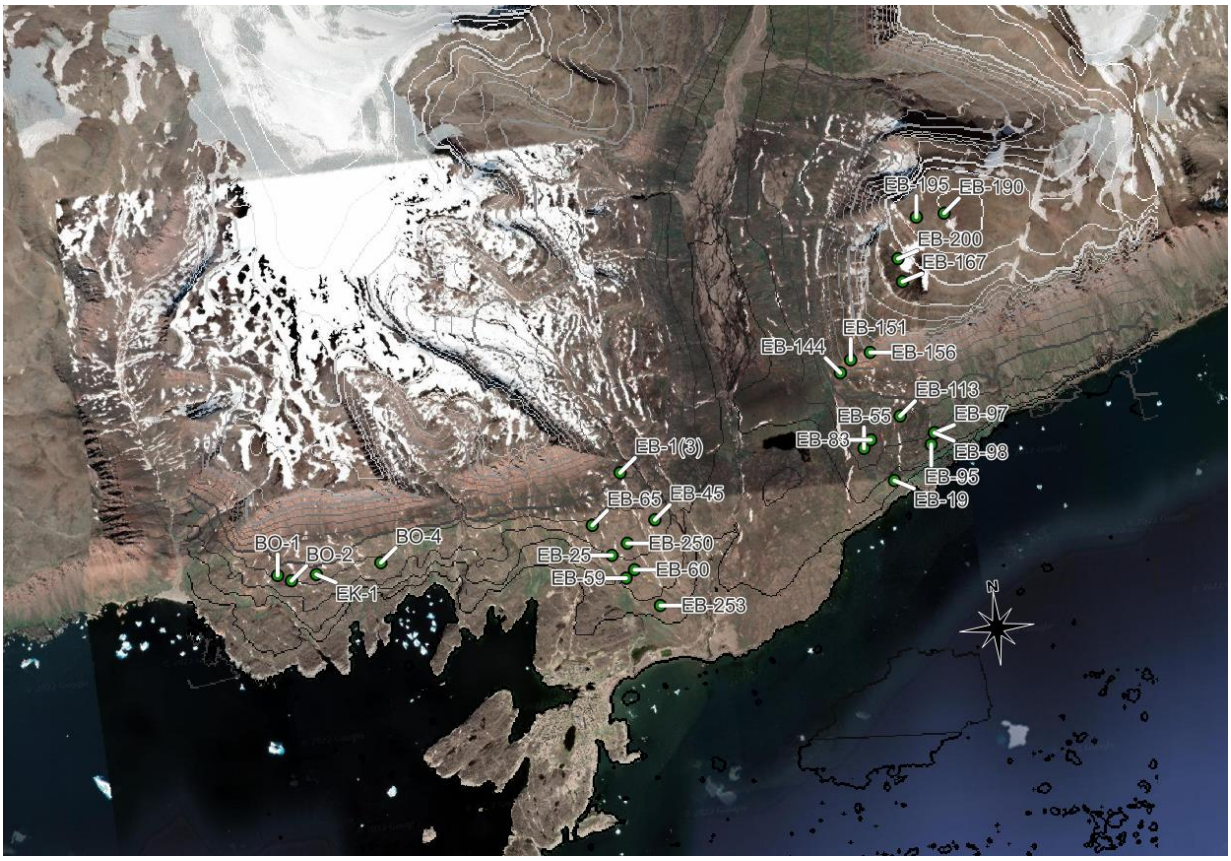

Figure 3: Southern Disko Island, 1:50'000. Position of samples used in this master’s thesis. Contour lines are imported to QGIS 3.22.11 from the Arctic DEM (Porter et al., 2022) and tiled Google Satellite Imagery for QGIS was put underneath.

1.4. Overarching Project

This master's thesis is embedded in a project by Dr. Gerald Raab, my supervisor. The project “Origin and timing of erratic boulders on Disko Island, Greenland: *Ice sheet dynamics & deglaciation history”*, is funded by the Swiss Polar Institute (SPI). The goal of this project is first to determine the age and source of origin of the EBs on southern Disko. Further the results of the samples on the basaltic plateau give crucial information to constrain the ice sheet thickness during the LGM, or even previous glaciations (Raab, 2021). All the samples mentioned in this master’s thesis were sampled and sent to Zurich by Gerald Raab in the

Summer of 2021, where I took them to the laboratory for the analyses at the start of my master's thesis.

2. Methods and Theory

2.1. Age Determination

2.1.1. ^{10}Be

Surface exposure dating (SED) with terrestrial cosmogenic nuclides (TCNs) is a modern tool for many applications (Cockburn & Summerfield, 2004; Ivy-Ochs & Kober, 2008). In this thesis, the focus is set on the terrestrial nuclide Beryllium-10. As explained in the introduction, ^{10}Be suits the location and the research goals, which is why this nuclide was chosen. ^{10}Be has several advantages to other nuclides, one being the very long half-life of 1.387 ± 0.012 million years (Korschinek et al., 2010), which enables studies over many time scales and another being its very well-constrained production rate.

The production of TCNs in general depends on the energy cosmic particles contain. For a CN to be produced, the cosmic particle has to contain more energy than the binding energy in the target nucleus. If the cosmic particle does not have enough energy, the target nucleus can not be split (Gosse & Phillips, 2001).

The energy a particle has is also influenced by Earth's magnetic field. The effect of the magnetic field on these high-energy particles is called rigidity and has been described by Gosse & Phillips (2001) as:

"The momentum of a particle per charge, or the product of the radius of curvature R due to the deflection of a charged particle through a magnetic field, B."

So only a cosmic particle with a rigidity that is high enough (>10 GeV) to pass through the magnetic field of Earth can reach the upper atmosphere and then interact with nuclei, producing secondary cosmic rays (Darvill, 2013). This highly influences the production rate, as fewer secondary cosmic rays, mean less CN production (Darvill, 2013; Gosse & Phillips, 2001). The cut-off rigidity is the minimum rigidity needed to enter the magnetic field (Gosse & Phillips, 2001). The cut-off rigidity drops below the necessary momentum to create cosmogenic nuclides at a latitude of 58°, which means that every particle which has enough momentum to create a cosmogenic nuclide can pass through the magnetic field. Above 58° latitude, the magnetic field no longer influences the production rates (Gosse & Phillips, 2001).

In Figure 4, the influence of the rigidity on cosmic particles is visualized (Darvill, 2013).

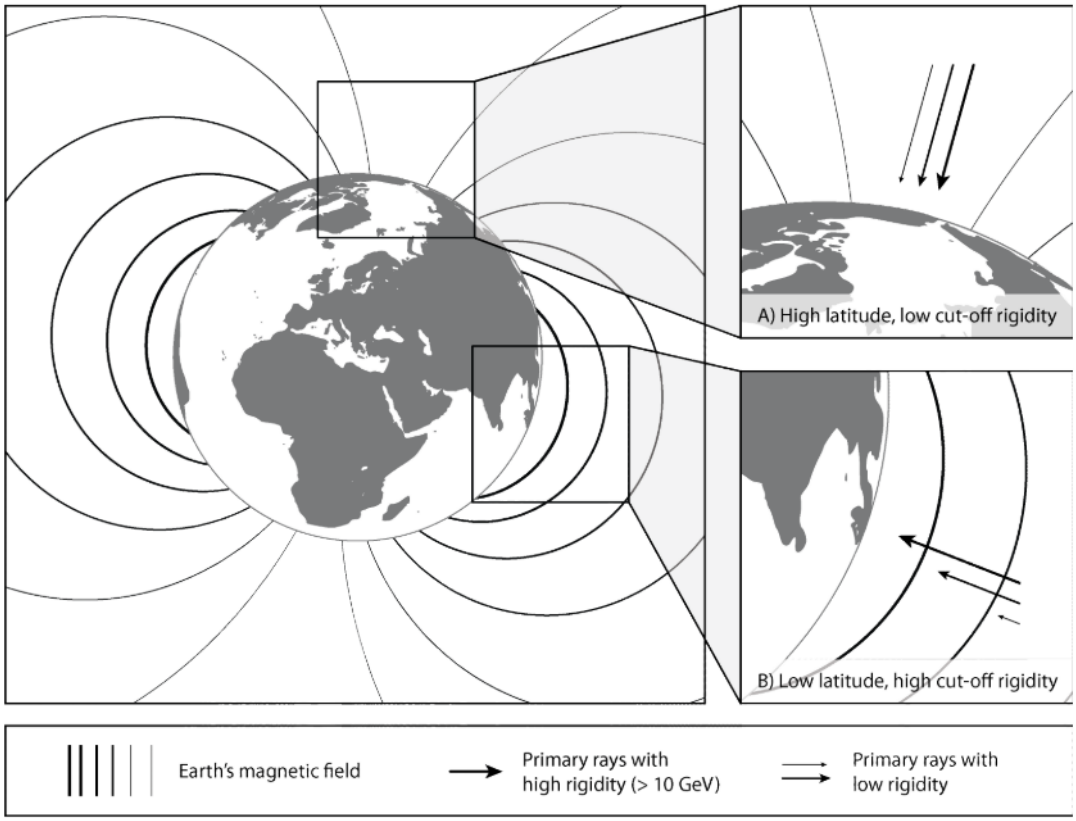

Figure 4: Incoming cosmic radiation being influenced by different latitudes, taken from Darvill (2013).

After the primary cosmic rays have entered the atmosphere, they collide with atoms in the upper atmosphere, forming secondary cosmic rays. The secondary cosmic rays then collide with other particles and further lose energy with every collision, as can be seen in Figure 5. The more energy the rays lose, the fewer CNs they can form. This attenuation of energy is mainly limited by the density of the material the cosmic radiation has to pass through (Gosse & Phillips, 2001).

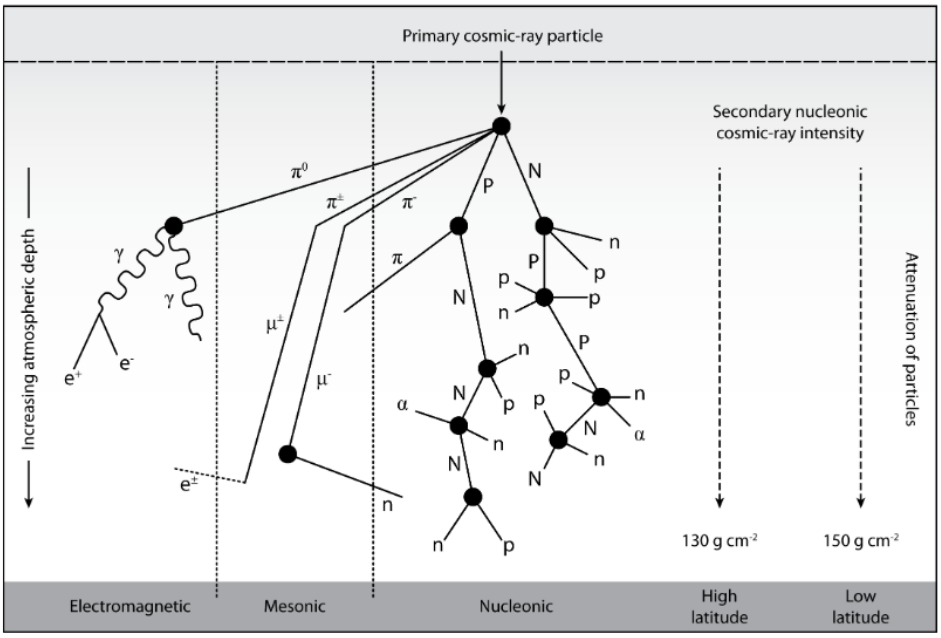

Figure 5: Cascading of secondary ray particles in the atmosphere by incoming primary cosmic rays, taken from Darvill (2013).

Secondary rays around the poles, where the magnetic field does not filter out the low-energy rays, have less average energy, so the attenuation by the atmosphere is more important at higher latitudes than at lower latitudes, where the rays must be highly energetic to pass through the magnetic field. This means that at higher latitudes the altitude is more important than at lower latitudes (Darvill, 2013).

^{10}Be can form either by spallation or by interaction with muons. Spallation is the process, where high-energy particles collide with a target nucleus and split light particles away, leaving a residual nucleus. The spallation can either happen in one step, where the nucleus is shattered into pieces by the collision or by the continuous splinting of nucleons from the nucleus until the energy of the incoming particles falls below the binding energy of the remaining nucleons in the nucleus. As illustrated in Figure 6, the production rate by spallation decreases very fast, with increasing penetration depth (Gosse & Phillips, 2001).

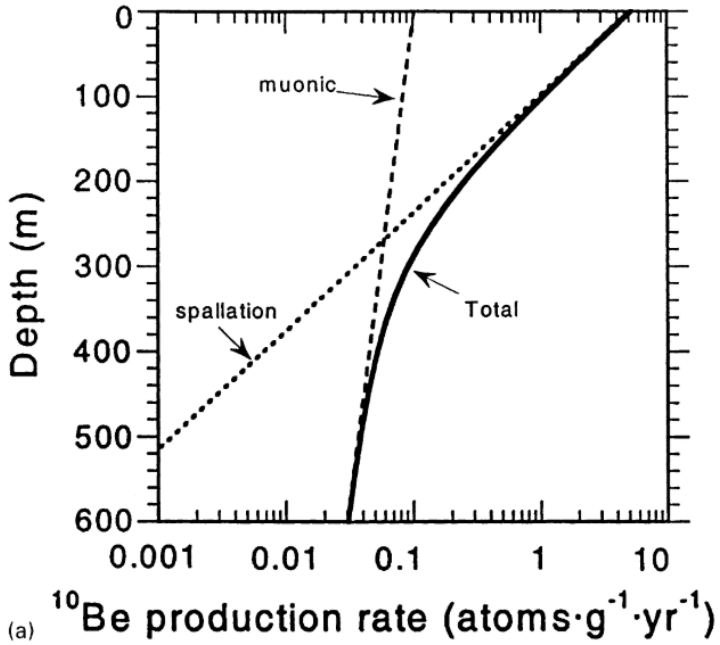

Figure 6: Variation of the production of ^{10}Be with depth in quartz arenite taken from Gosse & Phillips (2001).

Muons are secondary particles produced by high-energy particle interactions in the upper atmosphere. Muons are very short-lived, with a lifetime of 10^{-6} seconds, but the number of muons makes up for their rapid decay. Muons have low reactivity, which enables them to penetrate deeper into rocks (Gosse & Phillips, 2001). The impact of muons on the production of ^{10}Be is disputed. Balco et al. (2008) reported the muonic production to be 3.5 ± 0.5 % of the total ^{10}Be production. According to Marrero et al. (2016), muonic production only represents 1.4 ± 0.2 %. The muonic production is therefore strongly dependent on the measurement site. Just as plotted in Figure 6, muonic production is most important in deep samples. The samples in this master's thesis are all from the surface of the EBs and therefore the muonic component has a limited influence on the ^{10}Be production.

The production of ^{10}Be can happen with two target nuclei: ^{28}Si and ^{16}O. So, in-situ, the high-energy particle hits either a ^{28}Si or a ^{16}O nucleus and causes this to split into ^{10}Be and other products. This way the ^{10}Be forms inside of a sample and with time the ^{10}Be concentration enrichens.

2.1.2. Correction Factors

The production rate is not the same for different latitudes and different altitudes. Next to these two factors influencing the production factor, several more factors can change the ^{10}Be production rate and the concentration in the rocks, which had to be considered for my work, so the resulting ages can be looked at with some certainty. Some correction factors are better understood and easier to use than others.

2.1.2.1. Topographic Shielding

Topographic shielding describes the shielding of EBs from cosmic radiation by the surrounding topography. Topographic obstructions on the horizon, like mountains or hills, change the flux of incoming radiation (Darvill, 2013).

For the determination of the topographic shielding, one measures the angles at which the topography differs from an imaginary horizontal plane. This also includes the possibility of rocks lying on sloped surfaces. The deviation angle to the horizontal plane can then be used to calculate a correction factor, with which the ages can be corrected. Topographic obstructions usually lower the amount of ^{10}Be in a sample, as the EB does not receive the maximum potential radiation, so the age will be lower with increasing topographic shielding (Darvill, 2013; Gosse & Phillips, 2001).

2.1.2.2. Surface Shielding

Another factor, which can have a big influence on the age calculations is shielding by surface coverage, such as sand, soil, or snow. On the big EBs from Disko Island, snow cover is the most important factor, as there was no soil or sand on top of the boulders.

Snow adds a layer of more dense material to the attenuation of energy through the atmosphere. The cosmic radiation has to pass through the atmosphere and then additionally through a layer of snow until it can reach the target nuclides in the rock. This added layer reduces the amount of energetic particles for the production of cosmogenic nuclides (Darvill, 2013; Gosse & Phillips, 2001).

According to Figure 7 by Gosse & Phillips (2001) depending on the density and thickness of the snow cover, the age results can vary by up to 15 %.

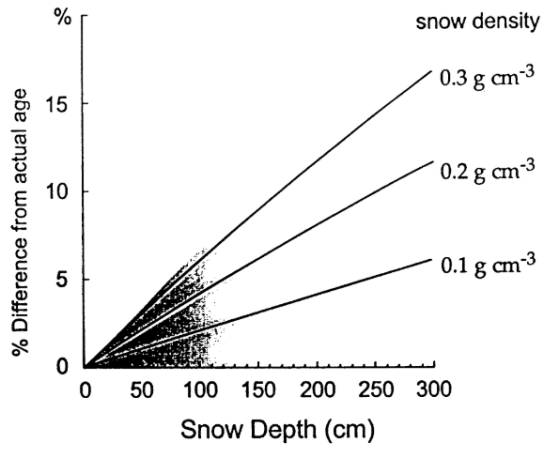

Figure 7: Effects of shielding by snow of different depths and densities for four months each year, taken from Gosse & Phillips (2001).

The observation of snow cover data on the sampled surfaces is very difficult and tedious and not available in most sites. With meteorological data, an assumption about snow cover can be made. The assumption does not resolve the uncertainty around snow cover but tries to limit it (Darvill, 2013). For approximation it is assumed that from the 300 mm (75 % of 400 mm) of precipitation falling between June and December, around 130 mm fall as snow (4 months rainfall and 3 months snowfall). So even if the whole 130 mm would cover the EB for four months every year, according to Figure 7, the percentual change of the samples' ages would be negligible at maybe one percent for dense (0.3 g cm^{-3}) snow.

2.1.2.3. Erosion of the Rock Surface

Erosion of the rock surface is another factor influencing the age results. Erosion gradually removes the top layer, where most of the cosmogenic nuclides are produced, which we want to measure. The eroded top layer operated as a surface shield, regarding the surface beneath. This leads to reporting younger calculated ages (Darvill, 2013).

Because the erosion rate is hard to determine, this factor often limits the applications of single nuclide analysis (Gosse & Phillips, 2001). To include the erosional effect, we report an appropriate age range with different erosion rates. Studies in Greenland have applied erosion rates of 0 – 10 mm per kyr (Dyke et al., 2014; Håkansson et al., 2007; Kelley et al., 2013; Søndergaard et al., 2020). The effect of different erosion rates on different age ranges will be discussed.

2.1.2.4. Pre-Exposure

Most factors named here have an influence on the results which cause younger ages. Pre-exposure, on the other hand, causes the ages to be higher than they actually are.

Pre-exposure is the result of a re-burial and re-exposure process of the sampled EB. If the EB has been exposed to cosmic radiation but has subsequently been buried again, the built-up CNs start to decay. If the burial time is too short for all CNs to decay, there will be a certain

amount of nuclides left in the rock, as new nuclides already form due to the new exposure. These left-over nuclides will also be measured with all the nuclides and therefore the age of the sample will be older because of the pre-exposure of the EB (Darvill, 2013). This is particularly important in the analysis of ^{10}Be ages, as ^{10}Be has a long half-life, allowing the decaying nuclides to remain in the sample even after a prolonged re-burial. To deal with pre-exposure, the optimal way would be to analyse two different CNs, which would lay bare a complex exposure history due to the different half-lives of the CNs. This can be done by adding ^{26}Al to the ^{10}Be analysis (Corbett et al., 2017).

2.2. Origin Determination

To determine the origin of the sampled erratic boulders, the focus was set on creating and analysing thin sections along with the chemical analysis with XRF.

2.2.1. XRF Spectrometry

X-ray fluorescence spectrometry is a method to gain information about the chemical composition of a sample. For XRF generally, the material can be in various solid forms. I worked with sample powder at UZH and glass beads at ETH.

The principle is to have x-rays interact with the sample. Matter can interact with x-rays either by absorbing or reflecting the energy. When the atoms in the sample absorb the x-rays, fluorescent radiation is produced, which is characteristic of each element. This is the most important process for XRF measurements. The fluorescence radiation is produced when x-rays hit electrons in the atom and cause them to get expelled out of the electron shell, as illustrated in Figure 8. The expelled electron leaves the atom in an excited state because the charges are not equal for a short period until the electron gets replaced by another electron from a higher energy shell. The replacement of the vacant electron spot by an electron of higher energy releases a characteristic photon, which is then measured. The collection of all the released photons gives the fingerprint and their intensity the concentration of the element, which is measured (Brouwer, 2010; El-Taher, 2012).

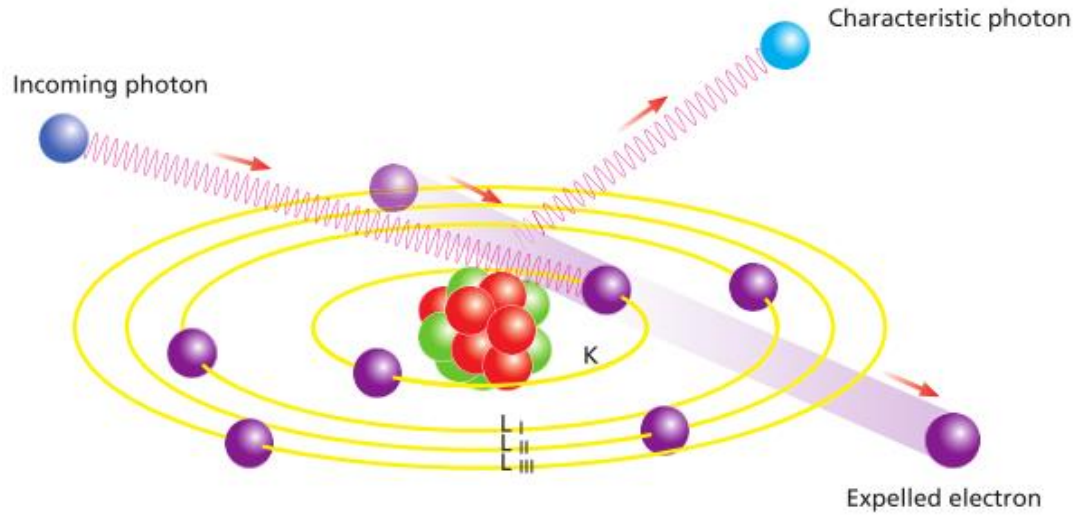

Figure 8: Ejection of an electron when hit by incoming x-rays, producing a characteristic photon. Taken from Brouwer (2010).

2.2.2. Thin Section Microscopy

Thin-section microscopy is a petrographic method, which enables us to look at the minerals, the composition, and the structure of the sample under an optical microscope. This can give us insights into the formation history of the sample. The determination of the minerals is done visually under the microscope, based on the optical and morphological characteristics of the minerals (Raith et al., 2011).

The identification of the minerals was done with the help of scripts by Stosch (2009) and Raith et al. (2011), and the Michel-Lévy interference colour chart (Michel-Lévy & Lacroix, 1888; Stosch, 2009).

3. Laboratory Work

3.1. Exposure Age Determination

From 47 collected erratic boulder samples, the 15 most representable samples for the three investigated areas on southern Disko Island were selected for exposure age determination. In detail, two samples were from the plateau in the west, three from the plateau in the north, and 10 from the vertical elevation profile in the east of the Qeqertarsuaq. The used samples are listed in Table 1. All samples were treated following the standard lab procedure by Egli et al. (2022) based on Kohl & Nishiizumi (1992). All the data of this lab work steps can be found in the appendix. The quartz content of sample EB-95 was below the ^{10}Be extraction requirement (< 30 g) and therefore was not further processed.

Table 1: Samples used for age determination.

Eastern site	Northern site	Western site
EB-19	EB-1(3)	EK-1 Drum
EB-144	EB-250	BO-2
EB-151	EB-253	
EB-156		
EB-55		
EB-98		
EB-167		
EB-190		
EB-195		

3.1.1. Sample Preparation

The selected 15 rock samples were crushed with a jaw crusher and sieved to obtain at least 400 g of the 0.25 – 0.6 mm fraction. This fraction was washed with distilled water and dried at 80 °C before the chemical cleaning of the samples. The excess material was stored.

3.1.2. Aqua Regia

To remove excess metals and organic material from the samples, 400 g of each sample was transferred into beakers and covered with aqua regia, until the acid reached 10 mm above the sample. Aqua regia is a mixture of one part 65 % nitric acid and 4.22 parts 32 % hydrochloric acid, known for dissolving various metals and all organics. EB-98 and EB-95 reacted the most out of all the samples, indicating more organics or different mineralogy. Most of the samples lost around 10 – 16 % of their original weight, except EB-98 and EB-95 which lost 31 % and 21 % respectively.

After stirring a few times, the samples were left to sit in the aqua regia under the fume hood overnight. The aqua regia was then washed off the samples with distilled water until they reached a neutral pH value. After drying them again at 80 °C, the weight was noted.

3.1.3. Froth Floatation

To remove feldspar from the mineral assemblages, the samples were treated with froth floatation. The samples were divided into 50 - 80 g large portions and put into Teflon bottles.

For froth floatation, we prepared two liters of 0.1 % dodecylamin solution. This was diluted with 18 L of distilled water. Before treating the samples with this mixture, the samples were put into 210 ml of 0.5 % hydrofluoric acid and kept in a fume hood for half an hour, where the samples were swirled two to three times.

After treating the samples with hydrofluoric acid, the samples were rinsed with distilled water and mixed with five drops of eucalyptus oil. We treated the samples with HF first, to create a fresh surface to take advantage of the different wetting characteristics and surface properties of feldspar and quartz, to separate these two minerals (Sulaymonova et al., 2018). The eucalyptus oil was added to stabilize the bubbles in the carbonated dodecylamin solution, which bound the feldspar (Purdue University, 2007).

The floatable parts were decanted into a beaker and after a few repetitions of the feldspar removal, the quartz-rich fraction was washed with distilled water and put in a new clean beaker.

After drying the sample at 80 °C in the oven, the mass of the quartz-rich fraction was weighed and noted (Egli et al., 2022). The floating feldspar was put in storage.

3.1.4. Hydrofluoric Acid Leaching

To be able to use the quartz for in-situ ^{10}Be extraction, the quartz needs to be pure. Additionally, the sample must be free from all other minerals, and the meteoric ^{10}Be from the surface of quartz (Goehring et al., 2008). To obtain clean quartz, 40 – 100 g of the samples were leached with a 4 % HF solution and put on a shaker for five days at 170 rounds per minute (rpm). The volume of the HF solution was dependent on the mass of the sample, according to Table 2.

Table 2: Volume of MQ-H_2O and 40 % HF necessary to leach the samples with 4 % HF for the amount of sample used, taken from Egli et al. (2022).

Sample mass (g)	Volume of MQ-H_2O (ml)	Volume of 40 % HF (ml)
90-100	500	50
80-90	450	45
70-80	400	40
60-70	350	35
50-60	300	30
40-50	250	25

EB-1(3) had the lowest mass with 41 g, and therefore only 250 ml of Milli-Q H_2O and 25 ml of 40 % HF were used.

During the leaching of the sample in these five days, the speed of the shaker was increased three to four times to 210 rpm for five minutes, to ensure good mixing. After the long leaching period, the samples were rinsed with Milli-Q H_2O two to three times.

This leaching process was repeated another two times to ensure pure quartz.

After leaching, the samples were rinsed with Milli-Q H_2O to neutral pH. Then the sample was rinsed with Milli-Q H_2O another ten times at least, just to be sure, that there was no acid and no potential isobars left in the sample. The samples had to be dried again on the hot plate at 80 – 100 °C and then weighed.

3.1.5. Quartz Decomposition

In this step, a process blank was added to the workload, which functioned as a check for lab cleanliness. The blank had a concentration of 1001.1 mg ^{9}Be per L and a density of 1.011 g cm^{-3}, produced by the company Scharlau. This blank followed all the same target chemistry steps.

So now that the samples were pure quartz, the focus was set to the ^{10}Be in the mineral structure. For this, the quartz needed to be decomposed. Exactly 30 g of the samples were put into a beaker, except for sample EB-1(3), which only had 26.8 g left after the leaching. 0.30 ml of ^{9}Be carrier solution with a concentration of 1 g ^{9}Be per L was added to the sample. For digestion 200 ml of 40 % hydrofluoric acid was added in two steps a day apart (100 ml + 100 ml). The beakers were then heated without the lid at 100 °C until the samples were completely dry. To the formed fluoride cake, we added ten ml of Milli-Q H_2O and heated it in a closed beaker at 80 °C for one hour.

The solids and liquid were transferred in a 15 ml centrifuge tube with a pipette and centrifuged for five minutes at 3000 rpm. The supernatant after centrifuging was put into a 50 ml clean centrifuge tube and the volume was topped up to ten ml with Milli-Q H_2O, so that every sample had the same volume. After adding exactly 13.2 ml of 32 % HCl, the sample was shaken shortly on the shaker and left for an hour for homogenization.

3.1.6. Anion Exchange Column

The anion exchange column is primarily done to remove excess Fe. The samples could have still contained a lot of unwanted Fe, and this had to be taken care of before separating and collecting the different elements in the cation exchange column. The iron is unwanted in the sample, as it precipitates over a very wide pH range and therefore would also precipitate during the precipitation of Be. High amounts of Fe in the Be fractions in the samples would possibly

lead to high errors in the exposure age due to interference with the measurements (Ochs & Ivy-Ochs, 1997).

First, in the anion exchange column, the samples were loaded into a column with a Biorad 1-X8 100-200 mesh. Before the samples were run through, the resin was cleaned with twice 5 ml of 0.3M HCl. The resin was then conditioned with three times 2 ml of 6M HCl.

Then the sample was loaded into the column and washed through with three times 2 ml of 6M HCl. The sample and the 6 ml HCl were then collected in a new and clean Teflon beaker.

After collecting the sample, the columns had to be cleaned for next use again, this was done by cleaning the resin with 5 ml of 0.3M HCl twice and then once putting 2 ml of Milli-Q H_2O through and filling it up with Milli-Q H_2O in the end.

The sample then was dried at 120 °C. After that, the sample is again heated for two hours, to 60 °C, with the addition of 4 ml of 0.4M Oxalic acid. Every half hour we replaced evaporated water with 1 ml of Milli-Q H_2O.

After cooling, the liquid was transferred into a 15 ml centrifuge tube and the volume of the samples was adjusted to the same volume of 4 ml with Milli-Q H_2O.

3.1.7. Cation Exchange Column

The cation exchange column allows the selective removal of elements, mainly Be in this case, or Al for further research. This was done by conditioning a resin with oxalic and nitric acid on the base of elution experiments. The mesh used for these columns was the Biorad AG50W-X8 200-400 mesh.

For simplicity, a summary is provided in Table 3. In Table 3 we see the different steps of adding different acid solutions and samples into the columns.

Table 3: Procedure for cation exchange column, taken from Egli et al. (2022).

Volume	Reagent	Collect in	Why
2 + 3 ml	5M HNO3	100 ml PP beaker	Clean the resin
2 + 3 ml	Milli-Q H2O		remove HNO3 from the resin
2 + 3 ml	0.4M Oxalic Acid		condition the resin
After the cleaning and conditioning, we load the sample in the cation exchange column. Before we centrifuged the sample for 5 minutes at 3000 rpm, to be able to transfer only the supernatant into the column. The last drop gets left in the tube because it does not contain Beryllium.			

Load Sample		15 ml CT for Al	Collect Al
1 + 1 ml	0.4M Oxalic Acid		
5 + 5 ml	0.4M Oxalic Acid	100 ml PP beaker	Elute Fe, Ti, and leftovers of Al
1 + 2 ml	Milli-Q H2O		Remove oxalic acid from the column
2 + 2 + 4 ml	0.5M HNO3	15 ml CT for Na	elute Na
3 + 3 + 5 ml	1M HNO3	15 ml CT for Be	elute and collect Be
2 + 4 ml	1.2M HNO3	15 ml CT for leftovers	collect leftovers
5 + 5 ml	5M HNO3	100 ml PP beaker	clean resin
2 + 2 ml + full	Milli-Q H2O		remove acid (pH paper for check)

In the end, as in the anion exchange columns, the columns were filled with Milli-Q H_2O for storage.

3.1.8. Precipitation and Calcination

To precipitate the Be out of the collected solution, we added 25 % NH_4OH drop by drop, to reach a pH of 8.5 – 8.7, where Be precipitates.

During this addition, the solution was tested multiple times for the pH value, which had to be between 8.5 and 8.7 at the end, which is the range for Be to precipitate.

A higher value than a pH of 10 would make the $Be(OH)_2$ dissolve again. Some samples needed more drops, but most of the samples needed around 30 drops. After waiting for homogenization of the sample, it was centrifuged at 3000 rpm for ten minutes to separate the $Be(OH)_2$ gel from the remaining liquid, which was transferred to waste. The $Be(OH)_2$ gel was mixed with a few drops of Milli-Q H_2O and transferred to a quartz crucible.

The $Be(OH)_2$ gel in the crucible was then dried on the hotplate at 70 °C to evaporate the excess water. The remaining $Be(OH)_2$ gel was dried overnight at 120 °C. The crucible was closed with a lid and calcinated in a quartz holder in the muffle oven at 200 °C for two hours and 850 °C for one more hour.

These crucibles with the calcinated BeO were then sent to the Laboratory for Ion Beam Physics (LIP) at the ETH. The $^{10}Be/^{9}Be$ ratios were measured with the MILEA AMS system at the LIP. The results were normalized to in-house standards S2007N and S2010N with nominal values of $^{10}Be/^{9}Be = 28.1 \times 10^{-12}$ and $^{10}Be/^{9}Be = 3.3 \times 10^{-12}$. Both, S2007N and S2010N have been calibrated to the primary standard ICN 01-5-1, by Nishiizumi et al. (2007) with a nominal $^{10}Be/^{9}Be$ value of 2.709×10^{-11}. The reported 1σ errors of the in-house standards are 2.7 % for S2007N and 2.4 % for S2010N (Christl et al., 2013).

The ages are corrected to the sample preparation blank and the long-term average blank, which have $^{10}Be/^{9}Be$ ratios of 0.016×10^{-12} and 0.0150×10^{-12}, respectively.

Reported internal measurement errors of ^{10}Be at/g were between 2.9 and 6.3 %, including the AMS standard error.

The ages were calculated with the CRONUS-Earth online calculator, version three (http://hess.ess.washington.edu, last accessed on 28.11.2022) (Balco, 2017), using the LSDn scaling model. This is a neutron monitor-based scaling model, which fits best at high latitudes, in comparison to other scaling models (Lifton et al., 2014). A rock density of 2.65 g cm^{-3} was chosen, and the ages were corrected for topographic shielding.

3.2. Origin Determination

3.2.1. Whole Rock Chemistry

For the determination of the origin of the erratic boulders, 28 boulders were selected, including the 15, which have already been used for exposure dating. The additional 13 samples were chosen according to their location on Disko Island so that every site is represented by four or more samples for the origin determination.

The samples were measured twice with XRF, once at the UZH and once at the ETH. At UZH the samples were milled to a fine powder and then measured. At ETH we used a different measurement technique, glass beads. The second measurement with glass beads was done because this technique increases the homogeneity of the sample and does not have to deal with sample particle size effects (Kawabata et al., 2005; Krusberski, 2010).

Both, at UZH and at ETH, the Loss on Ignition (LOI) was calculated. This was done to correct the element contents for volatiles and organic contents in the sample. At UZH part of the sample was used for LOI calculation and another part of the sample was measured with XRF. At ETH, on the other hand, the samples underwent the LOI step, and then the same part of the sample was melted into a glass bead, which was later measured.

3.2.1.1. XRF at UZH

For each of the samples selected, one of the remaining hand pieces was taken to the jaw crusher at UZH again and crushed. Some samples showed small amounts of weathering on

the surface, primarily lichen. Because of the coarseness of the rock crusher, I was not able to remove those weathered parts and took the pieces as they were, as can be seen in Figure 9. After crushing, 10 g were put into a wolfram beaker, along with two little wolfram balls. The closed beakers were then put into a horizontal mill, two samples at a time, and shaken at a speed of 30/s for approximately 15 minutes. The balls inside milled the sample down to less than 63 μm in these 15 minutes. Four samples were not fine enough at first measurements and had to be re-milled before they were correctly measured.

Figure 9: Visible weathering on one of the samples before XRF preparation. Picture by Sebastian Schaffner.

For LOI, 2 g of the milled material for XRF was taken and put into ceramic crucibles. The crucibles had to be exactly weighed before with an analytical scale, without the sample, and afterward, with the sample. After measuring and noting the weights, the crucibles were heated in a muffle oven at 550 °C for six hours.

After the crucibles were cooled in a desiccator, the crucible, with the sample inside, was weighed again. The difference between pre-heated and post-heated weight was then calculated and noted as the LOI (%), according to Equation 1.

Equation 1: Calculation of the LOI.

$$100 - \left((m_{total} - m_{crucible}) \div m_{sample} \times 100 \right)$$

For the XRF measurement, the samples were put into plastic cups, with a thin plastic foil on the bottom. Approximately 5 g of the sample was put into a plastic analyser cup and then measured in a Multi-Channel-Analyser (MCA) at UZH. The MCA is calibrated every week with a glass disc named "*coltide energy calibration disc mcacal*". The lab technician at UZH could

unfortunately not provide any specifications on this calibration, further information is not available. The global recalibration of the MCA is done with two discs “FLX-SP1” and “FLX-SP2”, which are reference materials by FLUXANA. The samples are measured with a control called “NCS DC 73326”.

3.2.1.2. XRF at ETH

Sample Basalt-Mix-2, which was not milled at UZH, was milled at the Institute for Geochemistry and Petrology of ETH Zurich, in a disk mill with an agate shatter box according to the standard laboratory procedure (Dietrich et al., 1984; Nisbet et al., 1979).

At the analytical lab of the Institute for Geochemistry and Petrology at ETH, the samples went through a different process for the XRF measurements.

After drying the samples again overnight in a muffle oven at 110 °C, 1.5 g of the samples were weighed into clean crucibles with an analytical scale. The weight of the crucible was weighed and noted before. The crucibles were then put into the muffle oven at 850 °C for two hours, except Basalt-Mix-1 and Basalt-Mix-2, which were put in at 1050 °C. After these two hours, the samples cooled down for ten minutes before they were weighed again. Here again with the difference in weight before and after, the LOI was calculated according to Equation 1.

After the LOI step, the samples were mixed with a flux in the exact ratio of 5:1, flux to sample. The flux consists of $Li_2B_4O_7D$(i-lithium tetraborate) and was added to lower the melting point of the mixture so that the powder melts at 1150 °C. Then this mixture was homogenized in an agate mortar and put into a clean platinum crucible. This platinum crucible and the casing dish were put into the Claisse Flux M4 where a predefined melting program was started. The Claisse Flux M4 melted the sample-flux-powder mix and poured the melt into the platinum casing dish, in which the bead was cooled down. After the cooling steps, the sample was taken out and tapped out of the casing dish onto a clean sheet of paper. The storage case was put on top of the glass bead, to avoid touching the side of the measurement. This finished glass bead was then measured with Axios, a wavelength dispersive x-ray spectrometer by PANalytical. Axios is calibrated based on around 35 certified reference materials for igneous and metamorphic rock compositions (Institute for Geochemistry and Petrology at ETH Zurich, 2022).

3.2.2. Thin Section Microscopy

For the second part of the origin determination, thin section microscopy was chosen, to characterize the petrology of the rock samples. Both, the preparation, and the microscopy parts were done at the Institute for Geochemistry and Petrology at ETH Zurich.

All 28 samples which were chosen for origin determination were used for this step. In the sawing room, the handpieces had to be sawn into a block with the exact extents of 33 x 22 x 15 mm. During this sawing, EB-200 and EB-156 broke because they had too small of a

handpiece, for them to be used, which is the reason that only 26 thin sections were created. The handpieces for these two samples can be seen in Figure 10 and Figure 11.

The 26 sawn rock pieces were then handed in at the workshop, where the samples were glued to a microscopy glass and sanded to a thickness of 30 µm. The finished thin sections had to be picked up and could then be brought to the microscope.

Figure 10: Broken handpieces of EB-200 during sawing.

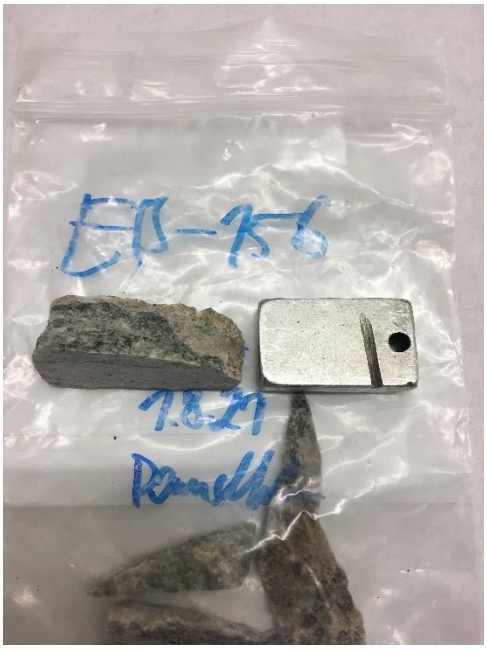

Figure 11: Biggest handpiece of EB-156 during sawing, next to the model of the required size of a thin section block.

The thin sections of the 26 samples were analysed and commented with an optical microscope, with a camera, which was connected to ZEN 3.5 (blue edition), a microscopy software by Zeiss, where the annotations for the minerals could be done on the snapshot directly. The figures of thin sections are snapped at a magnification of 2x in the microscope.

4. Results

4.1. ^{10}Be Ages

The sample information from the field and the measured ^{10}Be at g^{-1} (x10^4), which were put into the calculator, can be seen in Table 4. The ages in Table 4, do not include any errors or uncertainties.

Table 4: Input Data table for the CRONUS-earth calculator and the calculated ages for the samples without erosion correction, using the LSDn scaling scheme by Lifton et al. (2014), internal measurement errors are given in percentage of age change.

Field sample name	Latitude (°N)	Longitude (°W)	Elevation (m.a.s.l)	Shielding factor	Thickness (cm)	^{10}Be (at/g) (x10$^{4)}$	Err ^{10}Be (at/g) (x10^4)	Int. Error (%)	Age (yr) e = 0 mm/kyr
EB-190	69.2895	-53.4252	848	0.9999	1.6	106.1221	3.1232	2.94	104109
EB-195	69.2894	-53.4326	830	0.9442	1.5–2.0	38.9135	1.3702	3.52	40442
EB-167	69.2835	-53.4381	720 (718)	0.9906	2	77.1116	2.5363	3.29	85957
EB-156	69.2773	-53.4488	502 (559)	0.9963	1	7.4083	0.3348	4.52	9200
EB-151	69.2768	-53.4541	432	0.9955	1	7.2395	0.3630	5.01	10159
EB-144	69.2757	-53.4573	323	0.9782	1.5	4.1783	0.2285	5.47	6684
EB-55	69.2684	-53.4534	174	0.8159	2	5.3148	0.2599	4.89	11795
EB-98	69.2691	-53.4344	139	0.9876	3	5.4764	0.2728	4.98	10480
EB-19	69.2650	-53.4464	85	0.9971	1.5–2	4.7529	0.2454	5.16	9396
EB-1(3)	69.2687	-53.5183	264.2 (315)	0.9757	2	5.8708	0.3069	5.23	9473
EB-250	69.2621	-53.5184	166	0.9971	1.6–2	5.5179	0.2701	4.90	10082
EB-253	69.2559	-53.5116	91	0.9989	1.5–2	5.5101	0.3459	6.28	10840
EK-1 Drum	69.2625	-53.6012	213	0.8789	2.5	5.6188	0.2720	4.84	11182
BO-2	69.2621	-53.6079	200	0.8812	2	5.7374	0.2840	4.95	11504

EB-144 yields the lowest age with 6.7 ± 0.5 kyrs (± external errors for the scaling model). As the samples next to EB-144 are more than three thousand years older, this sample is an outlier.

The samples next to EB-144 locally are EB-156 and EB-151, which yield ages of 9.2 ± 0.7 and 10.2 ± 0.8 kyrs respectively. Other samples on the eastern slope are EB-190, EB-195, and EB-167, which are located on the plateau. These three samples have radically different ages than the others with EB-190 yielding the oldest age of 104.1 ± 7.0 kyrs. EB-195 results in 40.4 ± 2.8 kyrs and EB-167 yields an age of 86.0 ± 5.9 kyrs. The lowest elevation of these three samples is EB-167 at 720 m.a.s.l. With lower elevation on the eastern slope the samples EB-55, at an age of 11.8 ± 0.9 kyrs, EB-98 yielding an age of 10.5 ± 0.8 kyrs, and EB-19 with 9.4 ± 0.7 kyrs yield much lower ages again than the samples on the plateau.

Farther to the west in the central sample site, samples EB-1(3), EB-250, and EB-253 are located. These samples yield ages of 9.5 ± 0.8 kyrs, 10.1 ± 0.8 kyrs, and 10.8 ± 0.9 kyrs, respectively.

The westernmost samples EK-1 Drum and BO-2 yield ages of 11.2 ± 0.9 kyrs and 11.5 ± 0.9 kyrs.

The samples on the eastern slope, excluding the samples on the plateau, average 9.6 ± 0.9 kyrs. The northern samples show an average of 10.1 ± 0.8 kyrs and the western samples average 11.3 ± 0.7 yrs. The ages ± external errors are listed in Table 5.

Table 5: Ages (kyrs) for all the samples ± ext. Error.

Sample Name	Age (kyrs) ± ext. error
EB-144	6.7 ± 0.5
EB-156	9.2 ± 0.7
EB-19	9.4 ± 0.7
EB-1(3)	9.5 ± 0.8
EB-250	10.1 ± 0.8
EB-151	10.2 ± 0.8
EB-98	10.5 ± 0.8
EB-253	10.8 ± 0.9
EK-1 Drum	11.2 ± 0.9
BO-2	11.5 ± 0.9
EB-55	11.8 ± 0.9
EB-195	40.4 ± 2.8
EB-167	86.0 ± 5.9
EB-190	104.1 ± 7.0

4.2. XRF Data

The glass beads measured at ETH, have a few advantages compared to the powder method used at UZH. Glass beads eliminate the particle size effect, as well as the mineralogical matrix effect. Another advantage is the homogeneity of the sample in the glass bead because of the previous melting and mixing (Kawabata et al., 2005; Krusberski, 2010). Because of this increased accuracy of XRF measurements with the glass beads, only these results were chosen to be looked at for the geochemical analysis.

At the time of measurement of the glass beads, the Ni values could not be correctly measured and therefore these values were not used in the analysis.

The XRF results were handled with the GCD-Kit by Janoušek et al. (2006) in R. Simple summary statistics can be seen in Figure 12, where boxplots for all major elements are shown. The values for the elements in the boxplots are given in weight percentage (wt%). All raw measurement results are available in the appendix.

The SiO_2 values in the first boxplot show a range from 45.94 wt% up to 94.15 wt%. There are five obvious outliers with much lower or higher SiO_2 values than the rest of the dataset. The outliers are EB-95 (51.74 wt%), EB-200 (94.15 wt%), BO-1 (46.79 wt%), and the Basalt-Mixes

1 & 2 with 45.94 and 46.4 wt% SiO_2 respectively. The other samples plot between 65 and 76 wt% SiO_2. The mean of the data set is 67.84 wt% SiO_2.

EB-95, BO-1, and the two Basalt-Mix samples also show clear outliers in the TiO_2, FeO_t, MnO, and MgO plots, where they have significantly higher values than the rest of the dataset.

Other mentionable outliers in individual plots are EB-98 with low Al_2O_3 (5.57 wt%) and high CaO value (12.43 wt%) and EB-200 with the lowest Al_2O_3 value (1.82 wt%) of the dataset.

The K_2O values are widely spread between 0.24 and 5.98 wt%, with the mean at 2.52 wt% and a standard deviation of 1.65.

Other variables are constrained to a rather small range of values, such as TiO_2, with a standard deviation of 0.13, when excluding the outliers, and 0.88 with the outliers in the calculation.

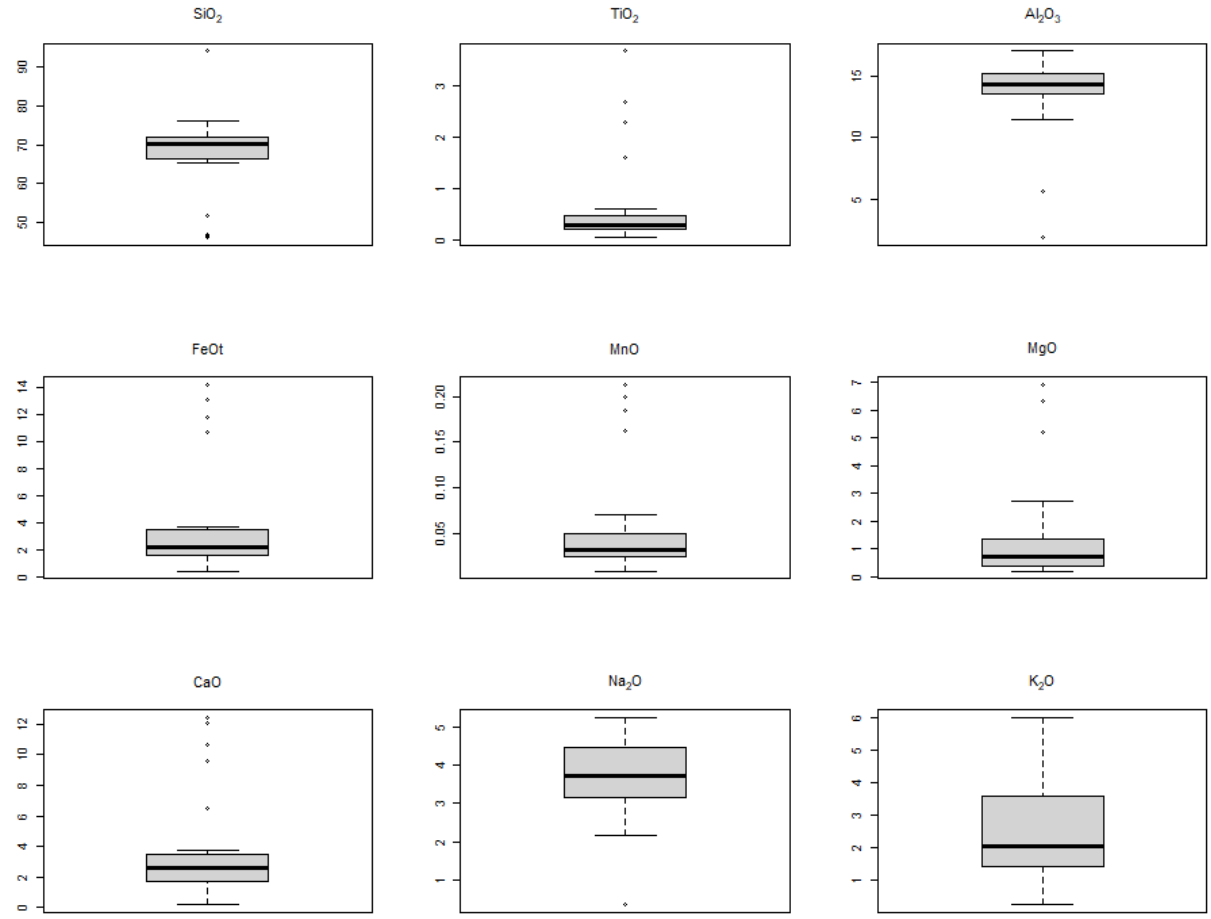

Figure 12: Summary boxplots for the major elements in the samples. Values are in wt%. Exported from GCD-Kit.

The samples which were not plutonic were excluded for further classification and analysis. This was the case for the basaltic samples BO-1 and the Basalt-Mixes, and also for EB-98, which was classified as a sandstone, and EB-200, a quartz vein.

The samples were classified with the Total Alkali vs Silica (TAS) plot based on Middlemost (1994). The classification can be seen in Figure 13. For re-assuring and comparison, another

classification based on de la Roche et al. (1980) was done, visible in Figure 14. In both classification plots, some samples have been assigned their names for easier detection of the samples outside of the cluster. The samples were coloured and symbolized according to their location on Disko Island. The blue triangles are the samples in the north of Qeqertarsuaq, the black squares are from the east of Qeqertarsuaq and the green squares are from the west.

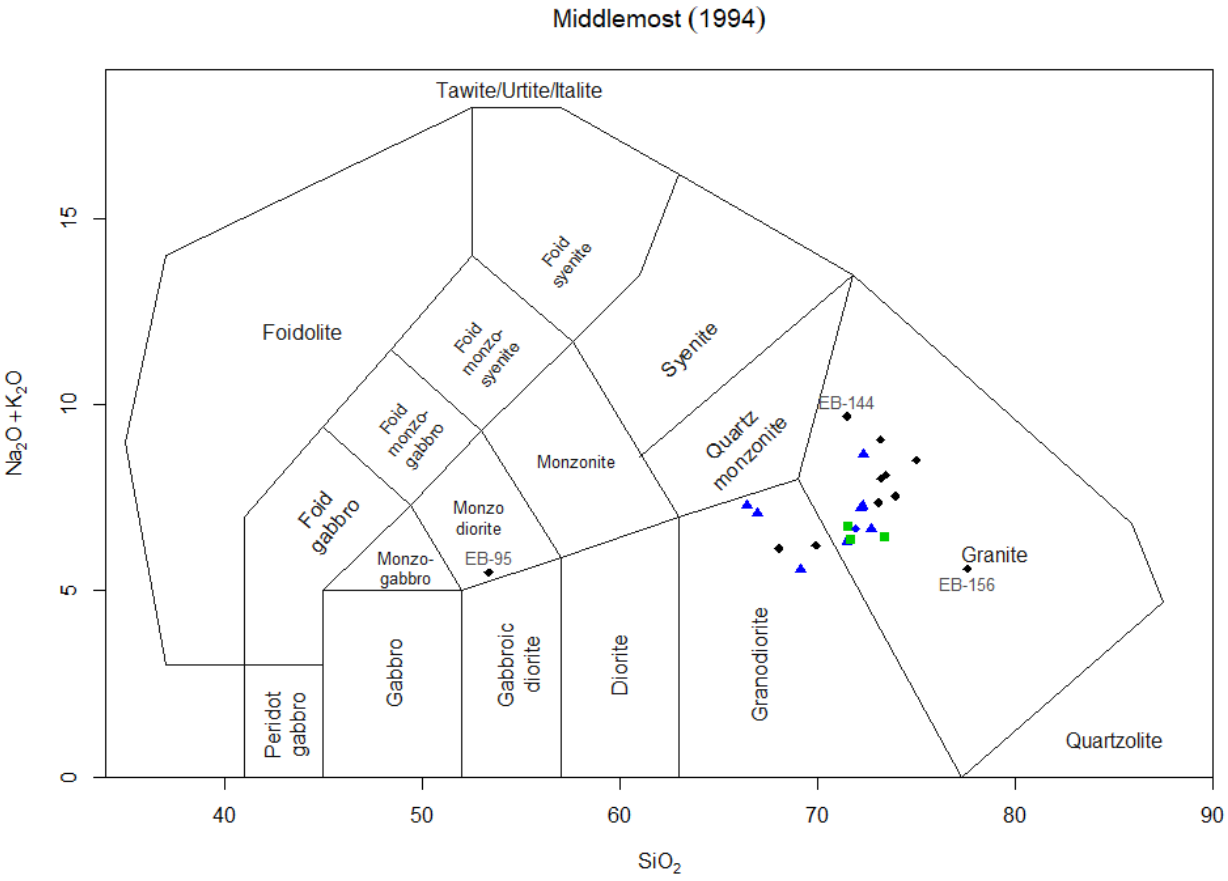

Figure 13: Classification plot TAS for plutonic rocks exported from with GCD-Kit. The samples were coloured and symbolized according to their location on Disko Island. The blue triangles are the samples in the north of Qeqertarsuaq, the black squares are from the east of Qeqertarsuaq and the green squares are from the west.

In Figure 13, EB-95, with the lowest SiO_2 value, plots in the Monzodiorite category, as the only one of the samples. The other samples all plot in the Granite or Granodiorite section. EB-156 with the highest SiO_2 value and EB-144 with the highest $Na_2O + K_2O$ value are highlighted as they do not quite plot with the others in a group. EB-156 is plotted outside of Figure 14, because of the high SiO_2 content but if the lines were extended, it would possibly plot in the Granite section, just as in Figure 13.

In Figure 14, there is also a section for Tonalites, which EB-1 plots in. In Figure 13, EB-1 is the blue triangle, with the lowest SiO_2 value, so the one which almost plots in the Quartz monzonite section.

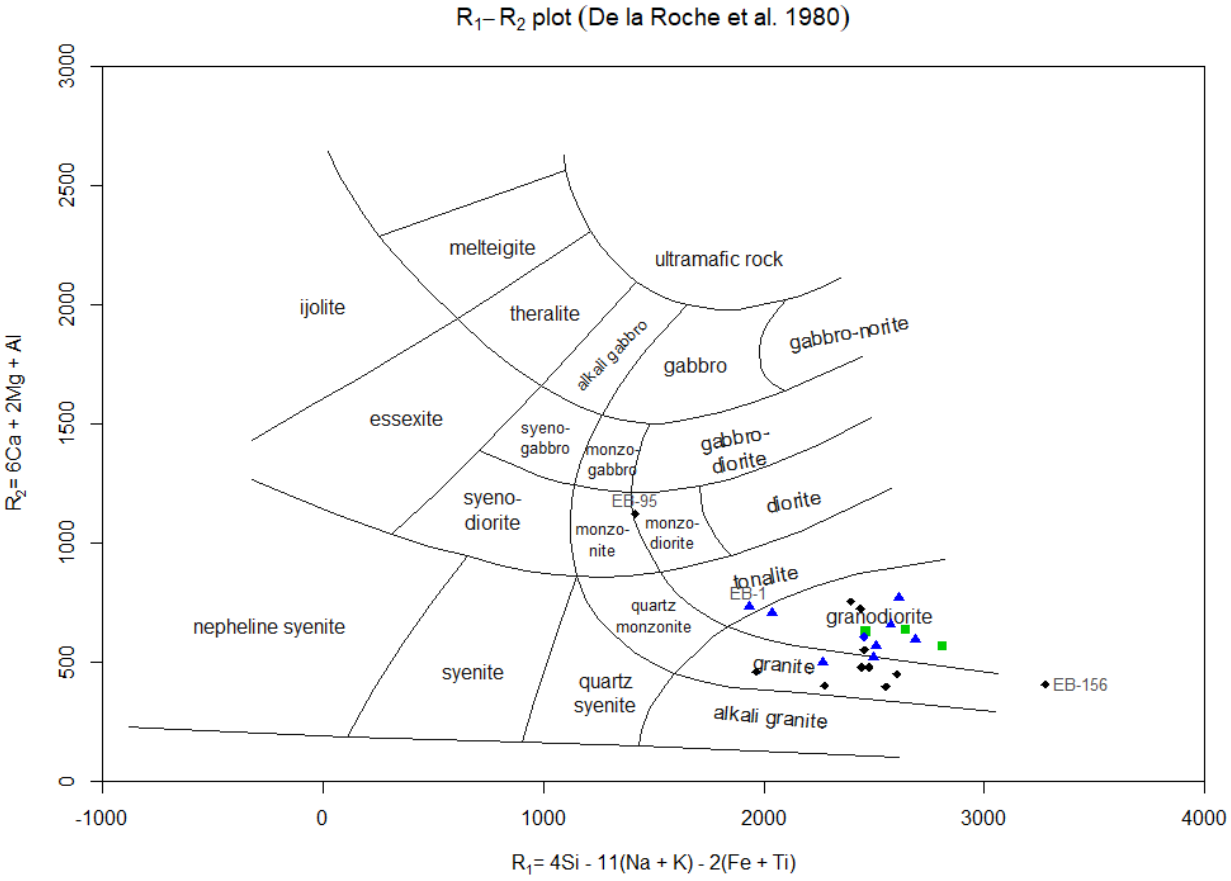

Figure 14: Classification plot exported from GCD-Kit. The samples are coloured according to their location on Disko Island. The blue triangles are the samples in the north of Qeqertarsuaq, the black squares are from the east of Qeqertarsuaq and the green squares are from the west.

4.3. Thin Sections

The thin section figures are exported from ZEN 3.5 with an added ruler in the bottom right corner with a length of 100 µm, for easier detection of size. All the thin sections in the following figures measure 560 x 420 µm. More thin section images which have not been used for description can be found in the appendix.

The sample grains were mostly inequigranular with no orientation of the grains. The grain bonding and grain sizes ranged from inequigranular – interlobate to seriate – interlobate. The samples showed rare glassy grains and are mostly close to being holocrystalline. Many samples showed very big plagioclase grains, as can be seen in Figure 18 or Figure 23.

The samples mainly consisted of quartz, plagioclase, and varying parts of alkali feldspar and mica, mostly biotite. The focus was set on identifying quartz, plagioclase, and alkali feldspars.

The annotations of the minerals are done with the following abbreviations: Quartz (Qtz), Alkali feldspars (Alkf), and Plagioclase (Plg). The abbreviations of the minerals are mostly written in the mineral grain itself, but for some small grains, the annotation was moved to the outside, so the grain is fully visible.

The distinctions of minerals in the thin sections were done with the script for mineral microscopy by Stosch (2009), where the characteristics of the minerals are thoroughly described. In the script, the Michel-Lévy interference colour chart was used for the distinction of minerals via colour (Michel-Lévy & Lacroix, 1888, p. 334).

Quartz was mostly distinguished based on the characteristic undulous extinction, which is observable in Figure 19 in the quartz grain just in the middle.

Another important characteristic is a low relief and no signs of weathering visible in the quartz grains. This can be seen in Figure 21 in the quartz grains in the middle.

On the Michel-Lévy interference colour chart, quartz shows a yellowish-white colour at 30 µm thickness. In Figure 17, Figure 20, or Figure 23, this colour can be seen on the annotated quartz grains. Some quartz grains show slightly different colours, indicating the thickness of the grain to be below 30 µm, at around 27 or 28 µm. The greyish white for these thicknesses of quartz can be seen in Figure 16.

Feldspars are colourless in non-polarised light but can show dulling in contrast to quartz. Figure 24 is a good example of this, where the quartz appears fresh and the feldspars, in this case, plagioclase, show dulling. Alkali feldspars and plagioclase were differentiated either by their characteristic twinning or by the extinction angles according to the characteristics described by Stosch (2009).

Characteristic twinning of microcline, an alkali feldspar, is the cross-hatched twinning, observable in Figure 16 and Figure 22.

Plagioclase often showed complete extinction at angles of 90°, which is hard to show in a picture, but the black plagioclase grain visible in Figure 23 on the left side, is fully extinct. Plagioclase can also show very thin twinning, as seen in Figure 20 on the left side.

According to the interference colour chart of Michel-Lévy & Lacroix (1888), plagioclase shows brighter colours than most alkali feldspars. This can be seen in Figure 18, where the plagioclase in the top right corner shows a greyish-white colour and the alkali feldspar in the middle shows a darker grey colour.

The classification according to the QAP- diagram was done with the template by Stosch (2022) and the diagram can be seen in Figure 15. The samples mostly fall into the Granite or Granodiorite section of the diagram. But some samples, which had almost no alkali feldspars, plot in the Tonalite section. The samples are grouped according to their location on Disko Island, west (W), north (N), and east (E) of Qeqertarsuaq.

The raw estimation data can be found in the appendix.

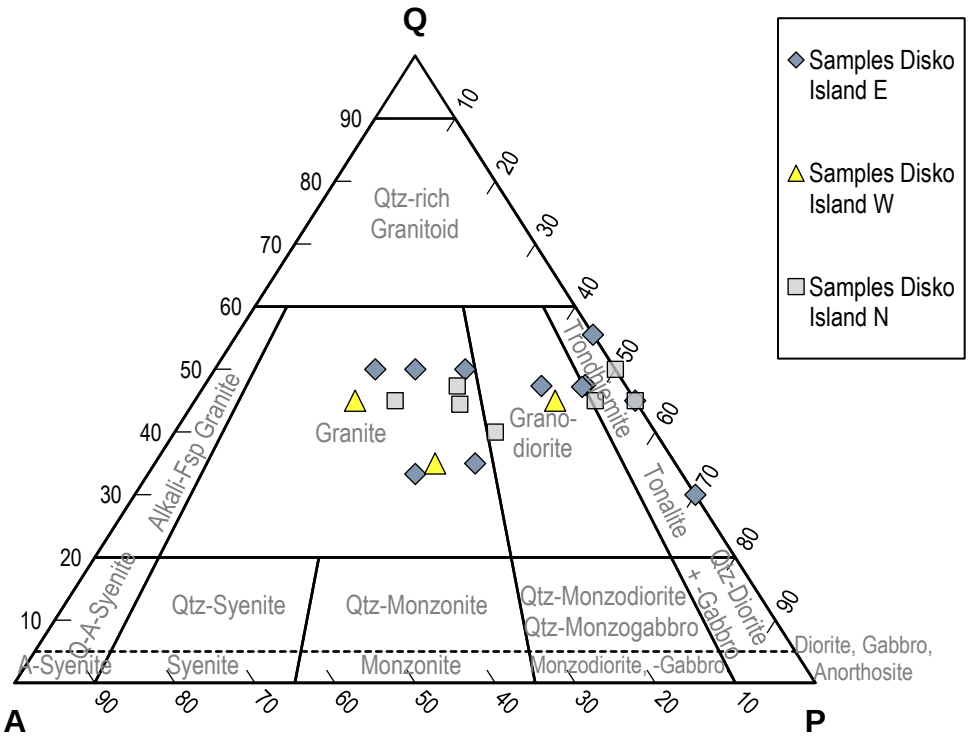

Figure 15: QAP Diagram with the mineral estimation of samples through optical microscopy, created with the excel template by (Stosch, 2022).

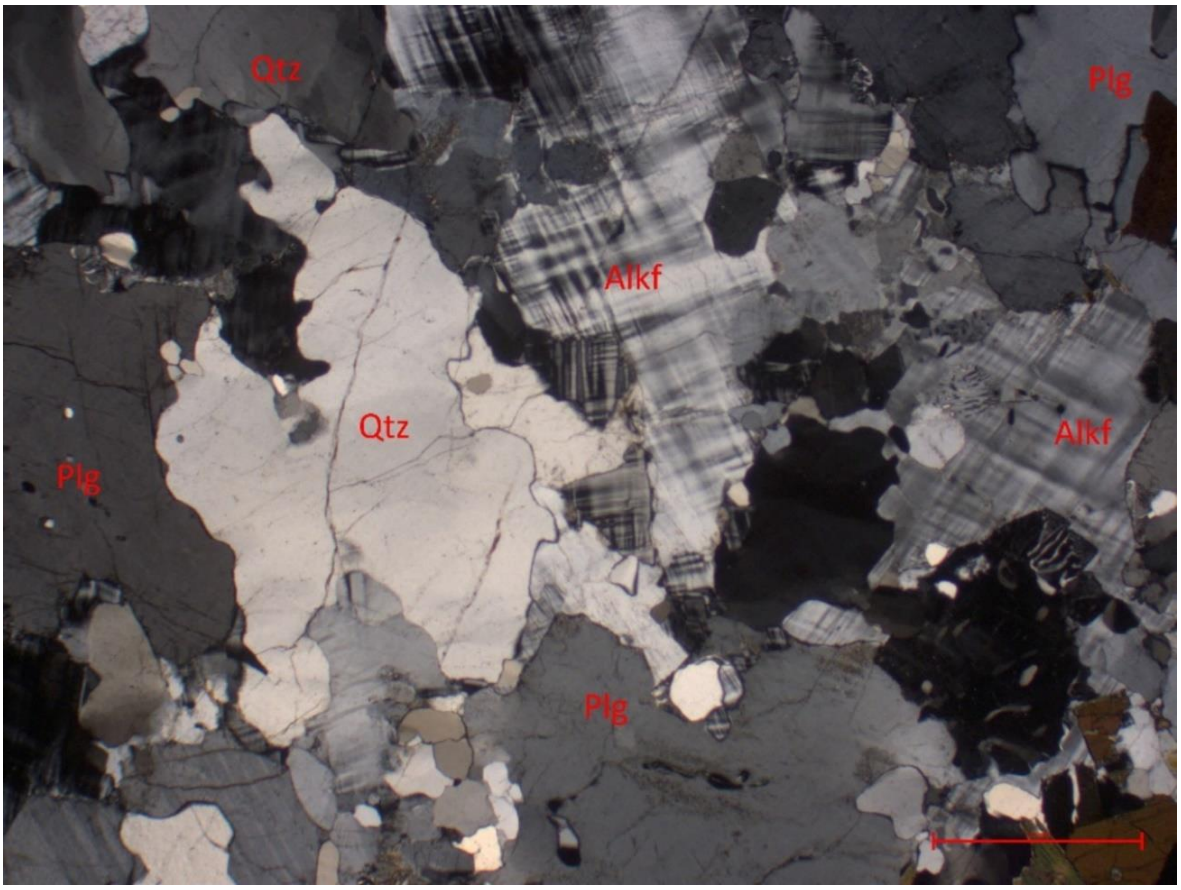

Figure 16: Thin section excerpt of EK-1 Drum under cross-polarised light, exported from ZEN 3.5.

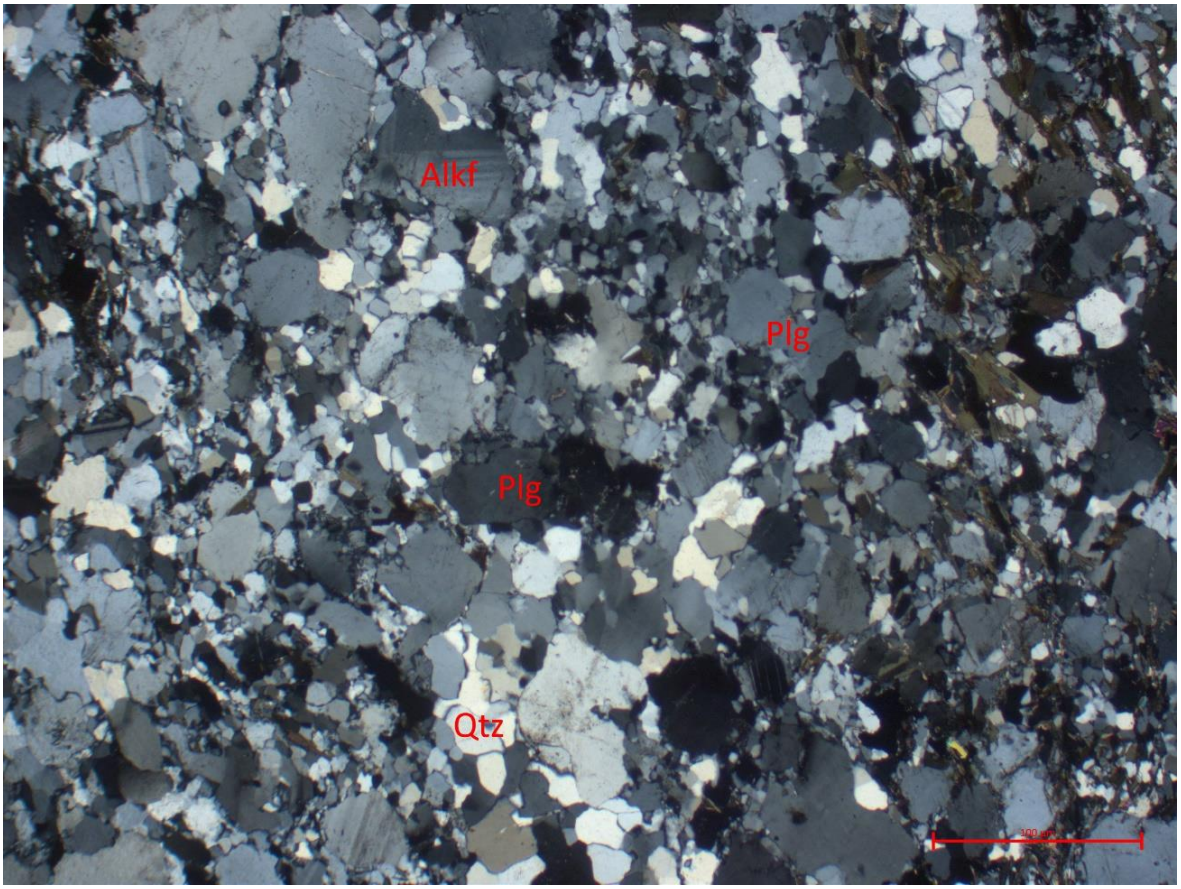

Figure 17: Thin section cutout of BO-4 under cross-polarised light, exported from ZEN 3.5.

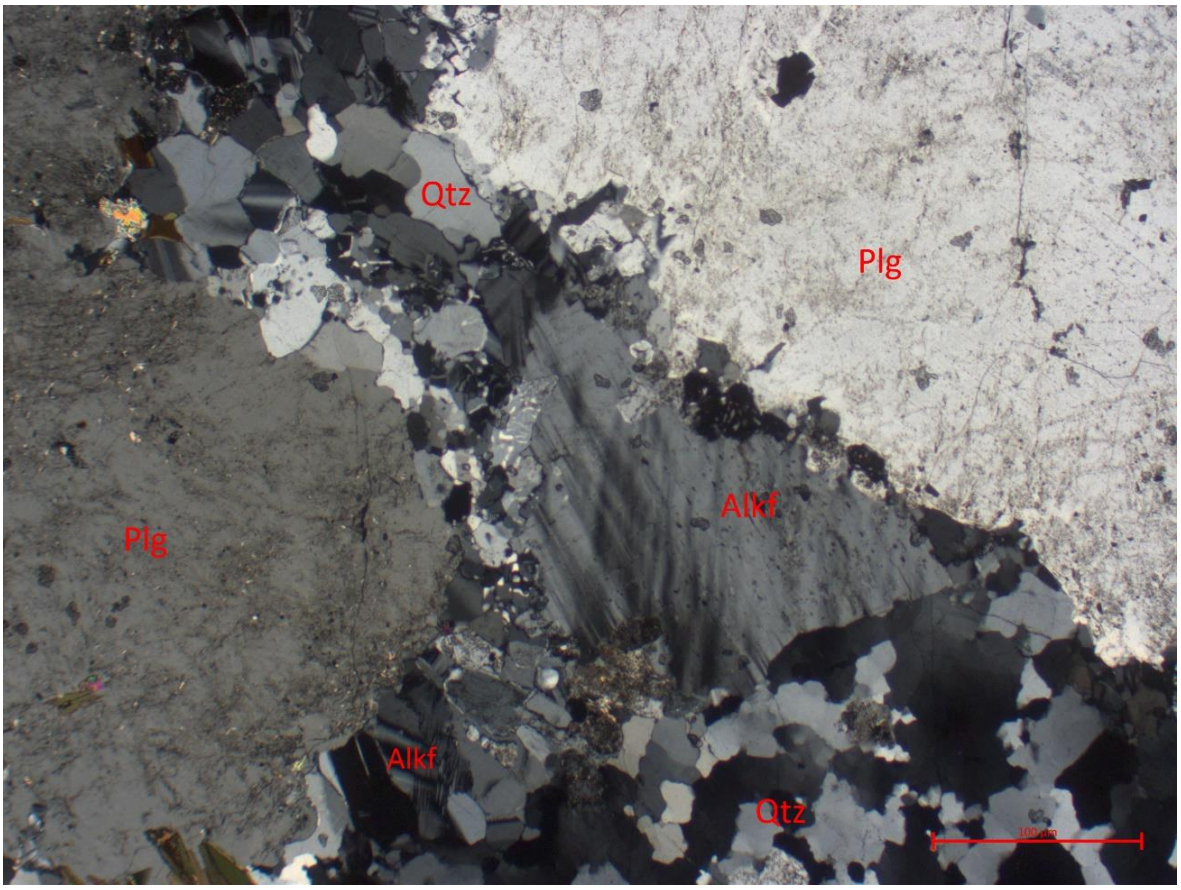

Figure 18: Thin section cutout of EB-25 under cross-polarised light, exported from ZEN 3.5.

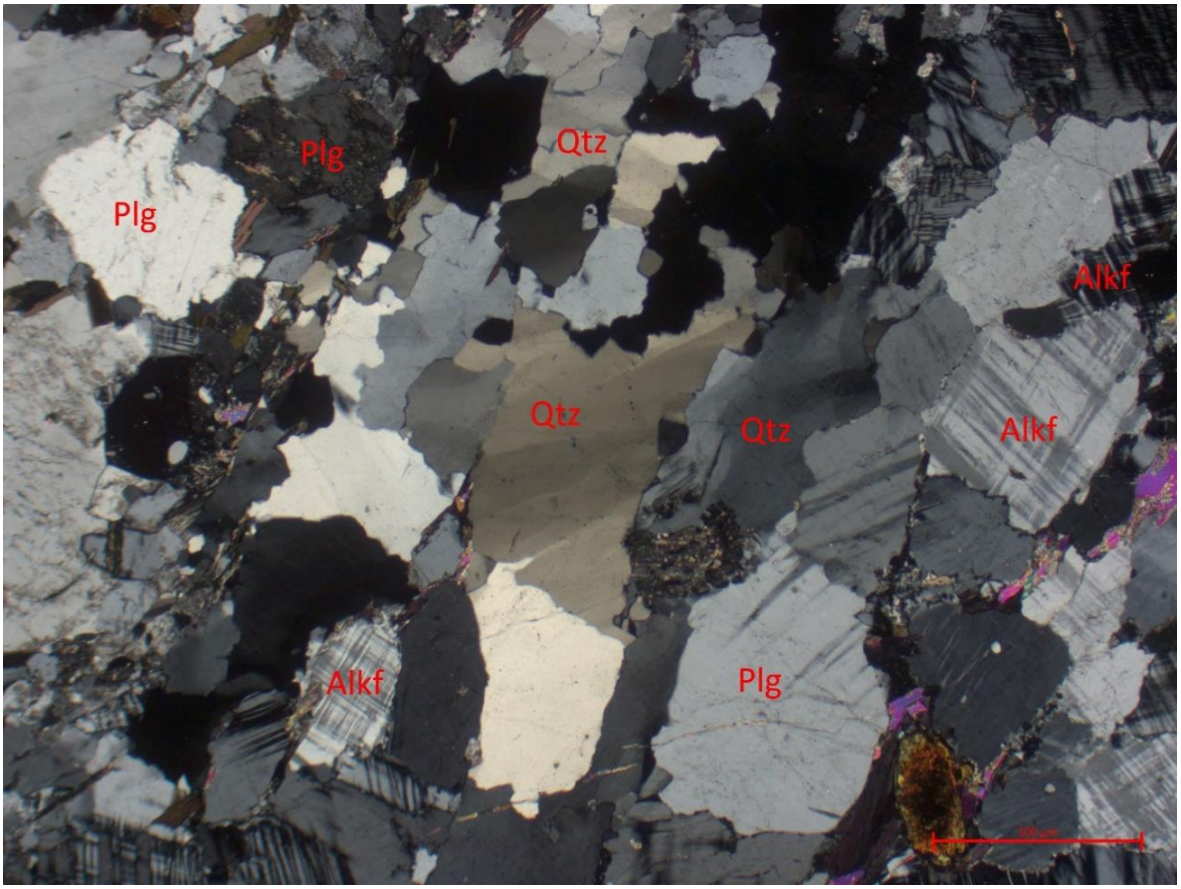

Figure 19: Thin section cutout of EB-45 under cross-polarised light, exported from ZEN 3.5.

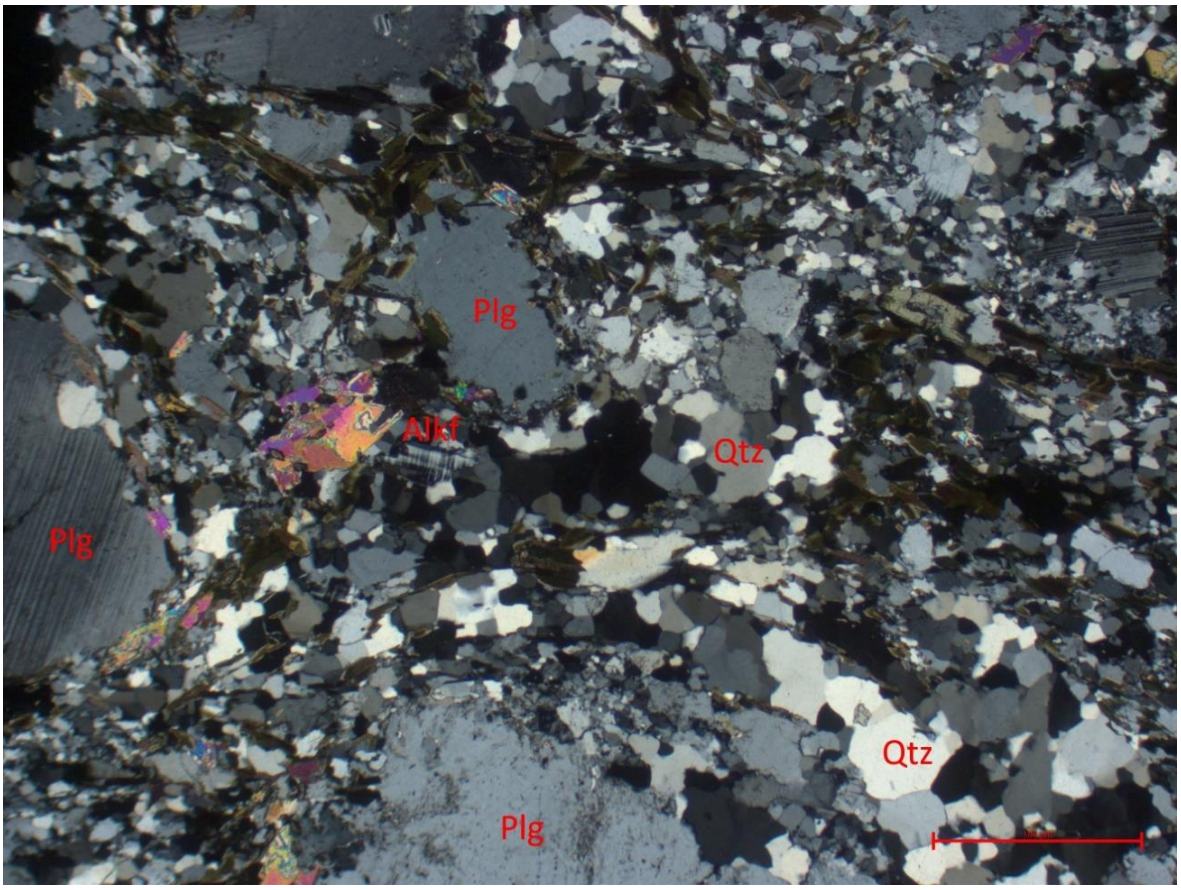

Figure 20: Thin section cutout of EB-1 under cross-polarised light, exported from ZEN 3.5.

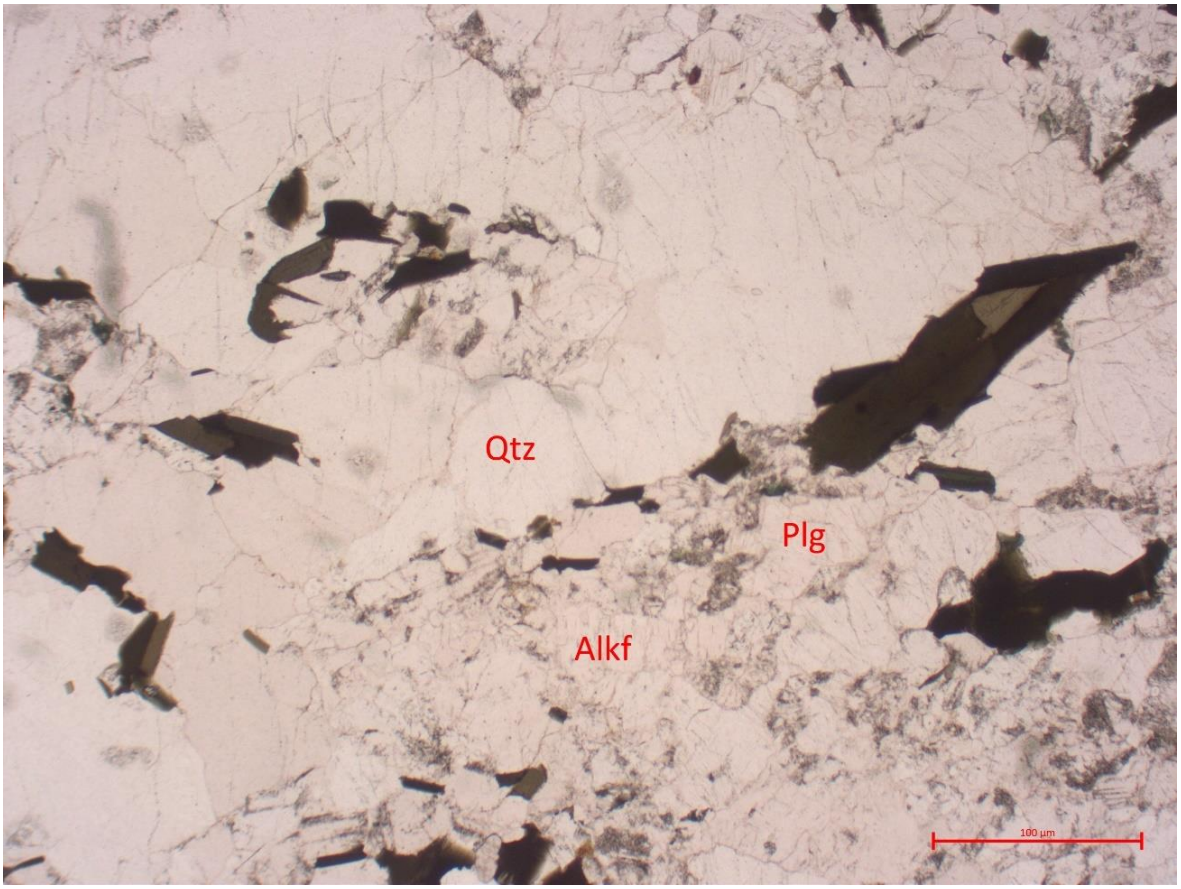

Figure 21: Thin section cutout of EB-19 under non-polarised light, exported from ZEN 3.5.

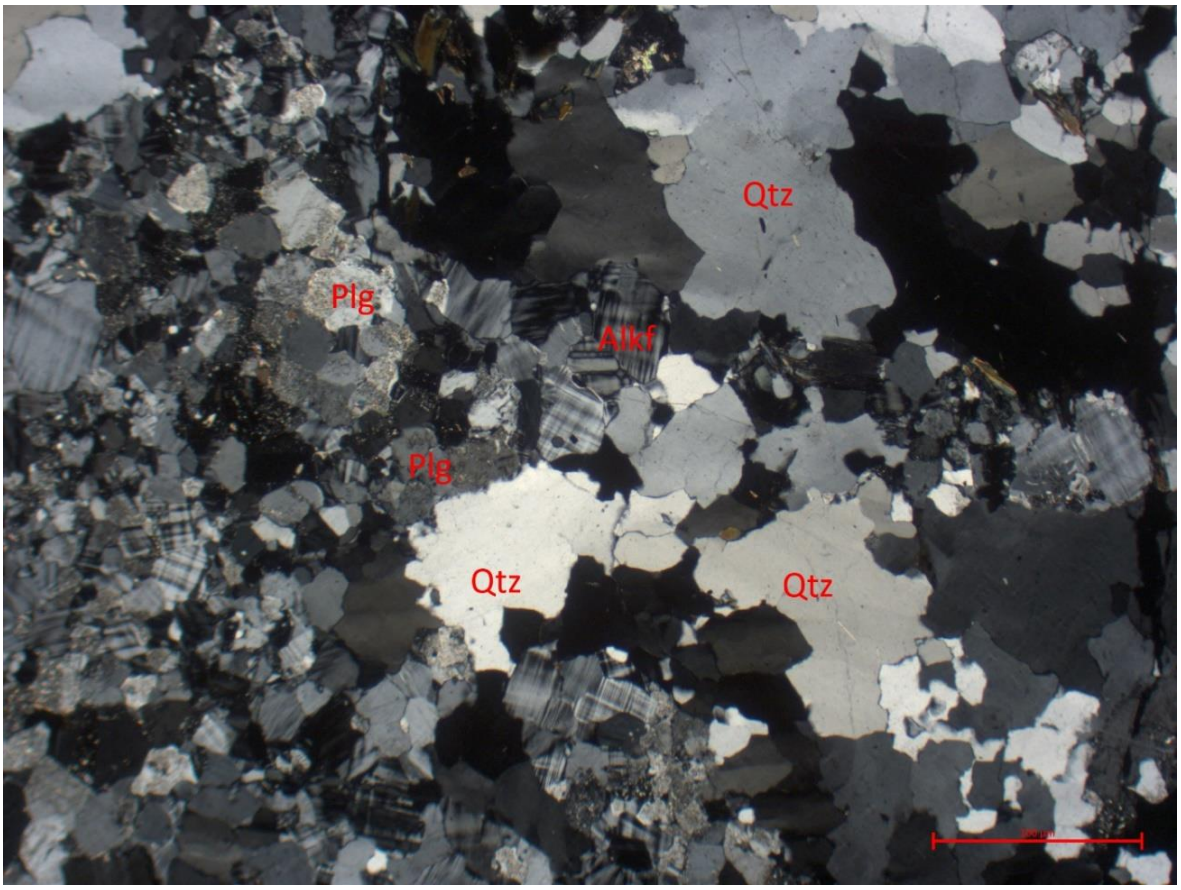

Figure 22: Thin section cutout of EB-97 under cross-polarised light, exported from ZEN 3.5.

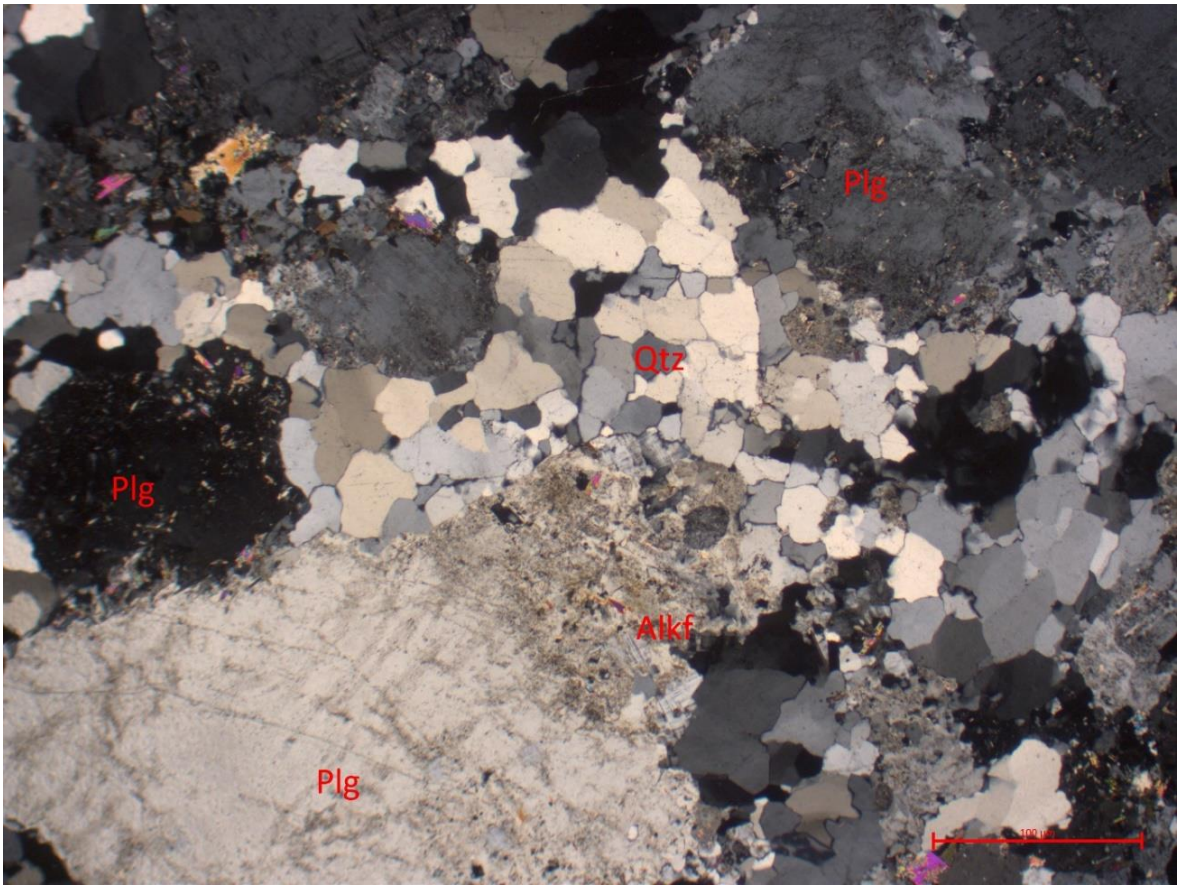

Figure 23: Thin section cutout of EB-151 under cross-polarised light, exported from ZEN 3.5.

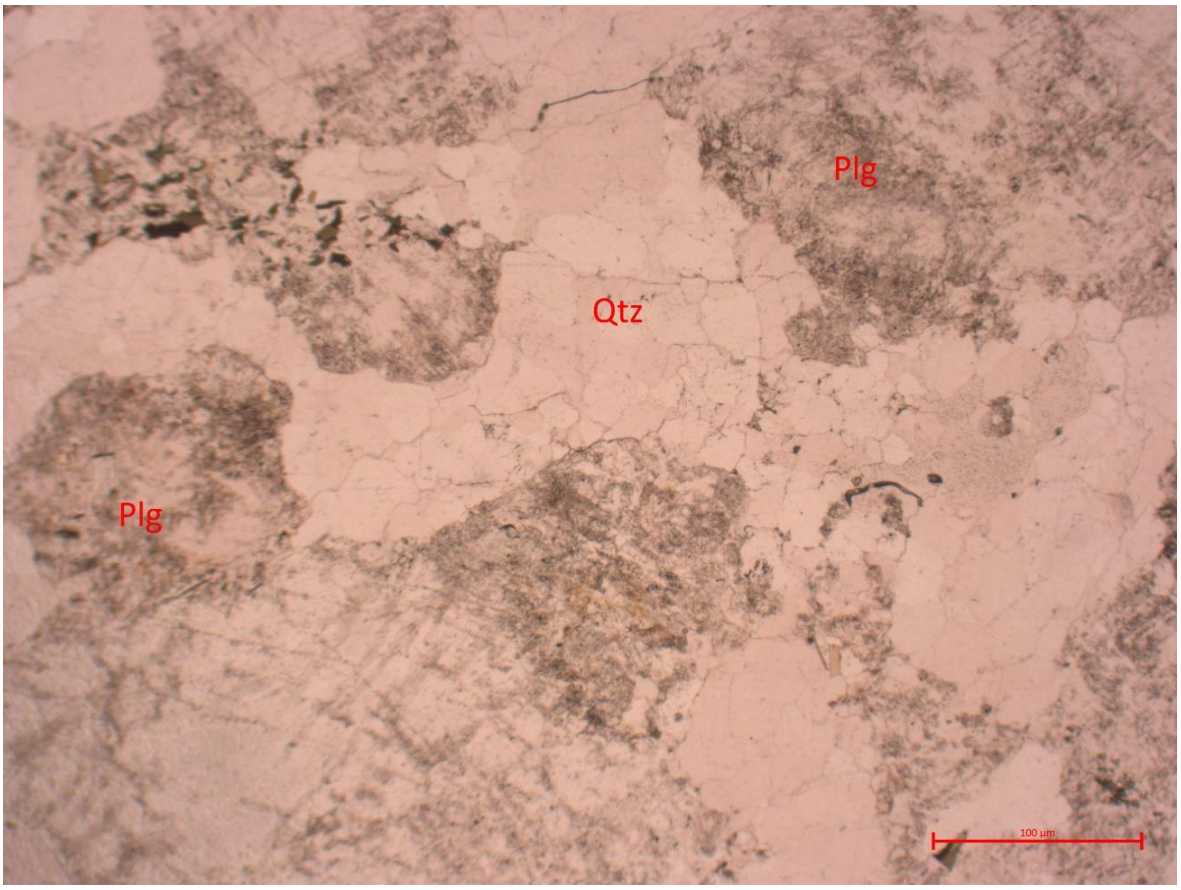

Figure 24: Thin section cutout of EB-151 under non-polarised light, exported from ZEN 3.5.

5. Discussion

5.1. Exposure Ages

Exposure ages can hold a lot of uncertainty, coming from various factors.

Reporting exposure ages with the internal measurement error narrows the age range of deglaciation down to a few hundred years. Unfortunately, the narrowest method holds the most uncertainty, as there are more factors influencing the age of the samples, besides the measurement in the AMS.

In Figure 25 and Figure 26 the effects of erosion (1 to 3 mm per kyr), a constant snow cover, and external errors, such as variation in the scaling model, are plotted next to the internal measurement errors. Here it is important to mention that the internal and external error can change the age of a sample in both directions, so these errors can influence the ages to be younger or older, while erosion and snow cover only lead to older actual ages. Additionally, for snow cover and erosion rate, there is no empirical data available for this region. This is why for these factors assumptions had to be made.

Two plots were created, as the effect of erosion on the three oldest samples would have made the effects on the younger samples look too small. It can be observed that erosion does not play such a big role in most of the samples, but its role increases drastically when looking at much older samples.

In the samples that date below 12 kyrs, the external error causes the single most uncertainty with seven to eight percent change. Erosion only plays a small role in these samples, with a maximum change of 3 %.

Other studies on exposure ages in Greenland have mostly reported no erosion correction (Kelley et al., 2013; Larsen et al., 2016; Lesnek & Briner, 2018; Søndergaard et al., 2020). Håkansson et al. (2007) have reported erosion up to 10 mm per kyr for their samples in central east Greenland, which were mainly sandstones and therefore were more subjected to erosion as granitoids in this case. Because of the goals of this research and the limited effect of erosion on most of the samples, a maximum erosion rate of 3 mm per kyr was decided to be looked at.

Snow cover can also be a factor influencing the production rate and therefore the ages of the samples. As previously described, due to the low precipitation on Disko Island, snow cover is negligible for these samples, and are therefore not included in the uncertainty analysis because of the limited effect on the ages. Other studies on Disko Bugt also did not account for snow cover on the samples (Kelley et al., 2013).

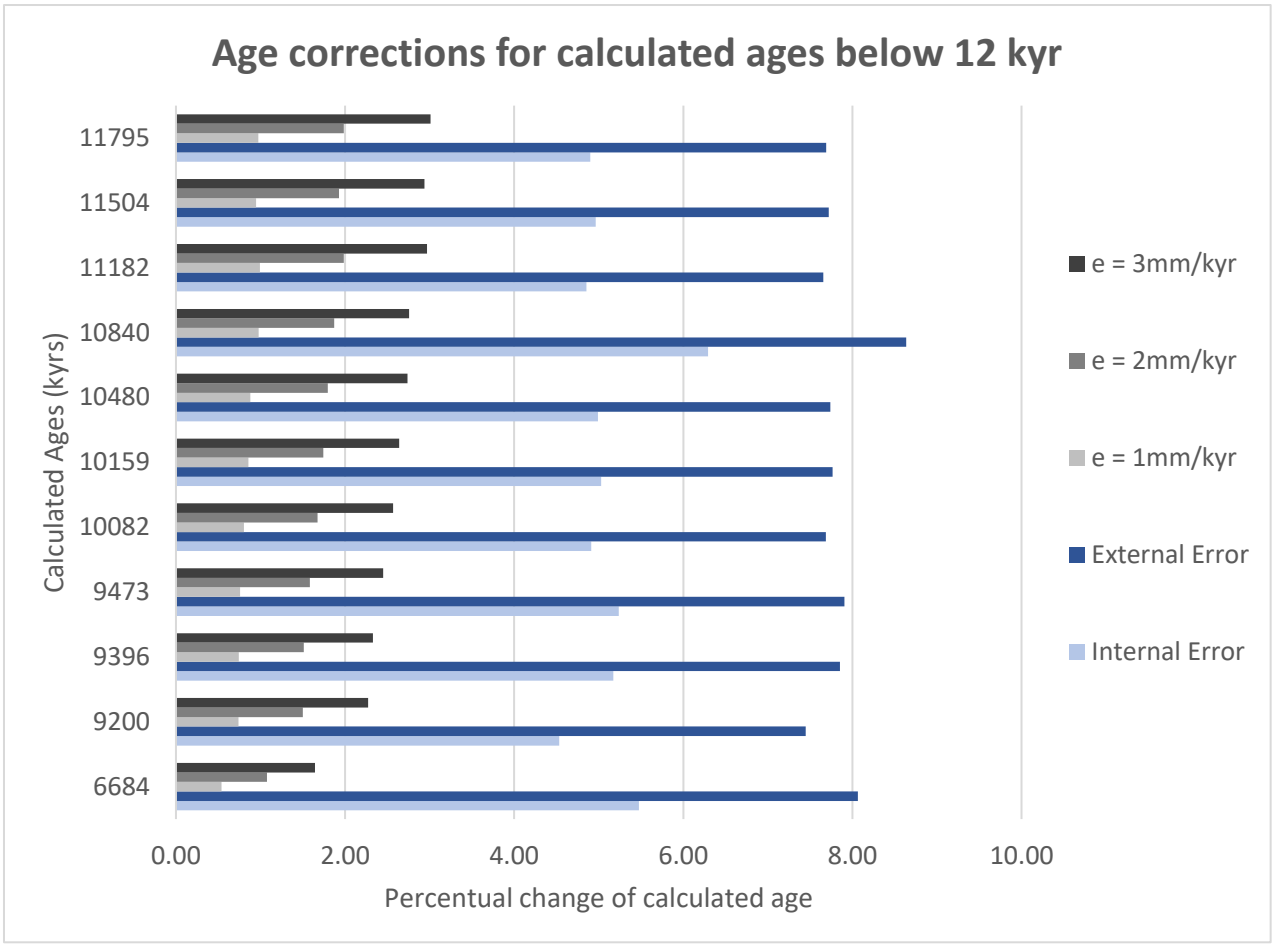

Figure 25: Different age corrections in % for ages below 12 kyrs of the calculated ages.

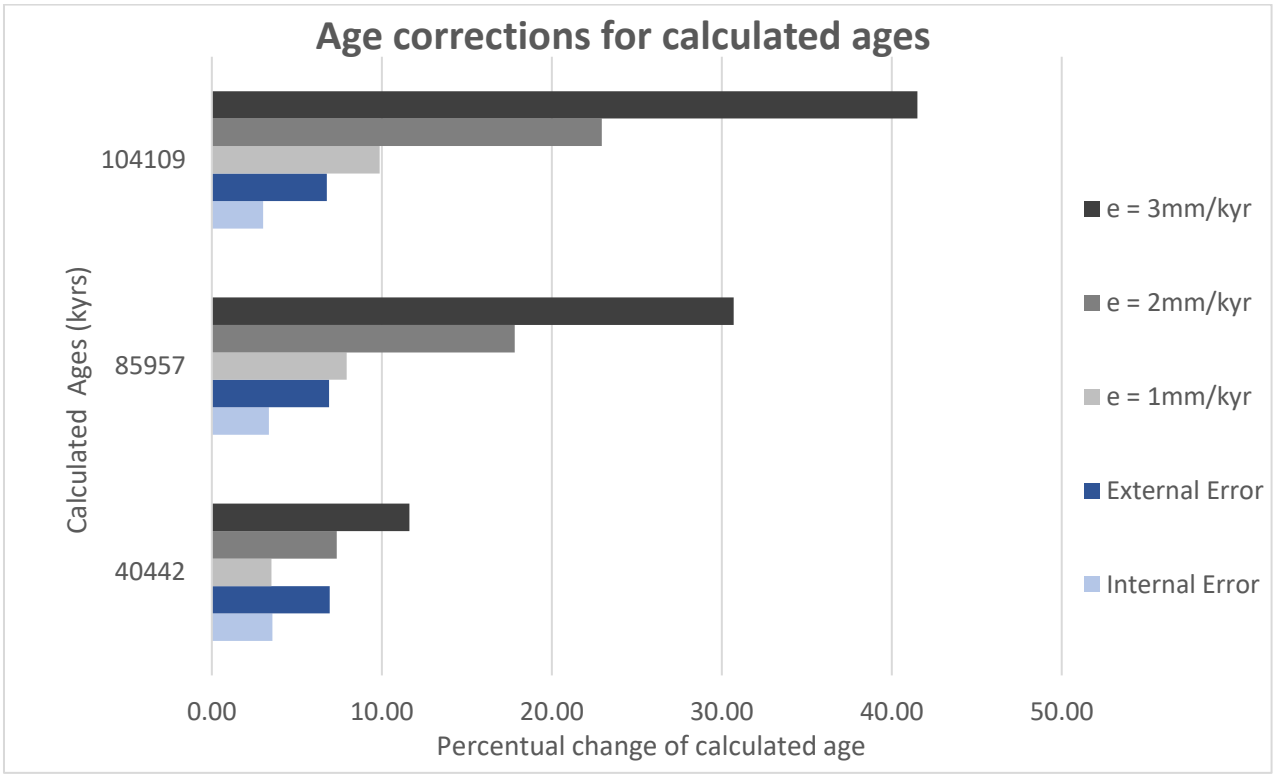

Figure 26: Different age corrections in % for the three oldest calculated ages.

For the samples with much higher ages on the basaltic plateau, erosion can have the biggest effect on the age of the sample. For the youngest of the three samples, EB-195 with an age of 40'442 yrs, 1 mm per kyr erosion issues a 3.5 % change, while 2 mm per kyr already surpasses the external error factor, with an age increase of 7.35 %. The impact of erosion only increases with older ages, as 2 mm per kyr erosion already raises the age of EB-167 by 17.8 %.

Another factor of uncertainty is the scaling model, which is used for the calculation of the ages. For comparison of the scaling models, the different results for the 14 samples in this study, are listed in Table 6.

Table 6: Exposure Ages (yrs) with different scaling models.

Sample Name	Scaling Model		
	Lal/St	Lm	LSDn
EB-190	110'034	106'789	104'109
EB-195	42'734	41'495	40'442
EB-167	90'670	88'011	85'957
EB-156	9'766	9'486	9'200
EB-151	10'796	10'486	10'159
EB-144	7'085	6'882	6'684
EB-55	12'630	12'270	11'795
EB-98	11'285	10'962	10'480
EB-19	10'186	9'894	9'396
EB-1(3)	10'108	9'818	9'473
EB-250	10'836	10'526	10'082
EB-253	11'714	11'379	10'840
EK-1 Drum	11'958	11'616	11'182
BO-2	12'297	11'946	11'504

Overall, the Lal/St scaling model yields on average 6.8 % older ages than the output from the LSDn model. The Lm model lies between the Lal/St and LSDn model and outputs 3.7 % higher ages on average than the LSDn model.

Other ^{10}Be ages on Disko Island, which are located between the western and the northern samples of this study, have been dated to an average of 10.0 ± 0.1 kyrs (Kelley et al., 2013). The samples by Kelley et al. (2013) based on the Lal/Stone scaling model, have not been corrected for snow cover or erosion, and are reported as mean ± internal errors.

As Kelley et al. (2013) have reported their ages with the Lal/St scaling model, the samples are approximately 700 years younger, in LSDn terms.

The average ages for the three sample sites on southern Disko Island come together to suggest a retreat of the GrIS from west to east from 11.3 ± 0.9 to 9.6 ± 0.7 kyrs.

This data agrees with the proposed general retreat history of Disko Bugt (Kelley et al., 2013; Weidick & Bennike, 2007).

When taking into consideration the possible age range, when including all the factors listed here, the age results of this study and the ages of Kelley et al. (2013) go together in their approximate age ranges to the conclusion, that the landscape north of Qeqertarsuaq was deglaciated at around 10.0 kyrs.

A sample that falls out of the timeline of ice retreat on Disko island and the Disko Bugt, is EB-144. With an age of 6.7 ± 0.5 kyrs, it has been exposed for a much shorter time than the rest of the samples. If the boulder was deposited by the GrIS with all the other samples, one possibility for this anomalously young age could be that the boulder was moved after deposition. So the boulder could have rolled over. The movement of such a boulder would bring previously shielded surfaces to the exposure of CNs and a completely new time clock would start to build up. Another possibility for this age could be the burial of the EB under soil for a long period of time. For further assessment of this outlier, a second CN analysis could help.

The samples EB-167, EB-190, and EB-195 yield much older ages than all the other samples. These ages will be discussed later.

5.2. Origin of Erratic Boulders

The output of the classification plots of Figure 13 and Figure 14 can be found in Table 7. Along with the TAS and the R_1-R_2 plot labels, the classification according to the optical microscopy is also listed in Table 7. The optical classifications are taken from Figure 15.

Table 7: Classification of samples according to plutonic classifications and optical microscopy.

	TAS (Middlemost, 1994)	R_1-R_2 (de la Roche et al., 1980)	Optical Microscopy
BO-2	Granite	Granodiorite	Granite
BO-4	Granite	Granodiorite	Granodiorite
EB-1	Granodiorite	Tonalite	Tonalite
EB-113	Granite	Granite	Granodiorite
EB-144	Granite	Granite	Granite
EB-151	Granite	Granodiorite	Tonalite
EB-156	Granite	*Outside of plot, see Figure 14*.	*broken*
EB-167	Granite	Granite	Granite
EB-19	Granite	Granite	Granite
EB-190	Granite	Granite	Tonalite
EB-195	Granodiorite	Granodiorite	Tonalite
EB-25	Granodiorite	Granodiorite	Granodiorite
EB-250	Granite	Granodiorite	Granite
EB-253	Granite	Granite	Granite
EB-45	Granite	Granodiorite	Granite
EB-55	Granodiorite	Granodiorite	Tonalite
EB-59	Granodiorite	Granodiorite	-
EB-60	Granite	Granodiorite	Tonalite

EB-65	Granite	Granite	Tonalite
EB-83	Granite	Granodiorite	Tonalite
EB-95	Monzodiorite	Monzodiorite	-
EB-97	Granite	Granite	Granite
EK-1	Granite	Granodiorite	Granite

The samples were mostly classified as Granites or Granodiorites based on the chemical analysis and Granites or Tonalites based on the optical classification. A possible explanation for this shift towards Tonalites in the optical classification could be due to underestimations of small grains in the thin sections. The estimation of mineral contents was done visually and rather at a rough estimate, as the time cost for more in-depth estimation was too high. Since many samples showed rather large (phanerocrystalline) plagioclase grains, the amounts assigned to plagioclase were possibly often larger than the actual amount.

To search for the origin of such erratic granitoid samples on Disko Island, a look at the mainland coast of Greenland is needed. In Figure 27, the geological setting of the whole Disko Bugt region is shown. The eastern coast of Disko Bugt is mainly composed of reworked Archean orthogneisses and granitic gneisses. Directly east of Disko Island so called Atâ Granites and associated grey dykes (Kalsbeek et al., 1988) and Atâ Tonalites (Kalsbeek & Skjernaa, 1999) can be found. More to the south of Disko Bugt, Kalsbeek (2001) has reported geochemical data for orthogneisses. For further investigation and comparison, the data for the two Atâ groups together, hereinafter referred to as Atâ Granites, just east of Disko Island, and data for orthogneisses were analysed.

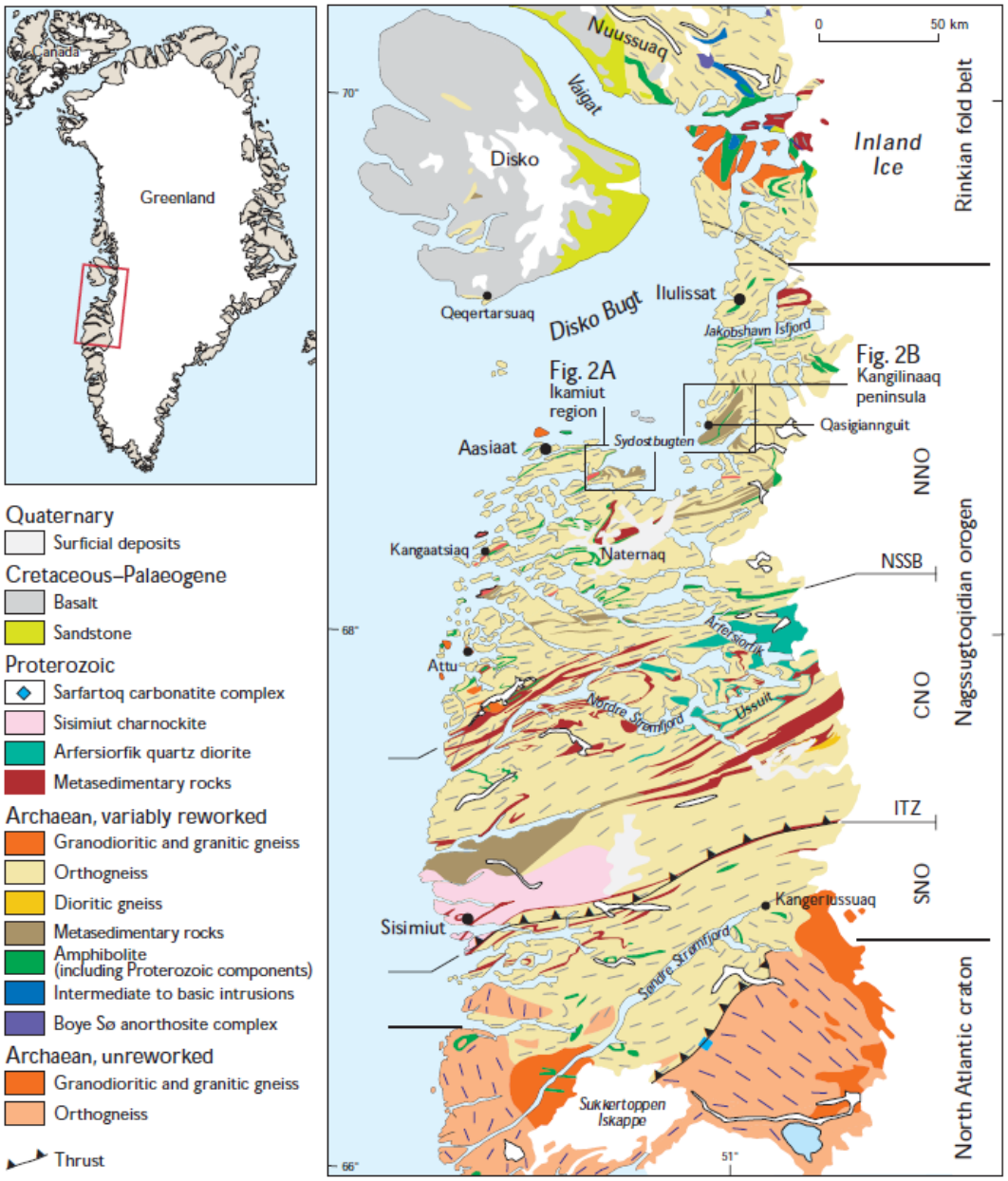

Figure 27: Geology of the mainland coast of central western Greenland (Gool et al., 2002). This geological map was directly taken from Hollis et al. (2006). The outlined areas for Figures do not matter for this Thesis.

The major elements for the samples of this master's thesis are plotted against SiO_2 in so called Harker diagrams in Figure 28.

In Figure 29, Harker diagrams for the orthogneisses from southern Disko Bugt (Kalsbeek, 2001) are plotted. Accordingly, in Figure 30, the Harker diagrams of the Atâ Granites from the eastern shore of Disko Bugt are displayed.

For the petrological comparison, the samples in this thesis generally showed more alkali feldspars, than the orthogneisses described by Kalsbeek (2001) or the Atâ Granites (Kalsbeek et al., 1988), where alkali feldspars were sparse or absent in the samples.

On the proposed classification diagrams by de la Roche et al. (1980) and Middlemost (1994), the orthogneisses and Atâ Granites also plot in the Granodiorite and Granite sections.

For all major elements but K_2O, a decline in wt% with increasing SiO_2 is visible in the samples in Figure 28. The K_2O values first decrease until SiO_2 reaches approximately 68 wt%, and then there is a rapid increase in K_2O values with increasing SiO_2 values observable.

For the other samples, the trend of decreasing K_2O wt% with increasing SiO_2 is also observable in the other samples in Figure 29 and Figure 30.

The compositions of the Atâ Granites are generally closer to the values of the samples from this study than the orthogneisses' compositions, especially since the K_2O and Na_2O values show quite similar distributions (Figure 30).

When looking at only the Archean orthogneisses, the similarity to the samples from this study is higher than when looking at the Proterozoic orthogneisses, as the Archean orthogneisses show similar trends and similar wt% values, just as the Atâ Granites.

The Archean orthogneisses also show an increase in K_2O values with increasing SiO_2 in Figure 29 in contrast to the Proterozoic counterparts.

The one black square with the lowest SiO_2 wt% is EB-95. This sample is clearly an outlier, as it plots outside of all the other samples. Whilst being an outlier, EB-95 does however represent the main trends in some Harker diagrams, so the decreasing wt% of Al_2O_3, MgO, CaO, P_2O_5, and FeO_t.

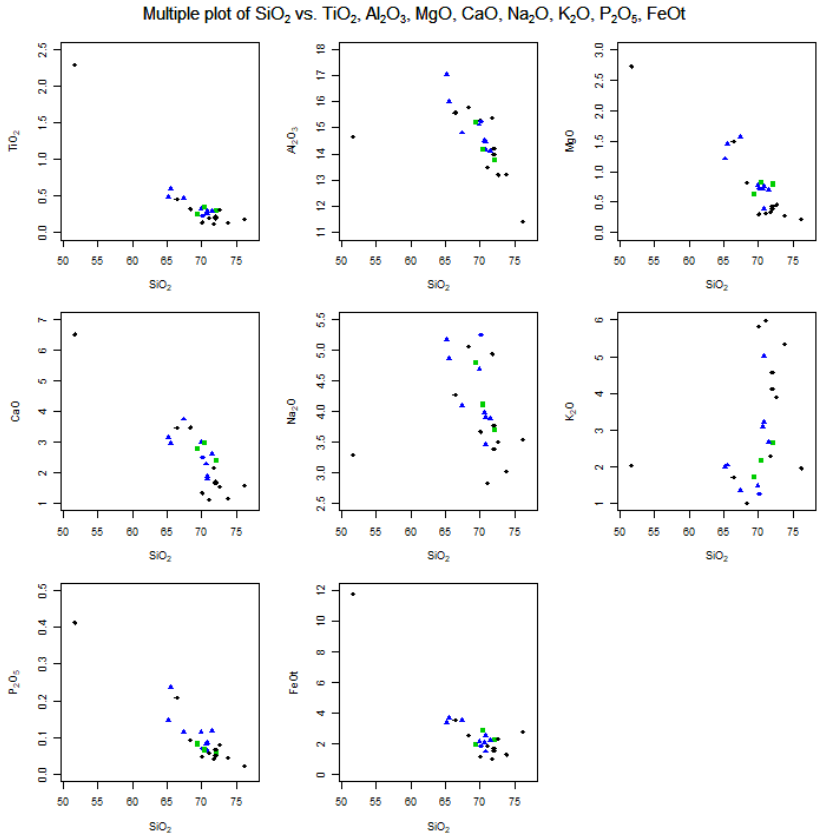

Figure 28: Harker diagrams for studied plutonite samples of this thesis. The samples are coloured and symbolised according to their location on Disko Island. The blue triangles are the samples in the north of Qeqertarsuaq, the black squares are from the east of Qeqertarsuaq and the green squares are from the western site.

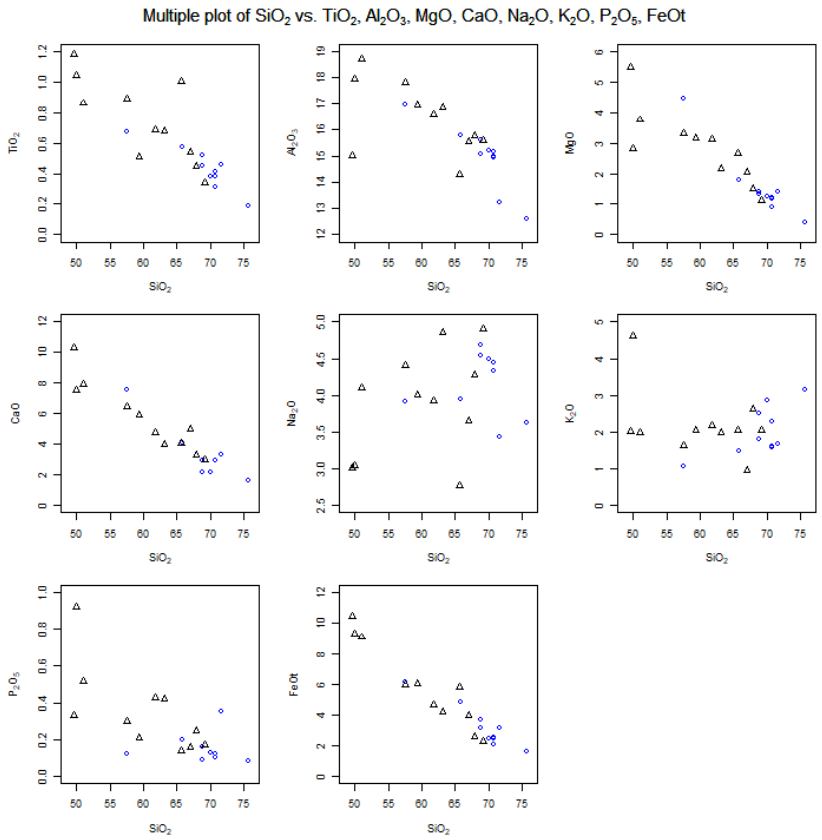

Figure 29: Harker diagrams for Archean and Proterozoic Orthogneisses. The Proterozoic orthogneisses are plotted with black triangles, while the Archean orthogneisses are plotted as blue dots.

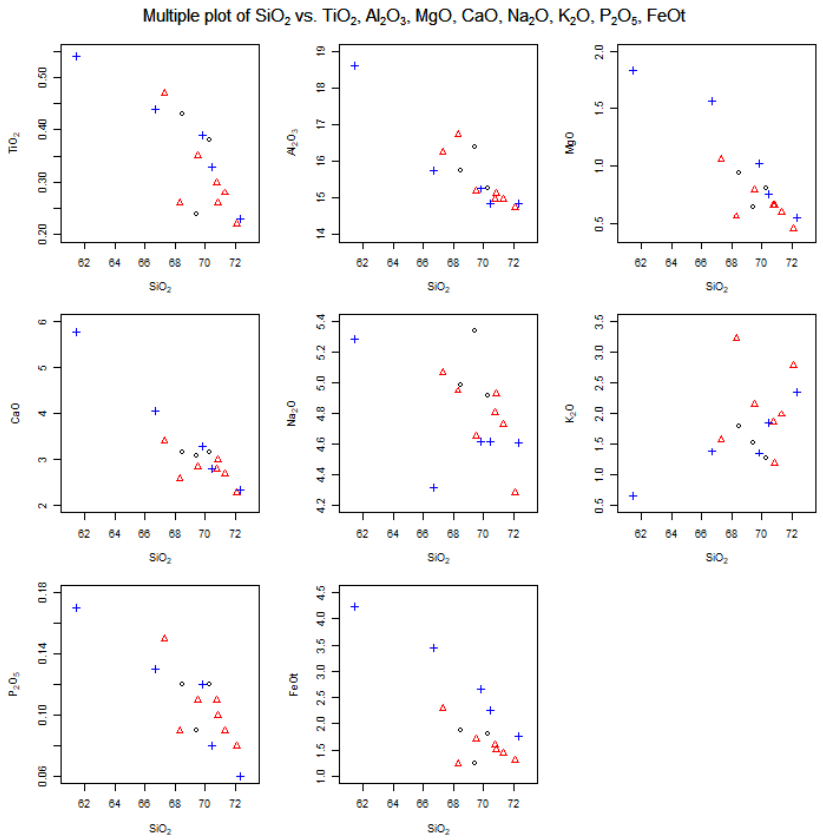

Figure 30: Harker diagrams for Atâ Granites. The Atâ Granites and associated grey dykes are symbolised with red triangles and black circles respectively, while the Atâ Tonalites are symbolised with blue crosses.

The origin of the samples can further be analysed with geotectonic classifications. The geotectonic settings of the formation of the granites can be looked at with major elements and trace elements. There are various possible plots available, but for major elements, tectonic discrimination according to Maniar & Piccoli (1989) was used. For trace elements, a diagram by Pearce et al. (1984) was used.

The geotectonic classifications can be viewed in Figure 31, Figure 32, and Figure 33 for the samples of this thesis, the orthogneisses and the Atâ Granites respectively.

Figure 31 shows that most samples from this thesis plot in the sections of IAG (island arc granitoids) + CAG (continental arc granitoids) + CCG (continental collision granitoids), or in the POG (post-orogenic granitoids) section. The one outlier which occasionally plots differently is EB-156, in the RRG (rift-related granitoids) + CEUG (continental epeirogenic uplift granitoids) section.

The POG group does not have its own field, as it constantly shows characteristics of both other groups (Maniar & Piccoli, 1989).

Further discrimination between IAG, CAG, and CCG can be done within the A/CNK variable. Only samples, which belong to the group of CCG have A/CNK [= $Al_2O_3/(CaO + Na_2O + K_2O)$] values of 1.15 and greater. The maximum value for A/CNK for the samples from Disko Island

is 1.06. This classifies the samples in the IAG or CAG section. Further discrimination in this group of IAG and CAG is not possible (Maniar & Piccoli, 1989).

So the plots in Figure 31 indicate the granitic rocks on Disko Island, to be either island or continental arc - granitoids, or granitoids from a post-orogenic setting.

The agreement on formation in IAG+CAG+CCG or POG is seen in all samples portrayed here, and just as in the samples from Disko Island, there are no samples with an A/CNK value of 1.15 or above, which leaves the classification to IAG, CAG, and POG. The Atâ Granites, however, show more similarities, or fewer outliers than the orthogneisses. Especially in the lower row of plots, the orthogneisses vary more.

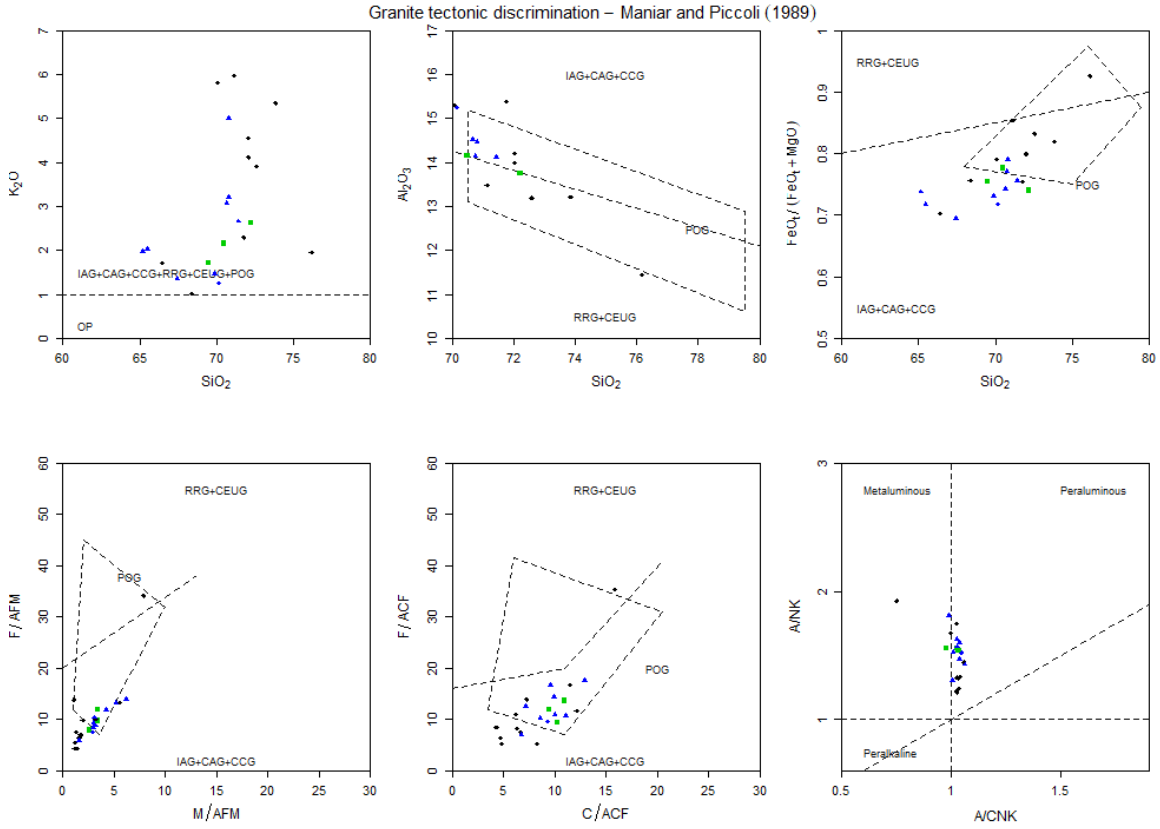

Figure 31: Geotectonic distinction of samples in this thesis. The samples are coloured and symbolised according to their location on Disko Island. The blue triangles are the samples in the north of Qeqertarsuaq, the black squares are from the east of Qeqertarsuaq and the green squares are from the western site.

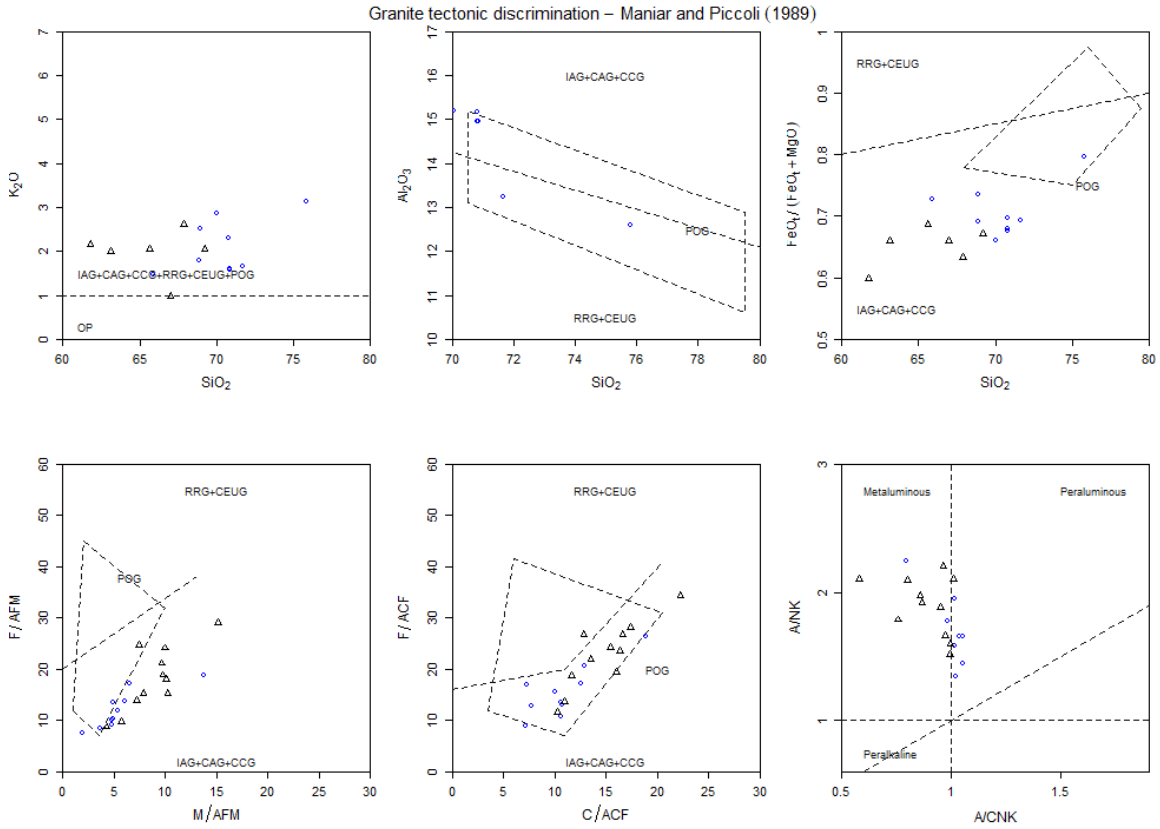

Figure 32: Geotectonic distinction of the orthogneiss samples. The Proterozoic orthogneisses are plotted with black triangles, while the Archean orthogneisses are plotted as blue dots.

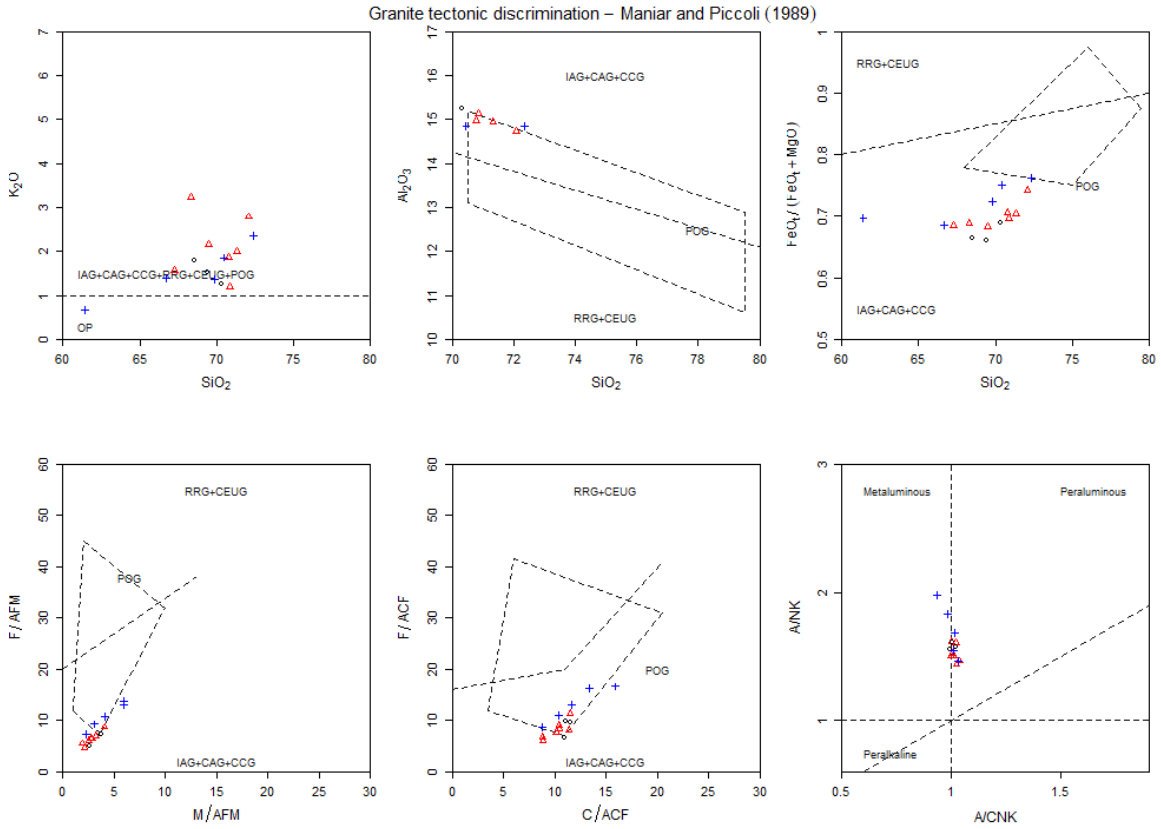

Figure 33: Geotectonic distinction of Atâ granite samples. The Atâ Granites and associated grey dykes are symbolised with red triangles and black circles respectively, while the Atâ Tonalites are symbolised with blue crosses.

For further distinction with trace elements, the most used trace elements are Rb, Y, Nb, Yb, and Ta (Pearce et al., 1984).

As the XRF measurements at ETH did not result in Yb or Ta values, only one diagram from Pearce et al. (1984) could be used, including the Rb, Y and Nb values. For the samples of this thesis the diagram is displayed in Figure 34. Important to note is that only four samples from Disko Island resulted in positive Nb values, so the main driver for values on the x-axis of Figure 34 is the Y values and not the Nb values. For the orthogneisses also no Ta or Yb values were reported, therefore these samples are plotted on the same diagram as well. The geotectonic classification of the orthogneisses is displayed in Figure 35. For the Atâ Granites, only the Atâ Tonalites were reported with all necessary trace elements to compare (Kalsbeek, 2001; Kalsbeek & Skjernaa, 1999). The Atâ Granites were reported with no Nb values.

The lack of trace elements Yb and Ta is a clear limitation of this distinction because there would be other diagrams available determining the geotectonic setting within the proposed plots by Pearce et al. (1984).

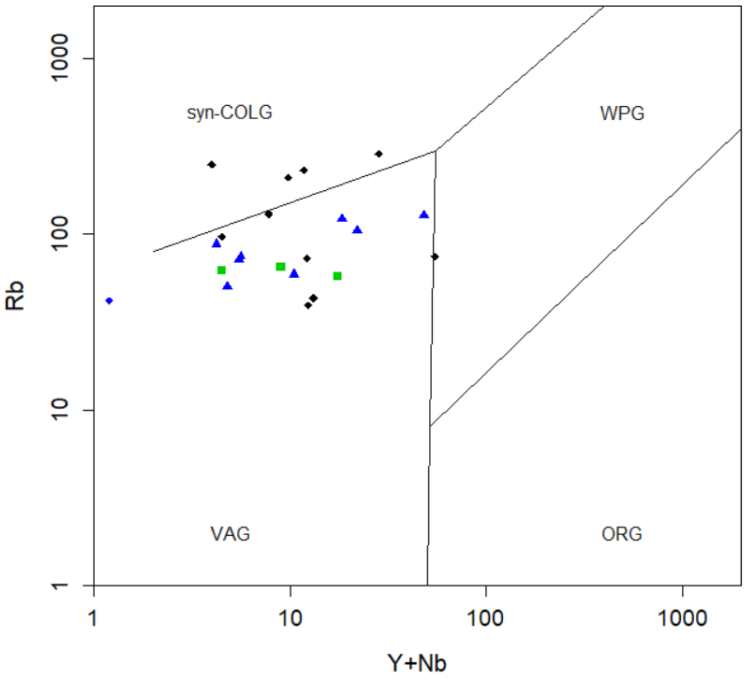

Figure 34: Diagram for geotectonic trace element discrimination for the samples of this thesis. The samples are coloured and symbolised according to their location on Disko Island. The blue triangles are the samples in the north of Qeqertarsuaq, the black squares are from the east of Qeqertarsuaq and the green squares are from the western site.

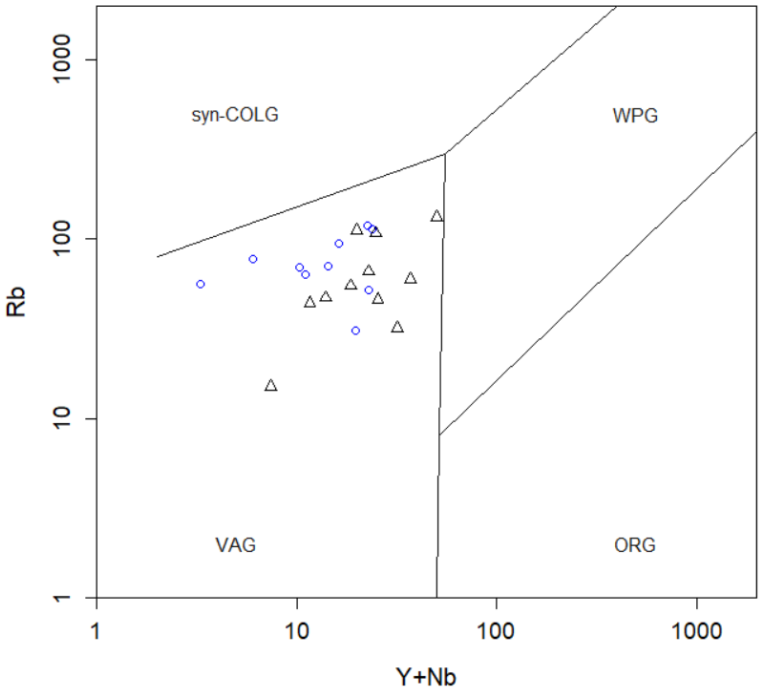

Figure 35: Diagram for geotectonic trace element discrimination for the orthogneiss samples. The Proterozoic orthogneisses are plotted with black triangles, while the Archean orthogneisses are plotted as blue dots.

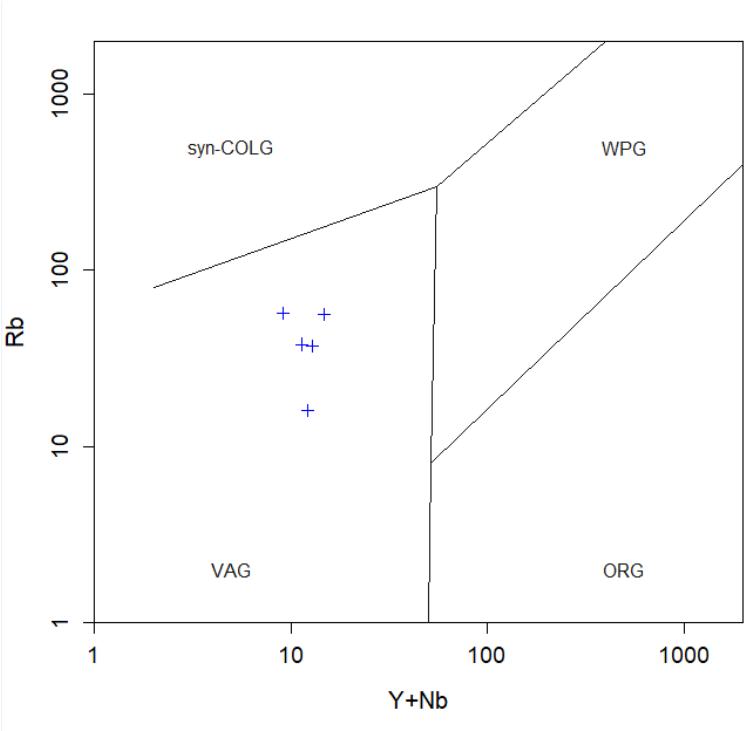

Figure 36: Diagram for geotectonic trace element discrimination for the Atâ Tonalites.

When comparing the figures, the samples show a similar distribution. The samples mostly plot in the VAG (volcanic arc granites) section. This supports the findings of the major elements, where the geotectonic distinction resulted in IAG/CAG.

For the direct comparison of the trace elements, the samples' trace elements are plotted against mid-ocean ridge basalts (MORB). VAG were described as: "*similar to, or more depleted than the MORB reservoir although there are exceptions*" by Pearce (1996).

One diagnostic feature of VAG is the low (Y+Nb) contents. Furthermore, they are characterized by enrichment in Th and Ce (Pearce, 1996). These patterns described can all be observed in Figure 37. The samples are clearly enriched in Th and Ce with respect to MORB. The depletion is strongest in the Y values, but the Nb values are also depleted.

The one sample with higher Y+Nb values, and enrichment through all elements portrayed, is EB-95, which was already an outlier in the classification plots, the only Monzodiorite.

In Figure 38, the trace elements of the orthogneiss samples are plotted against MORB. The orthogneisses also show the expected enrichment in Th and Ce. The depletion of Nb is not really the case, but Y is certainly depleted and fits the trend for VAG (Pearce, 1996). The trace elements of the Atâ Granites clearly display the VAG characteristics, with enriched Th and Ce values, and also show strongly depleted Y values in Figure 39. The Nb values are not really depleted, as the three values for the samples from Disko Island, but in a similar range with respect to Th and Ce.

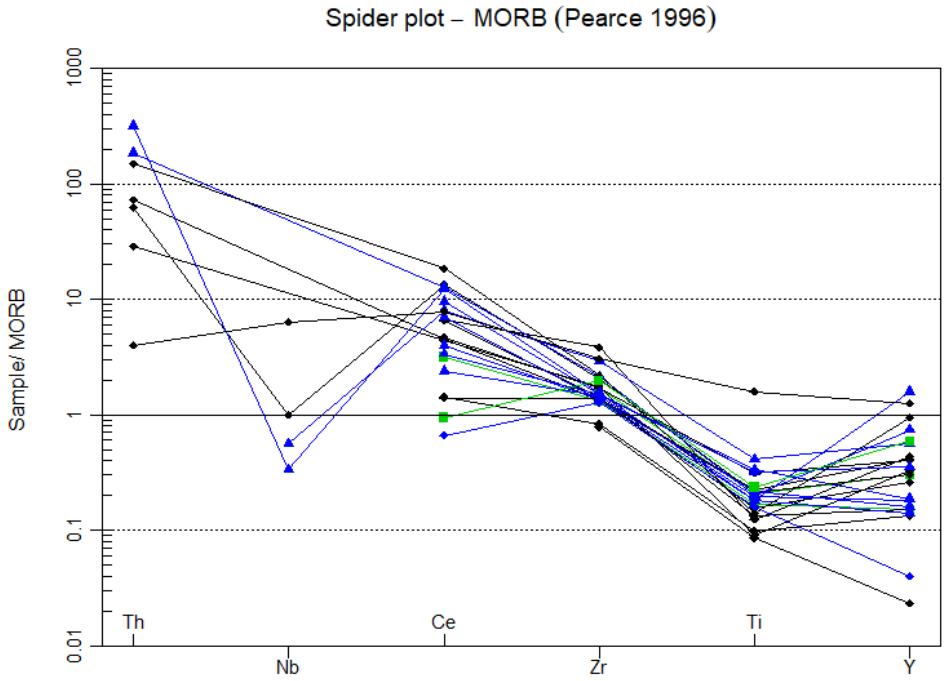

Figure 37: Trace elements of samples from Disko Island plotted against MORB compositions. The samples are coloured and symbolised according to their location on Disko Island. The blue triangles are the samples in the north of Qeqertarsuaq, the black squares are from the east of Qeqertarsuaq and the green squares are from the western site.

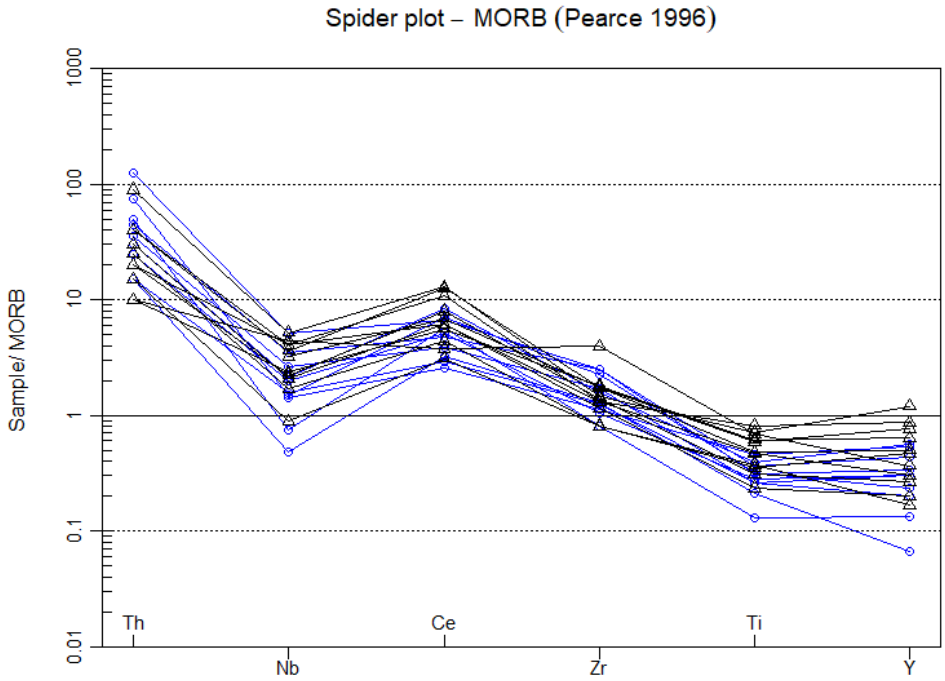

Figure 38: Trace elements of orthogneiss samples plotted against MORB compositions. The Proterozoic orthogneisses are plotted with black triangles and black lines, while the Archean orthogneisses are plotted as blue dots with blue lines.

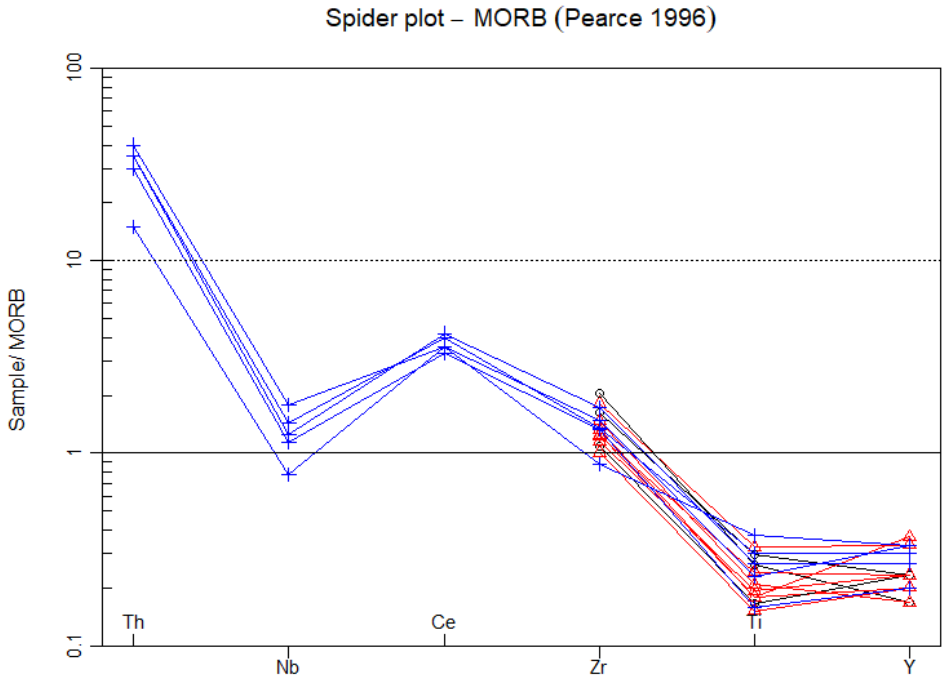

Figure 39: Trace elements of Atâ granite samples plotted against MORB compositions. The Atâ Granites and associated grey dykes are symbolised with red triangles and black circles respectively, while the Atâ Tonalites are symbolised with blue crosses.

The different comparisons shown in this chapter are strongly suggesting, that the sampled EBs from Disko Island originate either from the Atâ Granites (Kalsbeek et al., 1988; Kalsbeek & Skjernaa, 1999), on the eastern shore of Disko Bugt or from the orthogneisses (Kalsbeek, 2001) in the south of Disko Bugt. As there are no orthogneiss samples directly from the eastern shore of Disko Bugt, where Figure 27 shows orthogneisses, the assumption, that the sampled orthogneisses from Kalsbeek (2001) show similar characteristics and geochemistry to the mapped orthogneiss in eastern Disko Bugt, is likely.

The geochemical data and diagrams shown in this chapter support an allocation of the EBs sampled on Disko Island to the orthogneisses or the Atâ Granites (Kalsbeek, 2001; Kalsbeek et al., 1988). The allocation to the Atâ Granites group is more plausible just because of the proximity in comparison to the orthogneisses because we do not know about possible orthogneisses on northeastern Disko Bugt.

To come back to the second research goal of this master's thesis, hypothesis H1: "The erratic boulders originate from the western mainland coast of Greenland", can be accepted upon the here-stated similarities in geochemistry to the mainland orthogneisses and Atâ Granites. Not only do the geochemical trends and the geotectonic settings match, but the trace element compositions also show similarities, as far as they are reported.

The origin of the EBs on Disko Island being the western mainland coast of Greenland can also be supported by the general ice flow direction in this region. The ice flow in the LGM from east to the southwest is clearly supported by the overall bathymetry and the large Disko Trough in the Disko Bugt (Hogan et al., 2016).

5.3. Ice Thickness

Coming back to the research goals of this master's thesis, the first set hypothesis was:

"The plateaus show remnants of glacial periods prior to the LGM". The samples on the plateau were EB-190, EB-195, and EB-167. These samples yield ages of 104.1 ± 7 kyrs, 40.4 ± 2.8 kyrs, and 86.0 ± 5.9 kyrs. With regard to these ages, the first hypothesis can be accepted.

The samples on the basaltic plateau on Disko Island are remnants from previous glacials and were not deposited during the LGM.

The uncertainty for these ages is still very big, as the erosion rate has a huge impact on them, as shown in Figure 26. But erosion will only change the ages upwards and lead the samples to be older than thought, which enables the samples to be reported as pre-LGM with high certainty.

As described earlier in this thesis, these samples being much older than the LGM brings another component into this. EB-167 is the lowest sample, located at 720 m.a.s.l. The fact that this sample, and the ones with even higher elevation, are older than the LGM limits the ice thickness of the GrIS in Disko Bugt.

The here reported ages indicate that the GrIS did not overflow the plateaus on Disko during the LGM and therefore was not thicker than 720 m.a.s.l. This finding is in the same range as the thickness constraint Roberts et al. (2009) have made, where the maximum ice thickness of the GrIS was found to be below 810 m.a.s.l. in the region of Sisimut, south of Disko Bugt. Roberts et al. (2009) have dated their samples with both ^{10}Be and ^{26}Al. With the combined approach, uncertainty factors like erosion and surface shielding are far better constrained because the nuclides have different decay rates, which can be used for assessment of the exposure history (Darvill, 2013; Gosse & Phillips, 2001).

6. Conclusion

The 14 analysed ^{10}Be ages reported in this master's thesis fit into the deglaciation chronology of Disko Bugt and fill a gap of ^{10}Be exposure dating on Disko Island. The retreat of the GrIS on Disko Island occurred from 11.3 ± 0.9 to 9.6 ± 0.7 kyrs. The exposure ages are reported with ± their external errors. This is done to account for some of the uncertainty coming from various factors.

Samples on top of the basaltic plateaus yield much older ages that predate the LGM. This finding limits the maximum thickness of this branch of the GrIS in the LGM to below 720 m.a.s.l., where EB-167, with an age of 86.0 ± 5.9 kyrs is located.

Additionally, the geochemical analysis of 28 EBs from southern Disko Island resulted in granitic and granodioritic rocks with origin in a volcanic arc. Atâ Granites from eastern Disko Bugt and orthogneisses from southern Disko Bugt show many similarities and equal geotectonic settings. The erratic granitic boulders on Disko Island are therefore thought to originate from these sampled Atâ Granites (Kalsbeek et al., 1988; Kalsbeek & Skjernaa, 1999) in northeastern Disko Bugt, or possible offshoots of the orthogneisses (Kalsbeek, 2001) from southern Disko Bugt.

The origin of these EBs imply the flow direction of the GrIS to have been quite directly from east to west, with a southern deflection around Disko Island, where the plateaus are located, which were not overflown.

7. Outlook

The newly constrained ice thickness on Disko Island can be used for improved ice sheet modelling on the regional scale. With improved models, a better understanding of the reactions the GrIS showed during past climate changes can be achieved, which then can help future projections.

Additionally, further steps to better constrain the exposure ages of the measured EBs could be the analysis with a second nuclide, ^{26}Al, as an example. With the second nuclide, the erosional and the shielding factor can be improved, narrowing the age range of deglaciation down.

8. Challenges

In this master's thesis, I learned a lot and was able to work in different fields.

Most challenges were easily overcome with the very kind and competent help of many people, which I want to thank later.

First, I want to take the opportunity to tell about my learning outcomes and the challenges I faced during my work. The most challenging part of this thesis was the thin section analysis for me. As I have never attended any courses on petrology and thin section analysis, it was a new field for me. Already in the preparation step, while sawing the blocks for the thin sections, I faced a quite old rock saw, where I feared losing a finger. It did work out well in the end and I could get my thin sections and start with the analysis.

Working on the microscope and identifying the three main minerals (quartz, plagioclase, and alkali feldspars) was interesting and challenging at the same time.

After long meetings with Gerald Raab, where he showed me how to approach a thin section and the most important minerals for my samples, the basics were quite clear, and with the help of many tables, pictures, and the internet, I figured it out and was able to attain a basic understanding of this small part of the field of petrology.

9. Acknowledgments

This master's thesis would not have been possible without the help and assistance of a few people. I want to thank them individually here. First, my supervisor Dr. Gerald Raab, for helping and supporting me, often early in the morning (Canadian Time), on all my questions.

Further Prof. Dr. Markus Egli for the in-house support and help. Then I want to thank the lab technicians Yves and Dmitry for helping me in the laboratory steps at UZH and Michael, Lydia and Clara for the help at the laboratories at ETH.

Finally, I want to thank my friends and family for the support throughout this year and all the fellow students working on their master’s thesis’ in Y23 G10 for creating an atmosphere to work in, even if the internet connection was bad.

10. References

Balco, G. (2017). *Exposure age calculator V3*. https://hess.ess.washington.edu/math/v3/v3_age_in.html

Balco, G., Stone, J. O., Lifton, N. A., & Dunai, T. J. (2008). A complete and easily accessible means of calculating surface exposure ages or erosion rates from 10Be and 26Al measurements. In *Quaternary Geochronology* (Vol. 3, Issue 3, pp. 174–195). https://doi.org/10.1016/j.quageo.2007.12.001

Brouwer, P. (2010). *Theory of XRF* (3rd ed.). PANalytical B.V. www.panalytical.com

Cerling, T. E., & Craig, H. (2003). Geomorphology and in-situ cosmogenic isotopes. *Https://Doi.Org/10.1146/Annurev.Ea.22.050194.001421*, *22*, 273–317. https://doi.org/10.1146/ANNUREV.EA.22.050194.001421

Christl, M., Vockenhuber, C., Kubik, P. W., Wacker, L., Lachner, J., Alfimov, V., & Synal, H. A. (2013). The ETH Zurich AMS facilities: Performance parameters and reference materials. *Nuclear Instruments and Methods in Physics Research, Section B: Beam Interactions with Materials and Atoms*, *294*, 29–38. https://doi.org/10.1016/j.nimb.2012.03.004

Cockburn, H. A. P., & Summerfield, M. A. (2004). Geomorphological applications of cosmogenic isotope analysis. *Progress in Physical Geography*, *28*(1), 1–42. https://doi.org/10.1191/0309133304pp395oa

Corbett, L. B., Bierman, P. R., Rood, D. H., Caffee, M. W., Lifton, N. A., & Woodruff, T. E. (2017). Cosmogenic 26 Al/ 10 Be surface production ratio in Greenland. *Geophysical Research Letter*, *44*, 1350–1359. https://doi.org/10.1002/2016GL071276

Darvill, C. M. (2013). Cosmogenic nuclide analysis. In *British Society for Geomorphology Geomorphological Techniques* (Vol. 4, Issue 2).

de la Roche, H., Leterrier, J., Grandclaude, P., & Marchal, M. (1980). A classification of volcanic and plutonic rocks using R1R2-diagram and major-element analyses — Its relationships with current nomenclature. *Chemical Geology*, *29*(1–4), 183–210. https://doi.org/10.1016/0009-2541(80)90020-0

Dietrich, V. J., Carman, M. F., Wyttenbach, A., & McKee, E. H. (1984). Geochemistry of basalts from holes 519A, 520, 522B, and 524, Deep-Sea Drilling Project Leg 73 (South Atlantic). *Init. Report DSDP*, *73*, 579–601.

Dyke, L. M., Hughes, A. L. C., Murray, T., Hiemstra, J. F., Andresen, C. S., & Rodés, Á. (2014). Evidence for the asynchronous retreat of large outlet glaciers in southeast Greenland at the end of the last glaciation. *Quaternary Science Reviews*, *99*, 244–259. https://doi.org/10.1016/J.QUASCIREV.2014.06.001

Egli, M., Tikhomirov, D., Keller, T., & Brügger, Y. (2022). *Geochronology laboratory methods*.

El-Taher, A. (2012). Elemental analysis of granite by instrumental neutron activation analysis (INAA) and X-ray fluorescence analysis (XRF). *Applied Radiation and Isotopes*, *70*(1), 350–354. https://doi.org/10.1016/J.APRADISO.2011.09.008

Goehring, B. M., Brook, E. J., Linge, H., Raisbeck, G. M., & Yiou, F. (2008). Beryllium-10 exposure ages of erratic boulders in southern Norway and implications for the history of the Fennoscandian

Ice Sheet. *Quaternary Science Reviews*, *27*(3–4), 320–336. https://doi.org/10.1016/J.QUASCIREV.2007.11.004

Gool, J. A. M. van, Alsop, G. I., Árting, U. E., Garde, A. A., Knudsen, C., Krawiec, A. W., Mazur, S., Nygaard, J., Piazolo, S., Thomas, C. W., & Thrane, K. (2002). Precambrian geology of the northern Nagssugtoqidian orogen, West Greenland: mapping in the Kangaatsiaq area. *Geology of Greenland Survey Bulletin*, *191*, 13–23. https://doi.org/10.34194/GGUB.V191.5067

Gosse, J. C., & Phillips, F. M. (2001). Terrestrial in situ cosmogenic nuclides: theory and application. *Quaternary Science Reviews*, *20*(14), 1475–1560. https://doi.org/10.1016/S0277-3791(00)00171-2

Håkansson, L., Briner, J., Alexanderson, H., Aldahan, A., & Possnert, G. (2007). 10Be ages from central east Greenland constrain the extent of the Greenland ice sheet during the Last Glacial Maximum. *Quaternary Science Reviews*, *26*(19–21), 2316–2321. https://doi.org/10.1016/j.quascirev.2007.08.001

Hansen, B. U., Elberling, B., Humlum, O., & Nielsen, N. (2006). Meteorological trends (1991-2004) at Arctic Station, Central West Greenland (69°15'N) in a 130 years perspective. *Geografisk Tidsskrift*, *106*(1), 45–55. https://doi.org/10.1080/00167223.2006.10649544

Hogan, K. A., Ó Cofaigh, C., Jennings, A. E., Dowdeswell, J. A., & Hiemstra, J. F. (2016). Deglaciation of a major palaeo-ice stream in Disko Trough, West Greenland. *Quaternary Science Reviews*, *147*, 5–26. https://doi.org/10.1016/J.QUASCIREV.2016.01.018

Hollis, J. A., Keiding, M., Stensgaard, B. M., van Gool, J. A. M., & Garde, A. A. (2006). Evolution of Neoarchaean supracrustal belts at the northern margin of the North Atlantic Craton, West Greenland. *GEUS Bulletin*, *11*(11), 9–32. https://doi.org/10.34194/GEUSB.V11.4914

Humlum, O. (1998a). *Rock glaciers, Disko Island, Greenland, Version 1 [Data Set].* . Boulder, Colorado USA. National Snow and Ice Data Center.

Humlum, O. (1998b). The Climatic Significance of Rock Glaciers. *Permafrost and Periglacial Processes*, *9*(4), 375–395. https://doi.org/10.1002/(SICI)1099-1530(199810/12)9:4<375::AID-PPP301>3.0.CO;2-0

Ingólfsson, Ó., Frich, P., Funder, S., & Humlum, O. (1990). Paleoclimatic implications of an early Holocene glacier advance on Disko Island, West Greenland. *Boreas*, *19*(4), 297–311. https://doi.org/10.1111/J.1502-3885.1990.TB00133.X

Institute for Geochemistry and Petrology at ETH Zurich. (2022). *X-ray Fluorescence Analysis – High Pressure Geology | ETH Zurich*. https://highpressure.ethz.ch/facilities/analytical/xrf.html

Ivy-Ochs, S., & Kober, F. (2008). Surface exposure dating with cosmogenic nuclides. *E&G Quaternary Science Journal*, *57*(1–2), 179–209.

Janoušek, V., Farrow, C. M., & Erban, V. (2006). Interpretation of Whole-rock Geochemical Data in Igneous Geochemistry: Introducing Geochemical Data Toolkit (GCDkit). *Journal of Petrology*, *47*(6), 1255–1259. https://doi.org/10.1093/PETROLOGY/EGL013

Kalsbeek, F. (2001). Geochemical comparison between Archaean and Proterozoic orthogneisses from the Nagssugtoqidian orogen, West Greenland. *Precambrian Research*, *105*(2–4), 165–181. https://doi.org/10.1016/S0301-9268(00)00110-8

Kalsbeek, F., & Christiansen, F. G. (1992). Disko Bugt Project 1991, West Greenland. *Rapport Grønlands Geologiske Undersøgelse*, *155*, 36–41. https://doi.org/10.34194/RAPGGU.V155.8178

Kalsbeek, F., & Skjernaa, L. (1999). The Archaean Atâ intrusive complex (Atâ tonalite), north-east Disko Bugt, West Greenland. *Geology of Greenland Survey Bulletin*, *181*, 103–112. https://doi.org/10.34194/GGUB.V181.5118

Kalsbeek, F., Taylor, P. N., & Pidgeon, R. T. (1988). Unreworked Archaean basement and Proterozoic supracrustal rocks from northeastern Disko Bugt, West Greenland: implications for the nature of Proterozoic mobile belts in Greenland. *Canadian Journal of Earth Sciences*, *25*(5), 773–782. https://doi.org/10.1139/E88-072

Kawabata, H., Tatsumi, Y., Tani, K., Chang, Q., & Sato, K. (2005). Quantitative analyses of silicate rock major and trace elements by X-ray fluorescence spectrometer: Evaluation of analytical precision and sample preparation. In *FRONTIER RESEARCH ON EARTH EVOLUTION* (Vol. 2). https://www.researchgate.net/publication/267839674

Kelley, S. E., Briner, J. P., & Young, N. E. (2013). Rapid ice retreat in Disko Bugt supported by 10Be dating of the last recession of the western Greenland Ice Sheet. *Quaternary Science Reviews*, *82*, 13–22. https://doi.org/10.1016/J.QUASCIREV.2013.09.018

Kjær, K. H., Bjørk, A. A., Kjeldsen, K. K., Hansen, E. S., Andresen, C. S., Siggaard-Andersen, M. L., Khan, S. A., Søndergaard, A. S., Colgan, W., Schomacker, A., Woodroffe, S., Funder, S., Rouillard, A., Jensen, J. F., & Larsen, N. K. (2022). Glacier response to the Little Ice Age during the Neoglacial cooling in Greenland. In *Earth-Science Reviews* (Vol. 227). Elsevier B.V. https://doi.org/10.1016/j.earscirev.2022.103984

Kohl, C. P., & Nishiizumi, K. (1992). Chemical isolation of quartz for measurement of in-situ -produced cosmogenic nuclides. *Geochimica et Cosmochimica Acta*, *56*(9), 3583–3587. https://doi.org/10.1016/0016-7037(92)90401-4

Korschinek, G., Bergmaier, A., Faestermann, T., Gerstmann, U. C., Knie, K., Rugel, G., Wallner, A., Dillmann, I., Dollinger, G., von Gostomski, C. L., Kossert, K., Maiti, M., Poutivtsev, M., & Remmert, A. (2010). A new value for the half-life of 10Be by Heavy-Ion Elastic Recoil Detection and liquid scintillation counting. *Nuclear Instruments and Methods in Physics Research, Section B: Beam Interactions with Materials and Atoms*, *268*(2), 187–191. https://doi.org/10.1016/j.nimb.2009.09.020

Krusberski, N. (2010). *Exploring Potential Errors in XRF Analysis*. The Southern African Institute of Mining and Metallurgy: Analytical Challenges in Metallurgy, Johannesburg, South Africa, 2006.

Larsen, N. K., Funder, S., Linge, H., Möller, P., Schomacker, A., Fabel, D., Xu, S., & Kjær, K. H. (2016). A Younger Dryas re-advance of local glaciers in north Greenland. *Quaternary Science Reviews*, *147*, 47–58. https://doi.org/10.1016/J.QUASCIREV.2015.10.036

Lesnek, A. J., & Briner, J. P. (2018). Response of a land-terminating sector of the western Greenland Ice Sheet to early Holocene climate change: Evidence from 10Be dating in the Søndre Isortoq region. *Quaternary Science Reviews*, *180*, 145–156. https://doi.org/10.1016/J.QUASCIREV.2017.11.028

Lifton, N., Sato, T., & Dunai, T. J. (2014). Scaling in situ cosmogenic nuclide production rates using analytical approximations to atmospheric cosmic-ray fluxes. *Earth and Planetary Science Letters*, *386*, 149–160. https://doi.org/10.1016/J.EPSL.2013.10.052

Lloyd, J. M., Park, L. A., Kuijpers, A., & Moros, M. (2005). Early Holocene palaeoceanography and deglacial chronology of Disko Bugt, West Greenland. *Quaternary Science Reviews*, *24*(14–15), 1741–1755. https://doi.org/10.1016/j.quascirev.2004.07.024

Long, A. J., Roberts, D. H., & Rasch, M. (2003). New observations on the relative sea level and deglacial history of Greenland from Innaarsuit, Disko Bugt. *Quaternary Research*, *60*(2), 162–171. https://doi.org/10.1016/S0033-5894(03)00085-1

Maniar, P. D., & Piccoli, P. M. (1989). Tectonic discrimination of granitoids. *GSA Bulletin*, *101*(5), 635–643. https://doi.org/10.1130/0016-7606(1989)101<0635:TDOG>2.3.CO;2

Marrero, S. M., Phillips, F. M., Borchers, B., Lifton, N., Aumer, R., & Balco, G. (2016). Cosmogenic nuclide systematics and the CRONUScalc program. *Quaternary Geochronology*, *31*, 160–187. https://doi.org/10.1016/J.QUAGEO.2015.09.005

Michel-Lévy, A., & Lacroix, A. (1888). Les minéraux des roches. In *Bibliothèque recherche UMR 8198 Evo-Eco-Paléo CNRS - Université Lille 1* (Vol. 1). Librairie Polytechnique Baudry et cie (Paris). https://iris.univ-lille.fr/handle/1908/3113

Middlemost, E. A. K. (1994). Naming materials in the magma/igneous rock system. *Earth-Science Reviews*, *37*(3–4), 215–224. https://doi.org/10.1016/0012-8252(94)90029-9

Nisbet, E. G., Dietrich, V. J., & Esenwein, A. (1979). Routine trace element determination in silicate minerals and rocks by X-ray fluorescence. *Fortschritte Der Mineralogie*, *57*, 264–279.

Nishiizumi, K., Imamura, M., Caffee, M. W., Southon, J. R., Finkel, R. C., & McAninch, J. (2007). Absolute calibration of 10Be AMS standards. *Nuclear Instruments and Methods in Physics Research, Section B: Beam Interactions with Materials and Atoms*, *258*(2), 403–413. https://doi.org/10.1016/J.NIMB.2007.01.297

Ochs, M., & Ivy-Ochs, S. (1997). The chemical behavior of Be, Al, Fe, Ca and Mg during AMS target preparation from terrestrial silicates modeled with chemical speciation calculations. *Nuclear Instruments and Methods in Physics Research Section B: Beam Interactions with Materials and Atoms*, *123*(1–4), 235–240. https://doi.org/10.1016/S0168-583X(96)00680-5

Pearce, J. (1996). Sources and settings of granitic rocks. *Episodes Journal of International Geoscience*, *19*(4), 120–125. https://doi.org/10.18814/EPIIUGS/1996/V19I4/005

Pearce, J. A., Harris, N. B. W., & Tindle, A. G. (1984). Trace Element Discrimination Diagrams for the Tectonic Interpretation of Granitic Rocks. *Journal of Petrology*, *25*(4), 956–983. https://doi.org/10.1093/PETROLOGY/25.4.956

Porter, C., Morin, P., Howat, I., Noh, M.-J., Bates, B., Peterman, K., Keesey, S., Schlenk, M., Gardiner, J., Tomko, K., Willis, M., Kelleher, C., Cloutier, M., Husby, E., Foga, S., Nakamura, H., Platson, M., Wethington, Michael, Jr., Williamson, C., … Bojesen, M. (2022). *ArcticDEM - Strips, Version 4.1*. Harvard Dataverse, V1. https://doi.org/10.7910/DVN/OHHUKH

Previdi, M., Smith, K. L., & Polvani, L. M. (2021). Arctic amplification of climate change: A review of underlying mechanisms. *Environmental Research Letters*, *16*(9). https://doi.org/10.1088/1748-9326/AC1C29

Purdue University. (2007). *Froth Flotation*. https://www.physics.purdue.edu/primelab/MSL/froth_floatation.html

Raab, G. (2021). *Origin and timing of erratic boulders on Disko Island, Greenland* . https://www.geraldraab.com/projects/erratic-boulders-on-disko-island/

Raith, M., Raase, P., & Reinhardt, J. (2011). *Leitfaden zur Dünnschliffmikroskopie*.

Rantanen, M., Karpechko, A. Y., Lipponen, A., Nordling, K., Hyvärinen, O., Ruosteenoja, K., Vihma, T., & Laaksonen, A. (2022). The Arctic has warmed nearly four times faster than the globe since 1979. *Communications Earth & Environment 2022 3:1*, *3*(1), 1–10. https://doi.org/10.1038/s43247-022-00498-3

Roberts, D. H., Long, A. J., Schnabel, C., Davies, B. J., Xu, S., Simpson, M. J. R., & Huybrechts, P. (2009). Ice sheet extent and early deglacial history of the southwestern sector of the Greenland Ice Sheet. *Quaternary Science Reviews*, *28*(25–26), 2760–2773. https://doi.org/10.1016/J.QUASCIREV.2009.07.002

Søndergaard, A. S., Larsen, N. K., Lecavalier, B. S., Olsen, J., Fitzpatrick, N. P., Kjær, K. H., & Khan, S. A. (2020). Early Holocene collapse of marine-based ice in northwest Greenland triggered by atmospheric warming. *Quaternary Science Reviews*, *239*, 106360. https://doi.org/10.1016/J.QUASCIREV.2020.106360

Stosch, H. G. (2009). *Skript zur Kristalloptik II - Mineralmikroskopie* [Script]. Karlsruher Institut für Technologie (KIT).

Stosch, H. G. (2022). *QAPF (Streckeisen) diagram template for Excel*. https://doi.org/10.5281/ZENODO.5994130

Sulaymonova, V. A., Fuchs, M. C., Gloaguen, R., Möckel, R., Merchel, S., Rudolph, M., & Krbetschek, M. R. (2018). Feldspar flotation as a quartz-purification method in cosmogenic nuclide dating: A case study of fluvial sediments from the Pamir. *MethodsX*, *5*, 717–726. https://doi.org/10.1016/J.MEX.2018.06.014

Weidick, A., & Bennike, O. (2007). Quaternary glaciation history and glaciology of Jakobshavn Isbræ and the Disko Bugt region, West Greenland: A review. *Geological Survey of Denmark and Greenland Bulletin*, *14*, 1–78. https://doi.org/10.34194/GEUSB.V14.4985

Young, N. E., & Briner, J. P. (2015). Holocene evolution of the western Greenland Ice Sheet: Assessing geophysical ice-sheet models with geological reconstructions of ice-margin change. *Quaternary Science Reviews*, *114*, 1–17. https://doi.org/10.1016/J.QUASCIREV.2015.01.018

Young, N. E., Briner, J. P., Miller, G. H., Lesnek, A. J., Crump, S. E., Thomas, E. K., Pendleton, S. L., Cuzzone, J., Lamp, J., Zimmerman, S., Caffee, M., & Schaefer, J. M. (2020). Deglaciation of the Greenland and Laurentide ice sheets interrupted by glacier advance during abrupt coolings. *Quaternary Science Reviews*, *229*, 106091. https://doi.org/10.1016/J.QUASCIREV.2019.106091

11. Appendix

11.1. Data Tables for XRF measurements

Table 8: XRF results for major elements measured at ETH Zurich.

Major elements (wt%)	Basalt-Mix-1	Basalt-Mix-2	BO-1	BO-2	BO-4	EB-1	EB-113	EB-144	EB-151
SiO2	45.94	46.40	46.79	72.21	69.47	65.16	72.05	70.09	71.76
TiO2	3.68	2.68	1.59	0.30	0.25	0.48	0.19	0.14	0.12
Al2O3	11.95	13.58	14.83	13.75	15.20	17.01	14.00	15.30	15.38
Fe2O3	15.80	14.52	11.92	2.50	2.13	3.77	1.70	1.29	1.13
FeO	0.00	0.00	0.00	0.00	0.00	0.00	0.00	0.00	0.00
MnO	0.21	0.20	0.18	0.04	0.03	0.05	0.02	0.02	0.01
MgO	5.20	6.34	6.92	0.79	0.62	1.21	0.39	0.30	0.33
CaO	9.58	10.69	12.09	2.40	2.77	3.16	1.72	1.33	2.18
Na2O	2.62	2.48	2.16	3.70	4.80	5.17	3.40	3.67	4.94
K2O	0.62	0.37	0.24	2.63	1.71	1.98	4.56	5.83	2.29
P2O5	0.37	0.27	0.14	0.06	0.08	0.15	0.07	0.05	0.04
Cr2O3	0.01	0.01	0.03	0.00	0.00	0.00	0.00	0.00	0.00
H2O	0.00	0.00	0.00	0.00	0.00	0.00	0.00	0.00	0.00
CO2	0.00	0.00	0.00	0.00	0.00	0.00	0.00	0.00	0.00
LOI	0.80	0.80	0.68	0.37	0.52	0.59	0.73	0.67	0.53
Total	96.79	98.35	97.61	98.76	97.60	98.73	98.83	98.70	98.73

Table 9: Continuation of major element results measured with XRF at ETH.

Major elements (wt%)	EB-156	EB-167	EB-19	EB-190	EB-195	EB-200	EB-25	EB-250	EB-253
SiO2	76.18	72.59	73.86	72.05	66.46	94.15	65.46	71.42	70.80
TiO2	0.18	0.31	0.13	0.22	0.45	0.03	0.60	0.29	0.26
Al2O3	11.44	13.20	13.21	14.20	15.58	1.83	16.00	14.11	14.46
Fe2O3	3.07	2.54	1.41	1.88	3.93	0.49	4.11	2.42	1.63
FeO	0.00	0.00	0.00	0.00	0.00	0.00	0.00	0.00	0.00

MnO	0.02	0.04	0.02	0.03	0.07	0.01	0.05	0.02	0.03
MgO	0.22	0.46	0.28	0.42	1.49	0.18	1.45	0.70	0.39
CaO	1.57	1.55	1.15	1.65	3.48	0.19	2.96	2.61	1.80
Na2O	3.54	3.51	3.03	3.78	4.28	0.35	4.87	3.88	3.47
K2O	1.95	3.90	5.35	4.11	1.71	0.61	2.04	2.66	5.01
P2O5	0.02	0.08	0.05	0.05	0.21	0.02	0.24	0.12	0.06
Cr2O3	0.00	0.00	0.00	0.00	0.00	0.00	0.00	0.00	0.00
H2O	0.00	0.00	0.00	0.00	0.00	0.00	0.00	0.00	0.00
CO2	0.00	0.00	0.00	0.00	0.00	0.00	0.00	0.00	0.00
LOI	0.40	0.72	0.49	0.56	1.17	0.46	0.61	0.76	0.66
Total	98.60	98.91	98.98	98.98	98.84	98.32	98.40	98.99	98.57

Table 10: Continuation of major element results measured with XRF at ETH.

Major elements (wt%)	EB-45	EB-55	EB-59	EB-60	EB-65	EB-83	EB-95	EB-97	EB-98	EK-1
SiO2	70.65	68.39	67.44	69.87	70.75	70.18	51.73	71.14	66.05	70.49
TiO2	0.26	0.32	0.47	0.32	0.29	0.23	2.29	0.20	0.08	0.34
Al2O3	14.53	15.77	14.80	15.12	14.14	15.25	14.67	13.49	5.57	14.16
Fe2O3	2.27	2.81	3.94	2.35	2.82	2.05	13.07	2.05	0.60	3.19
FeO	0.00	0.00	0.00	0.00	0.00	0.00	0.00	0.00	0.00	0.00
MnO	0.03	0.04	0.07	0.03	0.03	0.02	0.16	0.03	0.03	0.05
MgO	0.71	0.81	1.56	0.78	0.75	0.72	2.72	0.32	0.22	0.82
CaO	2.28	3.49	3.75	3.00	1.88	2.52	6.53	1.11	12.43	2.96
Na2O	3.99	5.07	4.09	4.70	3.90	5.26	3.29	2.83	0.37	4.11
K2O	3.07	1.01	1.34	1.46	3.22	1.26	2.03	5.99	1.67	2.15
P2O5	0.08	0.09	0.11	0.12	0.08	0.07	0.41	0.06	0.02	0.07
Cr2O3	0.00	0.00	0.00	0.00	0.00	0.00	0.00	0.00	0.00	0.00
H2O	0.00	0.00	0.00	0.00	0.00	0.00	0.00	0.00	0.00	0.00
CO2	0.00	0.00	0.00	0.00	0.00	0.00	0.00	0.00	0.00	0.00
LOI	0.79	0.67	1.21	0.77	0.67	0.77	1.76	0.61	11.37	0.37
Total	98.68	98.48	98.78	98.51	98.55	98.33	98.69	97.83	98.42	98.72

Table 11: XRF results for trace elements measured at ETH.

Trace elements (ppm)	Basalt-Mix-1	Basalt-Mix-2	BO-1	BO-2	BO-4	EB-1	EB-113	EB-144	EB-151
Rb	8.7	7.2	3.4	64.7	62.2	74.9	97	249.9	49.1
Ba	116.9	61	46.8	622.8	386.8	512.2	1540.8	3504	748
Sr	304.8	233.3	198.6	188.2	312.3	450.9	345.3	455.1	497
Nb	14.4	9.2	5	0	0	0	0	0	0
Zr	227.2	162	87	153.2	116.9	134	129.3	74.5	70.7
Hf	0.6	1.1	0	1.3	0	0	2.3	0	0
Y	44.6	39.4	26	9	4.5	5.6	4.5	4	0.7
Ga	23	20.6	18	13.3	20.7	22.3	14.4	15.5	16.4
Zn	130.4	112.1	83	37.6	47.2	60.1	31.9	25.8	21.3
Cu	304.1	261	206.8	10.1	2.3	11.5	2.8	6	10.5
Co	55.5	51.5	48.7	16.9	16.5	13.8	21	13.4	12.8
Cr	58.7	96.1	207.6	0	0	0	0	0	0
V	523.9	433.3	346.9	15.3	22.4	48.5	15.5	14.3	12.3
Sc	42	43.6	47.3	10.3	8.8	9.8	8	6.9	7.2
La	7	1.5	0	12.3	12.3	52.6	53.2	14.2	4.6
Ce	65	29	20.1	0	31.6	95.2	65.4	14.3	0
Nd	30	23	14.7	0	6.2	37.5	28.1	9.6	6.7
Pb	0	0	0	0	0	0	0	3.3	0
Th	7.7	8	4	0	0	0	0	0	0
U	0	0	1	0.5	0	0	1	0	0
W	75.3	11.9	51.6	148.5	139.7	70.1	221	257.8	207.1

Table 12: Continuation of trace elements measured with XRF at ETH.

Trace elements (ppm)	EB-156	EB-167	EB-19	EB-190	EB-195	EB-200	EB-25	EB-250	EB-253
Rb	43.3	231.7	211.8	130.7	73	13.5	122.6	71.5	128.3
Ba	515.3	540.7	817.2	844.3	145.6	246.7	211.1	1027.6	1847.5
Sr	132.7	97.3	209.5	295.1	316.5	67.5	276.7	391.6	419.7
Nb	0	2.7	0	0	0	0	1.5	0	0.9

Zr	345.6	181.2	157.9	121.6	153.9	11.1	261	130.3	138.1
Hf	7.5	3.7	4.4	1.9	2.6	0	5.4	1.3	1.2
Y	13.2	9.1	9.8	7.8	12.2	0	16.9	5.5	47.3
Ga	12.9	17.8	15.5	16.1	18.6	0	23.1	15.6	16.1
Zn	31.1	51.8	26.2	42.3	70.7	5.3	92.6	38.2	29.1
Cu	20.8	3.4	3	6.4	23.6	1.1	13.9	1.4	4.4
Co	22.8	18.3	25.8	15.9	26.6	29.7	11.4	14.5	8.9
Cr	0	0	0	0	0.8	0	0.6	0	0
V	4.5	19.1	11.2	18.6	46.6	7.7	40.2	30.7	16.3
Sc	9.8	9.5	6.2	6.8	16.1	5.7	10.3	7.2	9.6
La	38.2	18.1	25.1	35.9	33.6	3	41.2	16.3	56.7
Ce	66.2	133.8	43.9	45.8	46.9	0	80.5	23.8	124.3
Nd	27.7	15.3	11	18.8	23.9	2.5	33	21.3	52.4
Pb	0	5.3	8.3	13.6	0	0	0	0	1.3
Th	0	12.4	5.7	14.4	0	0	0	0	63.4
U	1	0	1.2	0	1.4	0.1	2.3	0	0
W	207.7	225.3	274	147.7	141.4	303.9	56.4	111.6	105.8

Table 13: Continuation of trace elements measured with XRF at ETH.

Trace elements (ppm)	EB-45	EB-55	EB-59	EB-60	EB-65	EB-83	EB-95	EB-97	EB-98	EK-1
Rb	88.1	39.2	59.1	50	104.9	41.9	75	287.6	42.7	57.4
Ba	844.3	172.8	235.5	305.1	725.5	286.5	429.3	815	548.3	557.9
Sr	349.2	398.4	253.6	405.7	273.9	415.9	312.4	194.3	130.3	222.4
Nb	0	0	0	0	0	0	17.2	0	0	0
Zr	122.6	125.1	135.7	122.4	191.5	113.9	273.6	196.6	57.8	176.4
Hf	0	0.8	2.7	0	1.6	0	5.5	1.8	1.8	3.7
Y	4.2	12.4	10.5	4.8	22	1.2	37.9	28.4	0.2	17.6
Ga	17	20.3	15	16.9	20	19.2	23.1	14.9	3.6	16.3
Zn	46.3	50.4	51.9	51.6	57.3	23.9	151	19.6	6.9	40.9
Cu	8.3	5.6	21.9	7.6	6.7	7.3	21.4	2.5	4.6	9.4
Co	18	14.4	19.5	13.9	9.6	13.9	37.5	17.3	19.9	9.7

Cr	0	0	1.8	0	0	0	25.2	0	4	0
V	22.7	35.8	54.6	22.6	16.3	22.8	217.3	20.2	13.8	35.7
Sc	9.2	13.2	13.4	5.7	14.2	8.2	27.5	9.2	8.6	13.5
La	48.4	12	31	27.3	63.4	11.7	33	98.3	16.9	13.4
Ce	70.1	14	33.5	40	126.7	6.6	78.4	185.3	5.3	9.4
Nd	23.6	10	19.2	16.4	42.3	3.2	43.7	77.6	0	13.1
Pb	0	0	0	0	13.4	0	0	8.9	0	0
Th	0	0	0	0	37	0	0.8	29.6	0	0
U	0	0	0	0.6	1.2	0	2.3	1.1	0	0
W	114.7	141.8	139.3	106.1	105.4	149.8	84.7	170.1	253.3	74.3

Table 14: Raw results of XRF measurements at UZH. Element compositions in wt%.

	Sample Names								
	EB-190	EK-1	EB-151	EB-195	BO-2	EB-253	EB-144	EB-156	EB-167
Na	2.774	3.208	3.383	2.93	2.911	2.577	2.737	3.134	2.875
Mg	0.4692	0.854	0.3534	1.318	0.859	0.4351	0.3191	0.307	0.4335
Al	7.063	7.774	7.52	7.534	7.587	7.119	7.631	6.786	7.455
Si	35.74	30.85	36.06	31.9	31.6	34.77	35.75	34.73	32.87
P	0.0003	0.01674	0.0003	0.07685	0.00829	0.00464	0.0003	0.0003	0.01813
S	0.0002	0.00793	0.00102	0.0039	0.01608	0.00253	0.00179	0.01047	0.00296
Cl	0.01234	0.00945	0.01669	0.01313	0.00666	0.01565	0.0067	0.00791	0.0083
K	3.734	2.249	2.056	1.488	2.763	4.434	5.155	2.092	3.913
Ca	1.181	2.35	1.558	2.349	1.918	1.277	0.9592	1.258	1.264
Ti	0.1452	0.2445	0.08743	0.2839	0.2518	0.1563	0.09297	0.141	0.2207
V	0.00091	0.00256	0.0008	0.00419	0.00063	0.00047	0.0001	0.0001	0.00223
Cr	0.00029	0.00138	0.00032	0.00121	0.00112	0.00018	0.00124	0.00018	0.00095
Mn	0.0221	0.04124	0.01038	0.05129	0.03201	0.01772	0.01598	0.02059	0.03278
Fe	1.186	2.279	0.796	2.792	1.973	1.049	0.8711	2.089	1.904
Co	0.00056	0.00061	0.0011	0.00338	0.00212	0.00231	0.00085	0.00197	0.00169
Ni	0.00069	0.00139	0.00062	0.00201	0.00107	0.00045	0.00076	0.00087	0.00099
Cu	0.00013	0.00056	0.00009	0.00025	0.00086	0.00013	0.00017	0.00205	0.00012
Zn	0.00444	0.00472	0.00258	0.00723	0.00463	0.00316	0.00285	0.00365	0.00571
Ga	0.00212	0.00222	0.00215	0.00221	0.00209	0.002	0.00194	0.00189	0.00255

Ge	0.00005	0.00005	0.00005	0.00005	0.00005	0.00005	0.00005	0.00005	0.00005
As	0.00004	0.00004	0.00004	0.00004	0.00004	0.00004	0.00004	0.00004	0.00004
Se	0.00002	0.00002	0.00002	0.00002	0.00002	0.00002	0.00002	0.00002	0.00002
Br	0.00006	0.00002	0.00012	0.00003	0.00002	0.00009	0.00004	0.00002	0.00003
Rb	0.01321	0.00638	0.00536	0.00732	0.00747	0.01295	0.02454	0.00487	0.02427
Sr	0.0288	0.02454	0.04966	0.03056	0.02074	0.04061	0.04446	0.01435	0.01052
Y	0.00062	0.00189	0.00008	0.00117	0.00097	0.00454	0.00043	0.00123	0.0009
Zr	0.01097	0.01846	0.00733	0.01479	0.01504	0.0128	0.00711	0.03108	0.0185
Nb	0.00041	0.00046	0.00005	0.00057	0.00042	0.00107	0.0002	0.0003	0.00123
Mo	0.00023	0.00017	0.00021	0.00019	0.00016	0.00017	0.00022	0.00017	0.00031
Ru	0.00005	0.00005	0.00005	0.00005	0.00005	0.00005	0.00005	0.00005	0.00005
Rh	0.00005	0.00005	0.00005	0.00005	0.00005	0.00005	0.00005	0.00005	0.00005
Pd	0.00005	0.00002	0.00005	0.00005	0.00005	0.00005	0.00005	0.00005	0.00005
Ag	0.00005	0.00005	0.00005	0.00005	0.00005	0.00005	0.00005	0.00005	0.00005
Cd	0.00004	0.00004	0.00008	0.00003	0.00003	0.00003	0.00002	0.00002	0.00002
In	0.00005	0.00005	0.00005	0.00005	0.00005	0.00005	0.00005	0.00005	0.00005
Sn	0.0001	0.00015	0.00016	0.00005	0.00005	0.00025	0.00008	0.00009	0.00005
Sb	0.00005	0.00005	0.00005	0.00005	0.00005	0.00005	0.00005	0.00005	0.00005
Te	0.00005	0.00005	0.00005	0.00005	0.00005	0.00005	0.00007	0.00007	0.00005
I	0.00007	0.00007	0.00007	0.00007	0.00007	0.00007	0.00458	0.00007	0.00007
Cs	0.00128	0.00086	0.00203	0.00119	0.00106	0.00115	0.0002	0.00115	0.00139
Ba	0.07222	0.0513	0.06595	0.01351	0.05499	0.1478	0.2582	0.04816	0.04586
La	0.00579	0.00342	0.0052	0.00512	0.0032	0.00773	0.0027	0.00574	0.00494
Ce	0.00896	0.00466	0.00655	0.00876	0.00434	0.01338	0.00379	0.01012	0.01474
Pr	0.0071	0.0057	0.00932	0.007	0.00625	0.00732	0.00052	0.00694	0.00662
Nd	0.00995	0.00765	0.01031	0.00915	0.00703	0.01215	0.00247	0.01036	0.00842
Sm	0.00081	0.00081	0.00081	0.00081	0.00081	0.00083	0.00081	0.00081	0.00081
Hf	0.0002	0.00056	0.0002	0.00013	0.00009	0.0002	0.0002	0.00042	0.0002
Ta	0.00016	0.00016	0.00016	0.00016	0.00016	0.00016	0.00016	0.00016	0.00016
W	0.01577	0.00898	0.02243	0.01462	0.01776	0.01056	0.02874	0.02523	0.02664
Au	0.00004	0.00004	0.00004	0.00004	0.00004	0.00004	0.00004	0.00004	0.00004
Hg	0.00007	0.00007	0.00007	0.00007	0.00007	0.00007	0.00007	0.00007	0.00007
Tl	0.00005	0.00007	0.00007	0.00007	0.00007	0.00003	0.00019	0.00007	0.00012

Pb	0.0035	0.00076	0.0013	0.00071	0.00111	0.00259	0.0028	0.00143	0.00279
Bi	0.00005	0.00005	0.00005	0.00005	0.00005	0.00005	0.00005	0.00005	0.00005
Th	0.00273	0.0007	0.00004	0.00059	0.00079	0.00808	0.00074	0.00095	0.00364
U	0.00039	0.0001	0.00021	0.0002	0.00012	0.00063	0.00006	0.00008	0.00004

Table 15: Continuation of XRF results measured at UZH.

	Sample Names								
	EB-98	EB-55	EB-95	EB-19	EB-250	EB-1(3)	EB-59	BO-1	EB-45
Na	0.397	4.172	2.811	2.707	3.367	4.448	3.531	2.141	3.154
Mg	0.3008	0.883	1.707	0.3312	0.746	1.155	1.431	3.552	0.793
Al	3.561	8.915	7.697	7.506	8.028	9.635	8.215	8.768	8.131
Si	30.23	31.17	24.5	33.52	32.1	28.87	30.53	23.49	31.21
P	0.0003	0.02959	0.2142	0.0003	0.047	0.07375	0.04834	0.09522	0.01788
S	0.00861	0.0093	0.0899	0.0093	0.0002	0.00657	0.00847	0.01836	0.00109
Cl	0.00164	0.00987	0.05074	0.01002	0.01838	0.05033	0.01456	0.0002	0.01545
K	1.402	1.008	1.709	5.122	2.74	1.964	1.335	0.2322	3.165
Ca	9.864	2.678	4.097	0.8688	2.133	2.495	2.822	7.794	1.867
Ti	0.05343	0.222	1.244	0.08726	0.2234	0.3432	0.3393	0.9532	0.1991
V	0.00113	0.00376	0.01844	0.0004	0.00179	0.00429	0.00609	0.03238	0.00166
Cr	0.00159	0.0009	0.00259	0.00048	0.00055	0.00069	0.00199	0.01804	0.00049
Mn	0.02321	0.02921	0.1065	0.01579	0.02037	0.03903	0.05855	0.1271	0.02941
Fe	0.4551	2.087	8.929	0.9725	1.749	2.868	3.137	8.221	1.704
Co	0.00054	0.00157	0.00335	0.00276	0.00184	0.00162	0.00294	0.0054	0.00215
Ni	0.00107	0.00107	0.00236	0.00093	0.00095	0.00123	0.00209	0.01073	0.00095
Cu	0.00005	0.00017	0.00084	0.00011	0.00007	0.00069	0.0015	0.02014	0.00005
Zn	0.00109	0.00575	0.01449	0.00294	0.00434	0.00681	0.00596	0.00746	0.00537
Ga	0.00084	0.00247	0.00243	0.00207	0.00225	0.00262	0.00194	0.00189	0.00237
Ge	0.00005	0.00005	0.00005	0.00005	0.00005	0.00005	0.00005	0.00005	0.00005
As	0.00004	0.00004	0.00004	0.00004	0.00004	0.00004	0.00052	0.00004	0.00004
Se	0.00002	0.00002	0.00002	0.00002	0.00002	0.00002	0.00002	0.00002	0.00002
Br	0.00001	0.00003	0.00037	0.00007	0.00003	0.00006	0.00008	0.00002	0.00005
Rb	0.00394	0.00455	0.00729	0.02153	0.00798	0.00819	0.00671	0.00057	0.00991
Sr	0.0113	0.04141	0.03011	0.02126	0.04211	0.04818	0.02706	0.01983	0.03815

Y	0.00009	0.00117	0.00332	0.00096	0.00053	0.00061	0.0011	0.00281	0.00046
Zr	0.00529	0.01278	0.02489	0.01524	0.01205	0.01262	0.01313	0.00776	0.0123
Nb	0.00009	0.0005	0.00174	0.00046	0.00029	0.00033	0.00058	0.00048	0.00038
Mo	0.00025	0.00015	0.00031	0.00451	0.00011	0.00015	0.00017	0.00026	0.0002
Ru	0.00005	0.00005	0.00005	0.00005	0.00005	0.00005	0.00005	0.00005	0.00005
Rh	0.00002	0.00005	0.00005	0.00005	0.00005	0.00005	0.00005	0.00005	0.00005
Pd	0.00005	0.00005	0.00005	0.00005	0.00005	0.00005	0.00005	0.00005	0.00005
Ag	0.00005	0.00005	0.00005	0.00005	0.00005	0.00005	0.00005	0.00005	0.00005
Cd	0.00011	0.00003	0.00003	0.00006	0.00006	0.00002	0.00002	0.00003	0.00003
In	0.00005	0.00005	0.00005	0.00005	0.00005	0.00005	0.00005	0.00005	0.00005
Sn	0.00004	0.00005	0.00005	0.00009	0.0002	0.00005	0.00005	0.00005	0.00005
Sb	0.00006	0.00005	0.00005	0.00005	0.00005	0.00005	0.00005	0.00005	0.00005
Te	0.00005	0.00005	0.00005	0.00011	0.00059	0.00005	0.00005	0.00005	0.00005
I	0.00007	0.00007	0.00007	0.00257	0.00314	0.00007	0.00007	0.00007	0.00007
Cs	0.00218	0.0016	0.00021	0.00203	0.00112	0.00143	0.0012	0.00014	0.00058
Ba	0.04254	0.01701	0.03404	0.07241	0.09429	0.0469	0.02267	0.00311	0.07375
La	0.00488	0.00473	0.00344	0.00659	0.00627	0.00744	0.00444	0.00078	0.00584
Ce	0.00448	0.00735	0.00696	0.01035	0.00952	0.01273	0.00717	0.00246	0.01023
Pr	0.0102	0.00844	0.00398	0.01032	0.0092	0.00822	0.00676	0.00267	0.00525
Nd	0.0107	0.01022	0.0068	0.01193	0.01139	0.01107	0.00838	0.00403	0.00749
Sm	0.00081	0.00081	0.00081	0.00081	0.00081	0.00081	0.00081	0.00081	0.00081
Hf	0.0002	0.00007	0.00062	0.0002	0.00011	0.00012	0.00013	0.00096	0.0002
Ta	0.00016	0.00016	0.00016	0.00016	0.00016	0.00016	0.00016	0.00016	0.00016
W	0.02394	0.01544	0.00811	0.03214	0.01345	0.00779	0.01645	0.00498	0.01397
Au	0.00004	0.00004	0.00006	0.00004	0.00004	0.00004	0.00004	0.00005	0.00004
Hg	0.00007	0.00007	0.00007	0.00007	0.00007	0.00007	0.00007	0.00007	0.00007
Tl	0.00007	0.00007	0.00007	0.00012	0.00007	0.00007	0.00007	0.00007	0.00007
Pb	0.00064	0.00101	0.001	0.003	0.00124	0.00126	0.00124	0.00006	0.00158
Bi	0.00005	0.00005	0.00005	0.00005	0.00005	0.00005	0.00005	0.00005	0.00005
Th	0.00004	0.00079	0.00054	0.00292	0.00048	0.00139	0.00099	0.00013	0.0016
U	0.00004	0.00038	0.00004	0.00023	0.00031	0.00037	0.00021	0.00004	0.0003

Table 16: Continuation of XRF results measured at UZH.

	Sample Names								
	EB-83	EB-25	EB-113	EB-65	EB-60	EB-97	BO-4	EB-200	Basalt-Mix-1
Na	3.706	3.893	2.607	2.757	3.424	2.488	3.77	0.548	2.819
Mg	0.59	1.35	0.4083	0.633	0.714	0.3717	0.739	0.1646	2.48
Al	7.483	9.003	6.839	6.839	7.31	7.604	8.478	1.179	7.59
Si	35.13	28.3	34.92	34.8	33.91	31.48	30.83	44.61	24.07
P	0.0126	0.1291	0.00566	0.01861	0.04009	0.00246	0.02384	0.0003	0.2466
S	0.01249	0.00614	0.0002	0.0082	0.00442	0.0002	0.00553	0.00216	0.0047
Cl	0.03239	0.01498	0.01892	0.03504	0.01639	0.01301	0.01347	0.03662	0.0002
K	1.088	2.074	4.012	2.882	1.301	5.962	1.834	0.6957	0.6075
Ca	1.807	2.337	1.226	1.329	2.16	0.8779	2.236	0.1702	6.329
Ti	0.151	0.4087	0.1282	0.1993	0.2094	0.1428	0.1989	0.03588	2.009
V	0.00249	0.00329	0.00072	0.0011	0.00228	0.00161	0.00234	0.0005	0.04749
Cr	0.00058	0.00165	0.00016	0.0004	0.00056	0.00038	0.00085	0.00064	0.00519
Mn	0.01524	0.04331	0.01512	0.02471	0.02376	0.01964	0.02864	0.0081	0.1433
Fe	1.43	3.164	1.131	1.902	1.64	1.445	1.657	0.3679	10.71
Co	0.00095	0.00085	0.0022	0.0013	0.00163	0.00117	0.00193	0.00424	0.00742
Ni	0.00094	0.00164	0.00072	0.0011	0.00083	0.00091	0.00107	0.00093	0.00472
Cu	0.00053	0.00006	0.00008	0.00046	0.00034	0.00005	0.00005	0.00013	0.02934
Zn	0.00262	0.01012	0.00352	0.00584	0.00519	0.00244	0.00563	0.00101	0.01143
Ga	0.00225	0.00292	0.00193	0.00223	0.00211	0.00238	0.00278	0.00059	0.00223
Ge	0.00005	0.00005	0.00005	0.00005	0.00005	0.00005	0.00005	0.00005	0.00015
As	0.00004	0.00004	0.00004	0.00004	0.00004	0.00004	0.00004	0.00004	0.00004
Se	0.00002	0.00002	0.00002	0.00002	0.00002	0.00002	0.00002	0.00002	0.00002
Br	0.00007	0.00001	0.0001	0.00005	0.00004	0.00005	0.00005	0.00006	0.00002
Rb	0.00449	0.01302	0.01006	0.01037	0.00526	0.03056	0.00709	0.0018	0.00126
Sr	0.04126	0.03022	0.03373	0.02661	0.0399	0.02075	0.03432	0.00729	0.03035
Y	0.00019	0.00168	0.00032	0.00222	0.00047	0.00301	0.00046	0.0001	0.00433
Zr	0.01125	0.02638	0.01217	0.01822	0.01334	0.0202	0.0133	0.00216	0.02008
Nb	0.0002	0.00105	0.00017	0.00096	0.0004	0.00112	0.00039	0.00003	0.00117

Mo	0.00019	0.00023	0.0002	0.00015	0.00021	0.00022	0.00019	0.00017	0.00024
Ru	0.00005	0.00002	0.00005	0.00005	0.00005	0.00005	0.00005	0.00005	0.00005
Rh	0.00005	0.00001	0.00005	0.00005	0.00005	0.00005	0.00005	0.00005	0.00005
Pd	0.00002	0.00005	0.00005	0.00005	0.00005	0.00005	0.00005	0.00005	0.00005
Ag	0.00005	0.00005	0.00005	0.00005	0.00005	0.00005	0.00005	0.00005	0.00005
Cd	0.0001	0.00005	0.00005	0.00003	0.00003	0.00003	0.00003	0.00002	0.00004
In	0.00005	0.00005	0.00005	0.00005	0.00005	0.00005	0.00005	0.00005	0.00005
Sn	0.00009	0.00005	0.00014	0.00015	0.00005	0.00013	0.00005	0.00005	0.00005
Sb	0.00005	0.00005	0.00005	0.00005	0.00005	0.00005	0.00005	0.00005	0.00005
Te	0.00005	0.00005	0.00005	0.00005	0.00005	0.00005	0.00005	0.0003	0.00005
I	0.00007	0.00007	0.00007	0.00007	0.00007	0.00007	0.00007	0.00007	0.00007
Cs	0.00178	0.00084	0.00113	0.0021	0.00095	0.00133	0.00102	0.00129	0.00014
Ba	0.02773	0.01839	0.1256	0.06274	0.02824	0.06615	0.03537	0.02497	0.00858
La	0.00435	0.00548	0.00737	0.00897	0.0046	0.01037	0.00335	0.00366	0.00201
Ce	0.00633	0.01049	0.01128	0.01641	0.00762	0.01919	0.00558	0.00511	0.00537
Pr	0.0084	0.00599	0.00753	0.0104	0.00587	0.00816	0.00527	0.00708	0.00371
Nd	0.00904	0.00852	0.01077	0.01411	0.00758	0.01401	0.00635	0.00738	0.00703
Sm	0.00081	0.00081	0.00081	0.00096	0.00081	0.00175	0.00081	0.00081	0.00005
Hf	0.0002	0.00046	0.0002	0.00039	0.00009	0.00043	0.00005	0.0002	0.00031
Ta	0.00016	0.00016	0.00016	0.00016	0.00016	0.00016	0.00016	0.00016	0.00033
W	0.01642	0.00659	0.02416	0.01095	0.0115	0.0202	0.01643	0.03772	0.00487
Au	0.00004	0.00004	0.00004	0.00004	0.00004	0.00004	0.00004	0.00004	0.00007
Hg	0.00007	0.00007	0.00007	0.00007	0.00007	0.00007	0.00007	0.00007	0.00007
Tl	0.00007	0.00007	0.00003	0.00003	0.00007	0.00017	0.00007	0.00002	0.00007
Pb	0.00071	0.00146	0.00245	0.00322	0.0011	0.00371	0.00146	0.00044	0.00024
Bi	0.00005	0.00005	0.00005	0.00005	0.00005	0.00005	0.00005	0.00005	0.00005
Th	0.00017	0.00253	0.00152	0.00553	0.00069	0.00561	0.00055	0.00053	0.00004
U	0.00027	0.0002	0.00035	0.00043	0.00027	0.00036	0.00027	0.00003	0.00009

Table 17: Element data for the orthogneisses reported by Kalsbeek (2001).

	Ortho1	Ortho2	Ortho3	Ortho4	Ortho5	Ortho6	Ortho7	Ortho8	Ortho9	Ortho10
SiO2	70.84	70.03	70.83	68.9	70.81	65.9	71.67	75.8	68.85	57.49
TiO2	0.41	0.38	0.38	0.45	0.31	0.57	0.46	0.19	0.52	0.67
Al2O3	14.97	15.2	14.95	15.07	15.18	15.78	13.25	12.59	15.6	16.97
FeO	2.46	2.42	2.55	3.69	2.1	4.82	3.14	1.64	3.17	6.12
MnO	0.03	0.03	0.03	0.04	0.03	0.07	0.03	0.02	0.05	0.1
MgO	1.18	1.24	1.2	1.33	0.91	1.8	1.39	0.42	1.42	4.46
CaO	2.95	2.18	2.95	2.14	2.96	4.12	3.3	1.65	2.96	7.57
Na2O	4.44	4.49	4.45	4.68	4.33	3.95	3.44	3.63	4.54	3.91
K2O	1.61	2.87	1.59	2.51	2.29	1.48	1.67	3.14	1.8	1.05
P2O5	0.12	0.13	0.1	0.09	0.12	0.2	0.35	0.08	0.16	0.12
Volat.	0.51	0.49	0.49	0.6	0.33	0.7	0.49	0.2	0.56	0.97
Total	99.53	99.45	99.53	99.48	99.35	99.38	99.2	99.35	99.64	99.43
Rb	71	95	70	114	56	52	64	78	120	31
Ba	210	425	164	233	588	385	450	675	285	104
Pb	9	8	7	12	8	6	7	8	7	3
Sr	264	145	195	134	434	310	184	265	235	253
La	24	21	13	31	16	44	38	31	25	9
Ce	52	39	29	66	32	84	70	57	48	26
Nd	19	17	11	26	14	32	29	21	20	15
Y	9	9	6	10	2	17	7	4	13	16
Th	5	7	3	25	3	6	15	10	9	0
Zr	94	152	111	223	114	142	205	73	225	102
Hf	0	0	3.3	5.6	0	3.7	0	0	5.5	2.4
Nb	5.3	7.2	4.3	14	1.3	5.8	4	2	9.5	3.8
Zn	48	41	47	50	46	74	53	23	59	78
Cu	7	8	3	5	11	15	10	11	5	18
Ni	12	10	10	10	8	15	10	6	11	85
Sc	3	3	5	6	3	10	4	0	6	18
V	35	28	34	34	22	70	26	19	39	129
Cr	14	10	12	12	9	17	15	6	10	89
Ga	18	21	19	20	20	21	17	14	22	20

Table 18: Element data for the orthogneisses reported by Kalsbeek (2001).

	Ortho 11	Ortho 12	Ortho 13	Ortho 14	Ortho 15	Ortho 16	Ortho 17	Ortho 18	Ortho 19	Ortho 20	Ortho 21
SiO2	51.02	61.78	63.13	57.59	69.21	49.94	49.56	59.37	67.88	65.62	66.99
TiO2	0.86	0.69	0.68	0.89	0.34	1.04	1.18	0.51	0.45	1	0.54
Al2O3	18.7	16.61	16.85	17.81	15.59	17.92	15.03	16.93	15.78	14.3	15.57
FeO	9.1	4.65	4.21	5.99	2.27	9.29	10.47	6.08	2.62	5.85	4
MnO	0.17	0.08	0.05	0.09	0.05	0.21	0.18	0.13	0.04	0.07	0.07
MgO	3.76	3.12	2.16	3.33	1.11	2.81	5.46	3.15	1.52	2.67	2.06
CaO	7.94	4.77	3.96	6.48	2.97	7.52	10.31	5.89	3.29	4.07	5.01
Na2O	4.11	3.93	4.86	4.41	4.9	3.05	3.01	4.01	4.28	2.77	3.65
K2O	2	2.17	1.99	1.62	2.05	4.63	2.03	2.06	2.62	2.06	0.97
P2O5	0.52	0.43	0.42	0.3	0.17	0.92	0.33	0.21	0.25	0.14	0.16
Volat.	1.11	0.96	0.78	0.92	0.39	2.06	1.92	0.97	0.49	0.98	0.54
Total	99.28	99.18	99.08	99.06	99.42	99.39	99.48	99.31	99.21	99.52	99.55
Rb	32	108	112	46	44	133	60	55	47	66	15
Ba	2290	906	927	1050	2100	2220	1180	1000	1720	1700	566
Pb	8	9	8	8	8	34	8	11	10	9	8
Sr	1000	968	1120	716	890	952	382	836	888	353	598
La	32	66	62	26	36	68	30	21	44	21	17
Ce	69	126	109	56	62	129	62	44	80	38	31
Nd	36	51	40	31	24	66	31	23	33	16	12
Y	23	15	9	19	6	36	26	14	8	11	5
Th	0	8	8	2	6	18	4	5	4	2	3
Zr	156	159	118	163	104	132	118	72	125	354	73
Hf	4.9	4.7	0	4.1	2.5	0	0	0	3.6	10.1	0
Nb	8.8	9.8	11	6.4	5.6	14	11	4.6	6	12	2.4
Zn	97	75	63	87	42	117	118	80	45	75	68
Cu	46	26	20	16	4	42	32	11	26	36	12

Ni	13	44	21	18	9	13	44	14	14	28	10
Sc	23	11	6	15	3	14	38	18	5	16	5
V	192	87	80	112	31	152	287	121	48	181	61
Cr	21	72	25	53	14	7	177	28	26	79	32
Ga	19	22	21	20	16	20	18	17	19	16	18

Table 19: Element data for the Atâ Granites and associated grey dykes (Kalsbeek et al., 1988).

	Atâ Granite1	grey dyke 1	Atâ Granite2	grey dyke 2	Atâ Granite 3	Atâ Granite 4	grey dyke 3	Atâ Granite 5
SiO2	67.27	70.32	70.86	69.4	71.33	72.08	68.52	68.3
TiO2	0.47	0.38	0.26	0.24	0.28	0.22	0.43	0.26
Al2O3	16.26	15.25	15.13	16.39	14.96	14.74	15.76	16.73
Fe2O3*	0.81	0.58	0.54	0.58	0.49	0.25	0.81	0.72
FeO	2.3	1.8	1.51	1.25	1.43	1.3	1.87	1.24
MnO	0.05	0.03	0.04	0.04	0.04	0.03	0.04	0.04
MgO	1.06	0.81	0.66	0.64	0.6	0.45	0.94	0.56
CaO	3.41	3.15	3	3.08	2.68	2.28	3.16	2.59
Na2O	5.07	4.92	4.93	5.34	4.73	4.28	4.99	4.95
K2O	1.58	1.27	1.19	1.53	1.99	2.79	1.8	3.23
P2O5	0.15	0.12	0.1	0.09	0.09	0.08	0.12	0.09
Volatile	1.03	0.82	0.81	0.85	0.86	0.73	0.91	0.73
Total	99.45	99.45	99.03	99.43	99.47	99.22	99.35	99.44
Rb	54	46	53	52	56	65	57	99
Ba								
Pb								
Sr	471	297	448	404	431	373	415	445
La								
Ce								
Nd								
Y	10	5	6	7	7	6	7	11
Th								
Zr	163	183	119	98	104	91	146	113
Nb								

Zn								
Cu								
Ni								
Sc								
V								
Cr								
Ga								

Table 20: Element data for the Atâ Granites and Atâ Tonalites (Kalsbeek et al., 1988; Kalsbeek & Skjernaa, 1999).

	Atâ Granite 6	Atâ Granite 7	Atâ Tonalite 1	Atâ Tonalite 2	Atâ Tonalite 3	Atâ Tonalite 4	Atâ Tonalite 5
SiO2	70.77	69.49	61.41	66.68	69.84	70.45	72.36
TiO2	0.3	0.35	0.54	0.44	0.39	0.33	0.23
Al2O3	14.98	15.2	18.62	15.76	15.25	14.85	14.84
Fe2O3*	0.55	0.7	4.7	3.82	2.96	2.51	1.96
FeO	1.59	1.7					
MnO	0.03	0.05	0.05	0.05	0.03	0.03	0.02
MgO	0.66	0.79	1.83	1.57	1.02	0.75	0.55
CaO	2.79	2.85	5.78	4.07	3.29	2.81	2.33
Na2O	4.81	4.65	5.29	4.32	4.62	4.62	4.61
K2O	1.86	2.16	0.66	1.38	1.36	1.86	2.36
P2O5	0.11	0.11	0.17	0.13	0.12	0.08	0.06
Volatile	0.89	1.18					
Total	99.33	99.23					
Rb	43	52	16	37	38	56	57
Ba			266	402	510	562	866
Pb			7	8	9	13	9
Sr	407	426	603	460	478	407	370
La			14	21	21	20	19
Ce			36	40	42	36	33
Nd			19	17	15	16	15

Y	5	7	10	9	8	10	6
Th			3	7	7	8	6
Zr	132	111	79	121	155	133	120
Nb			2.1	3.9	3.4	4.8	3.1
Zn			62	68	65	63	54
Cu			55	10	9	14	5
Ni			16	14	5	5	4
Sc			10	6	3	3	2
V			77	54	35	28	20
Cr			26	15	8	7	8
Ga			21	19	19	19	18

11.2. Thin sections.

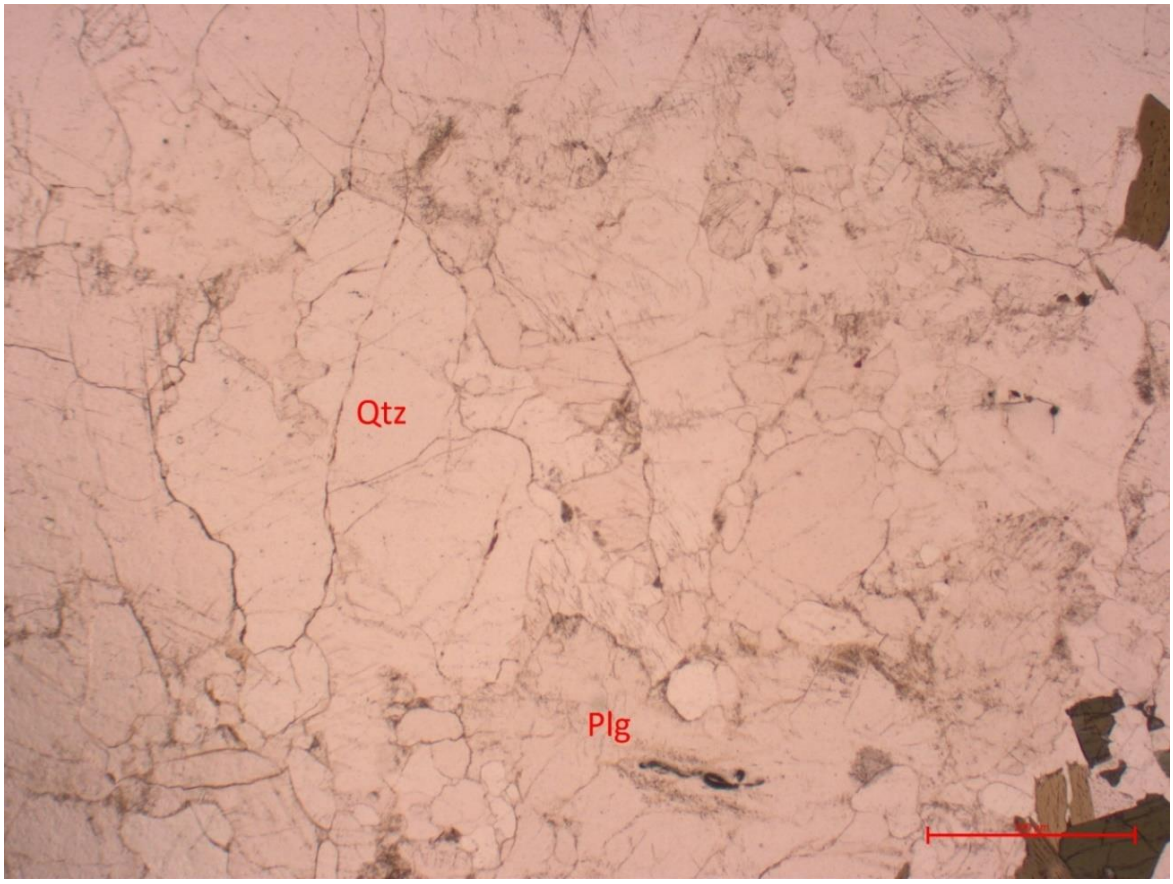

Figure 40: Thin section cutout of EK-1 under non-polarised light, exported from ZEN 3.5.

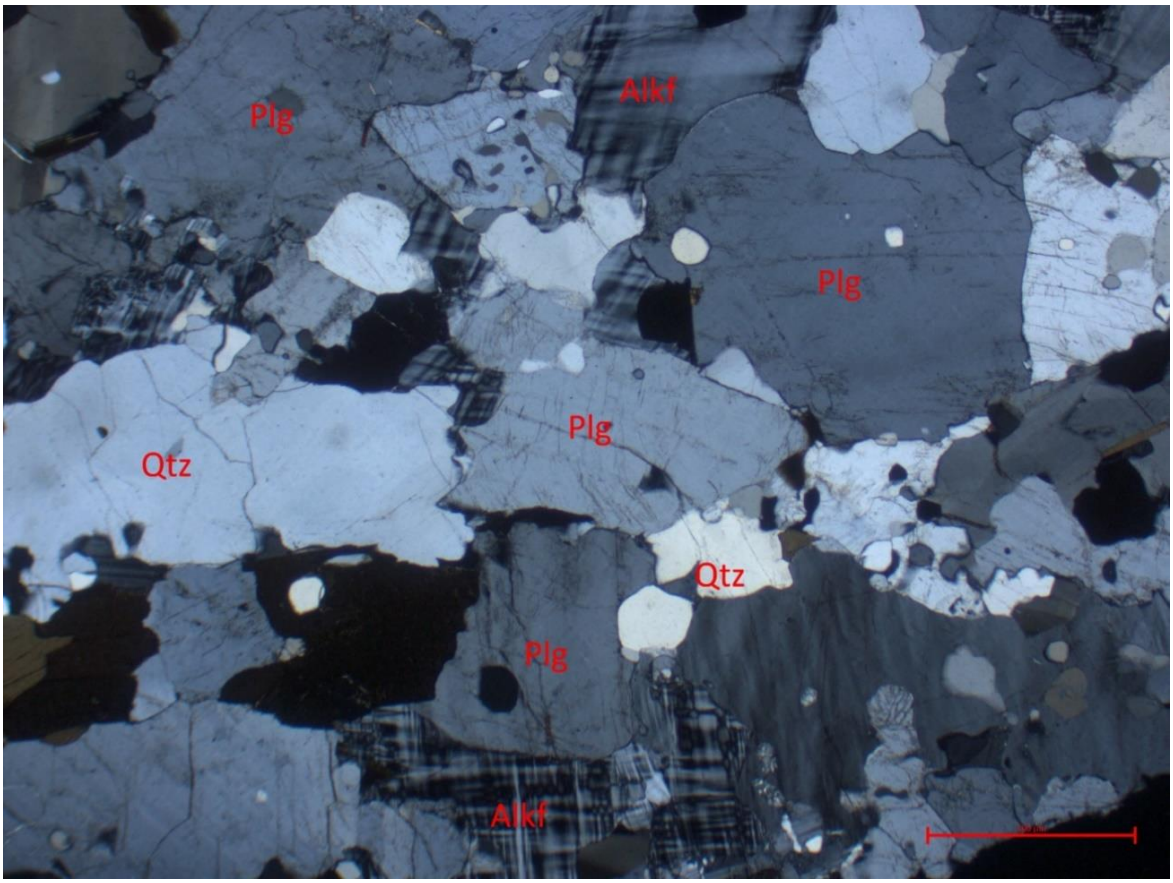

Figure 41: Thin section cutout of BO-2 under cross-polarised light, exported from ZEN 3.5.

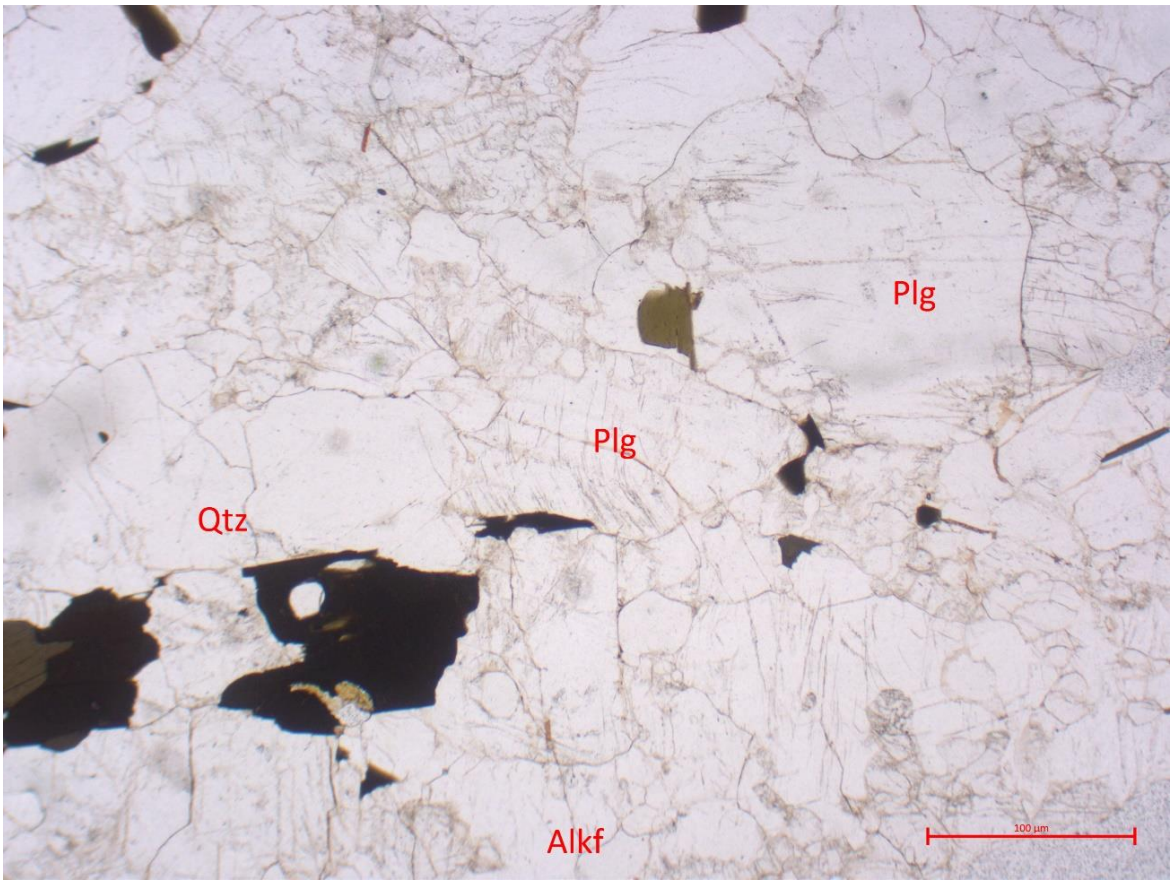

Figure 42: Thin section cutout of BO-2 under non-polarised light, exported from ZEN 3.5

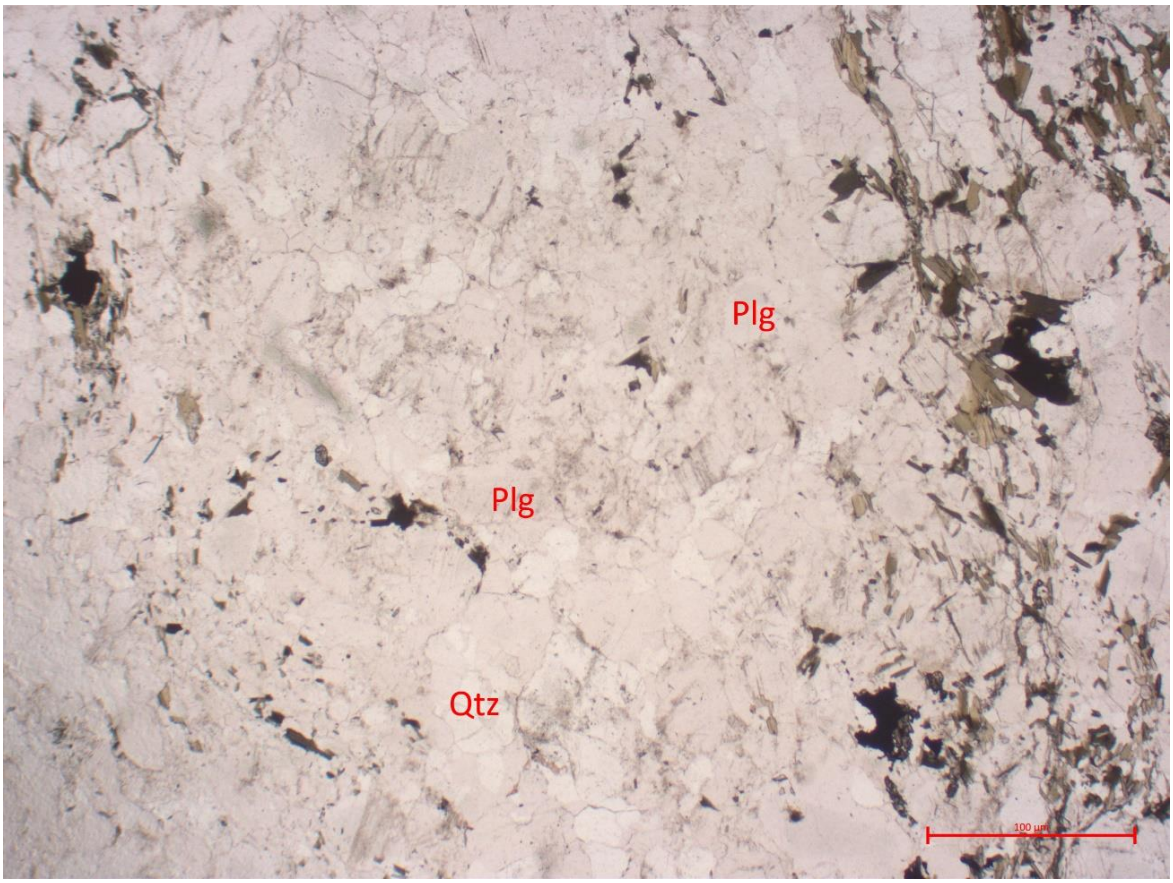

Figure 43: Thin section cutout of BO-4 under non-polarised light, exported from ZEN 3.5.

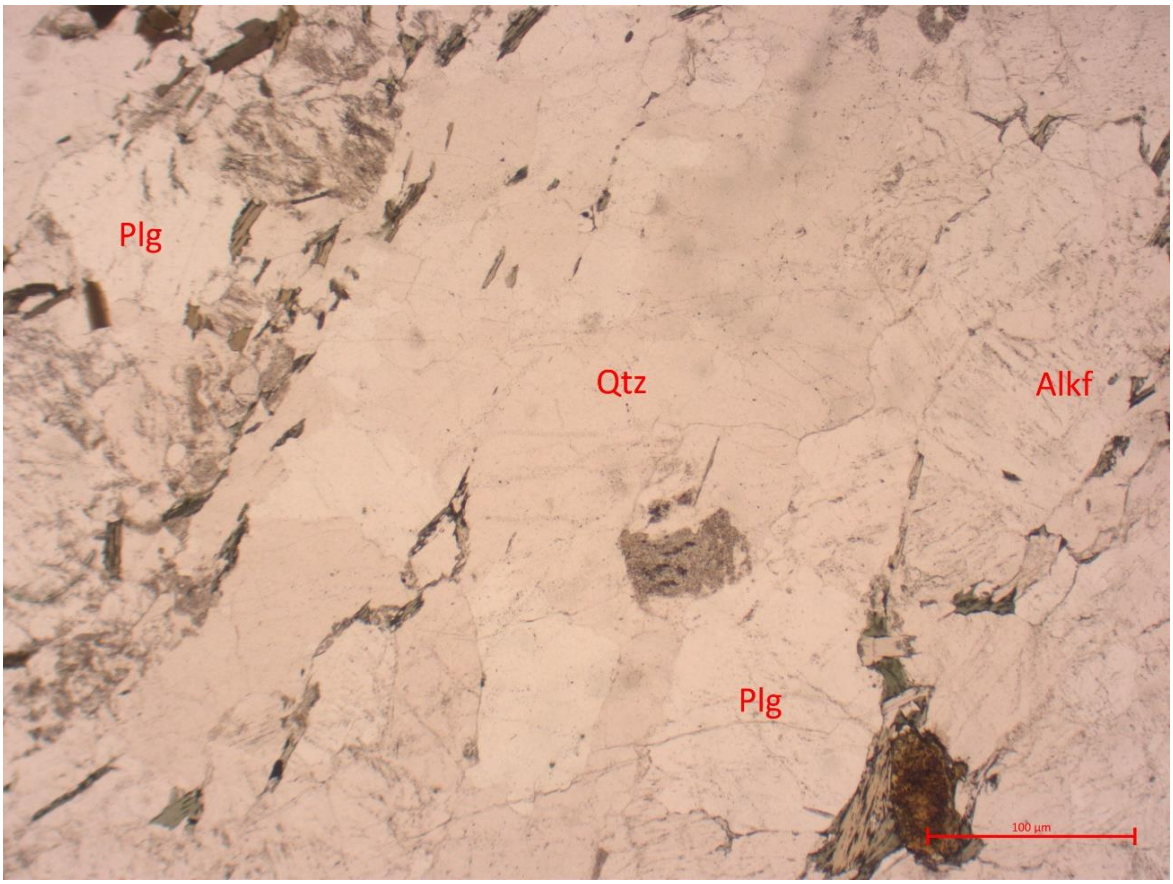

Figure 44: Thin section cutout of EB-45 under non-polarised light, exported from ZEN 3.5.

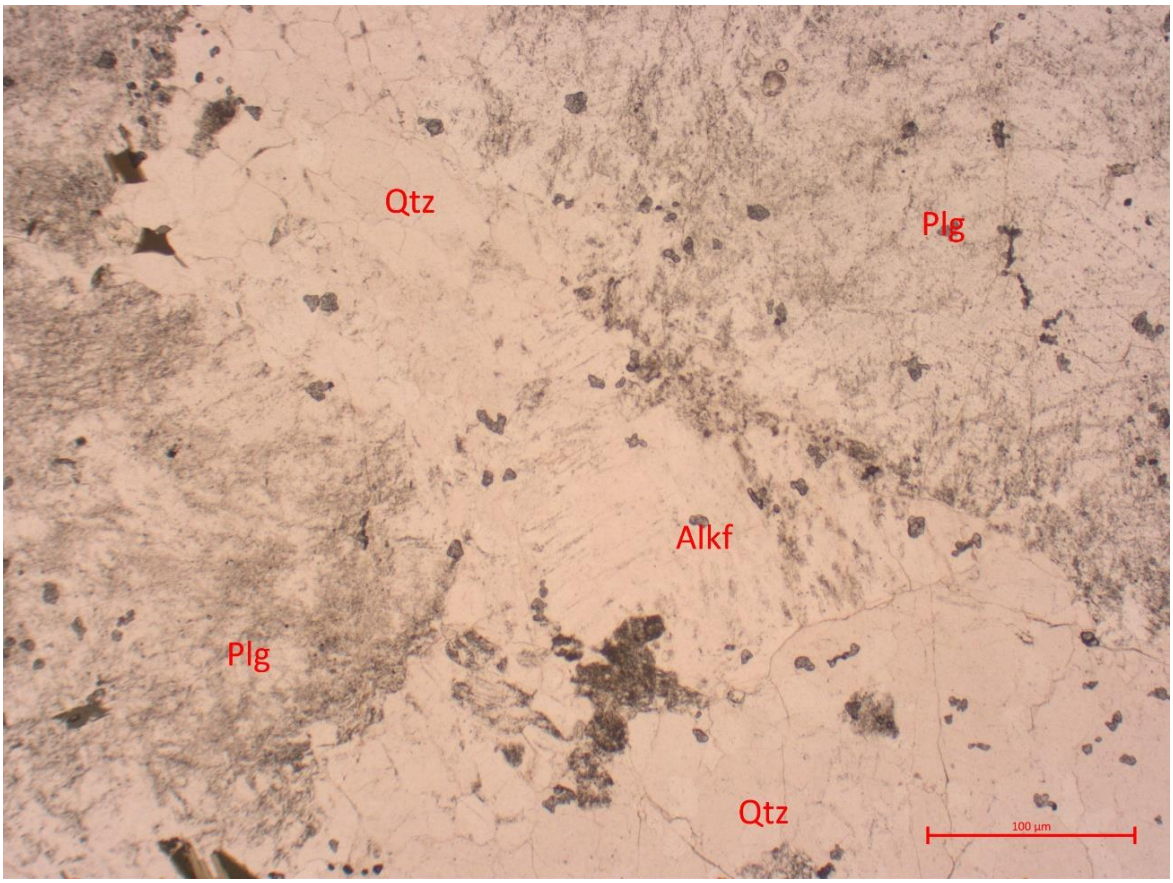

Figure 45: Thin section cutout of EB-25 under non-polarised light, exported from ZEN 3.5.

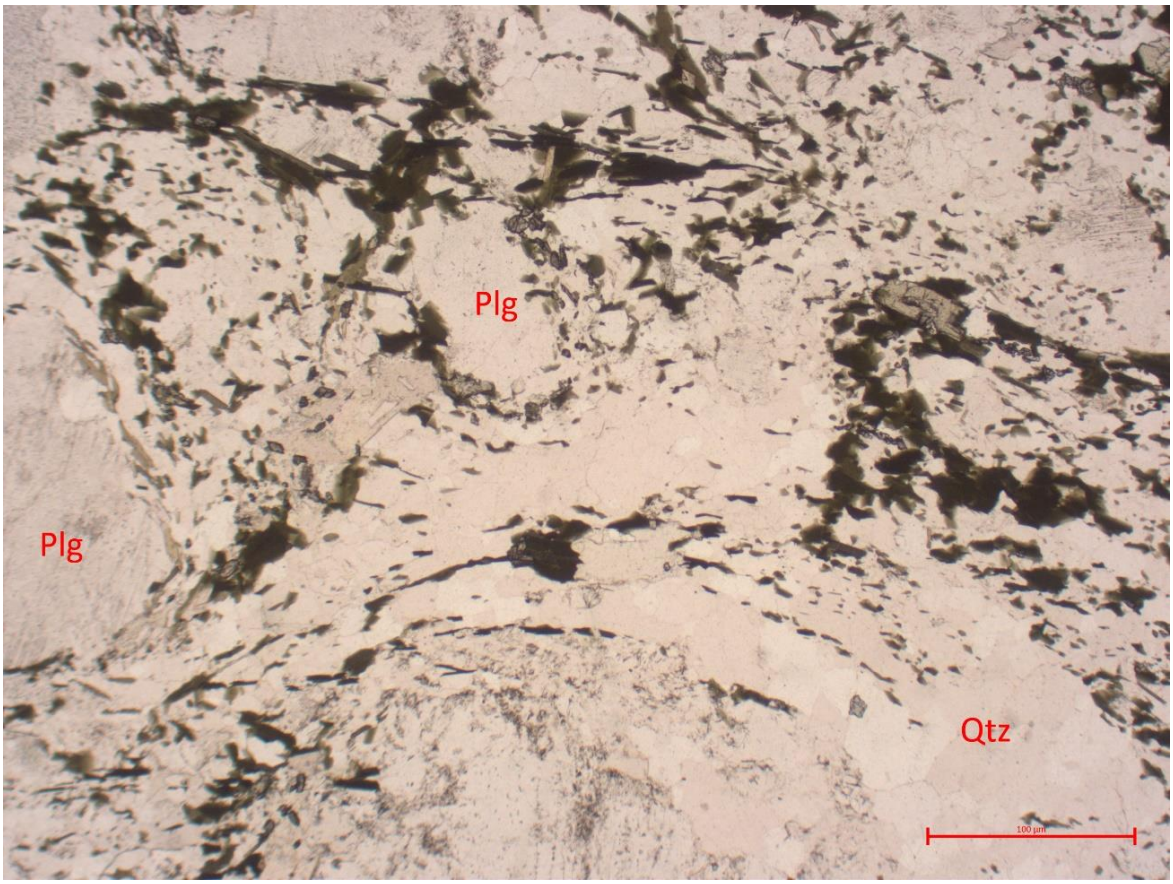

Figure 46: Thin section cutout of EB-1 under non-polarised light, exported from ZEN 3.5.

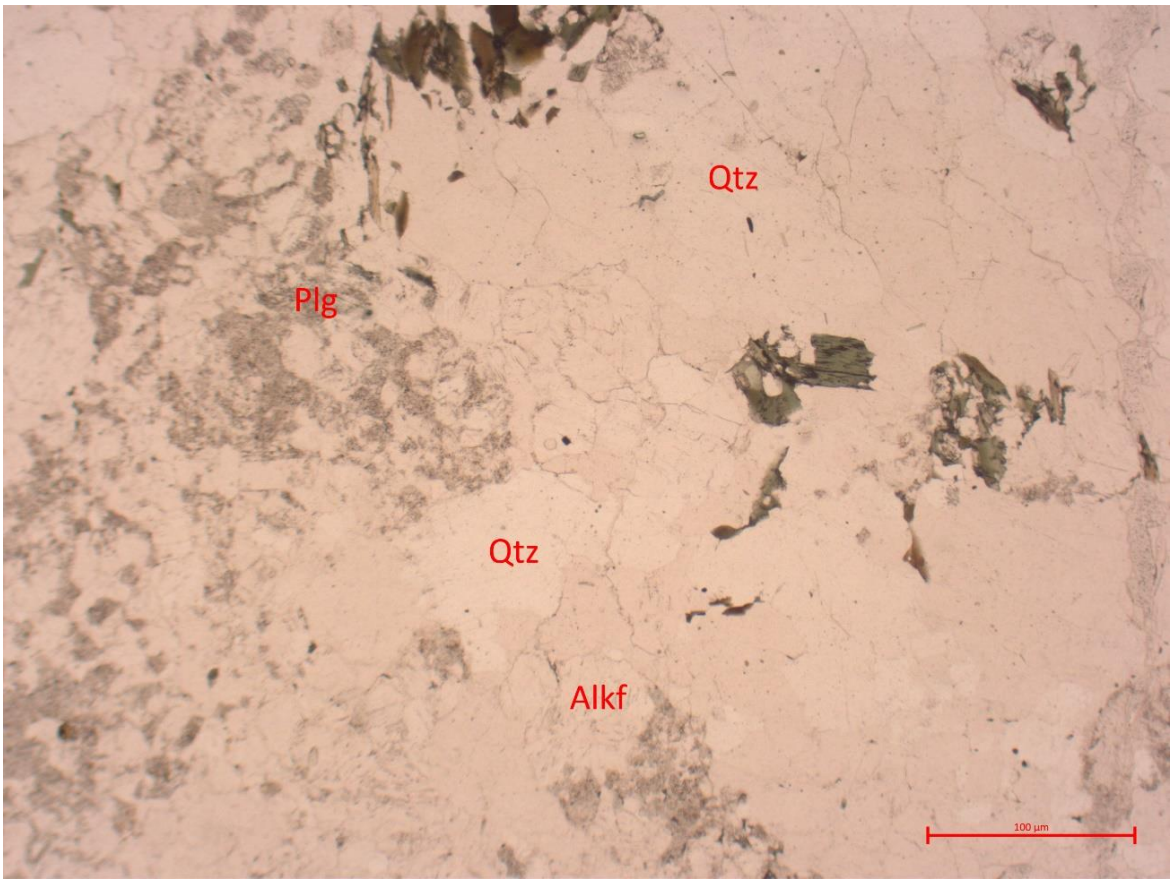

Figure 47: Thin section cutout of EB-97 under non-polarised light, exported from ZEN 3.5.

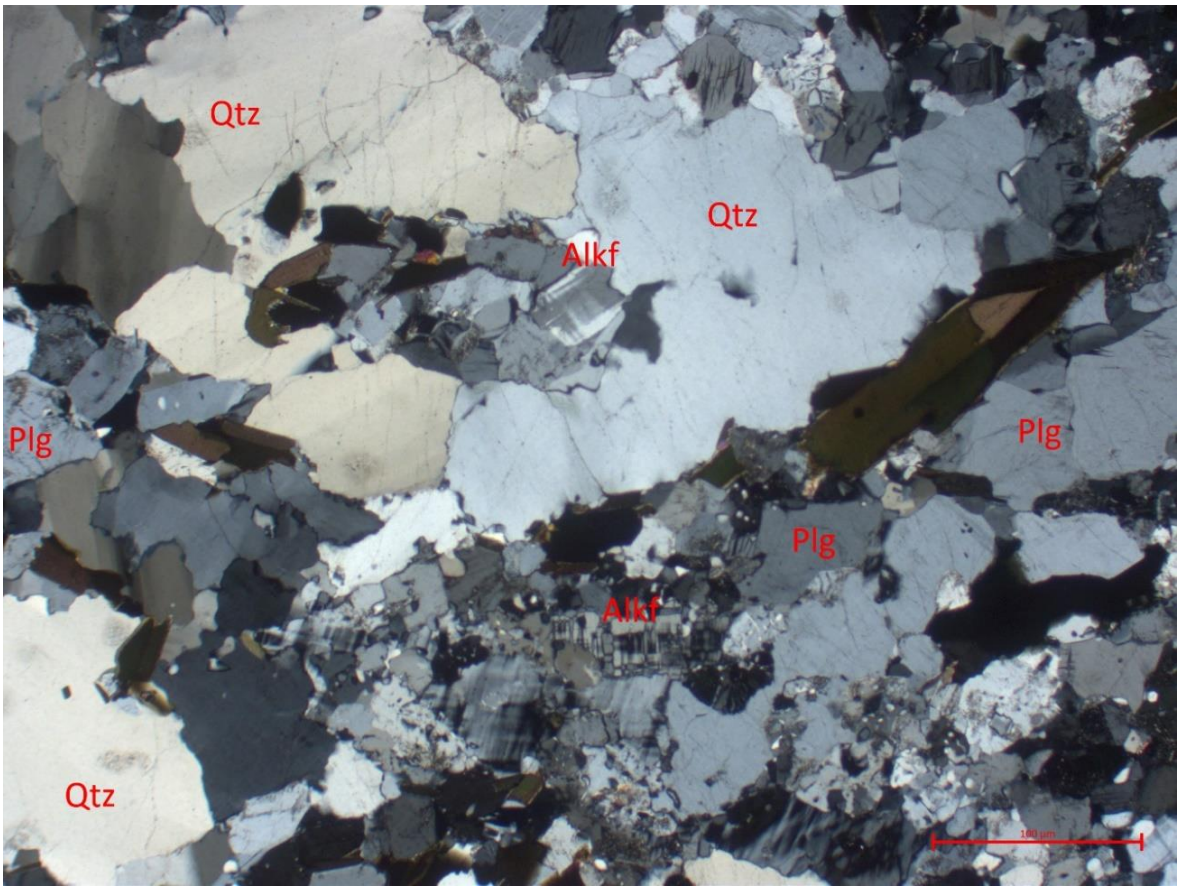

Figure 48: Thin section cutout of EB-19 under cross-polarised light, exported from ZEN 3.5.

Table 21: Estimation of mineral contents for optical classification.

Sample	Qtz (%)	Plg (%)	Alkf (%)	Mica (%)	Notes	Classification
BO-2	35	35	25	5		Granite
BO-4	45	45	5	5		Granodiorite
EB1	35	55	0	10		Tonalite
EB113	45	40	10	5		Granodiorite
EB144	30	30	30			Granite
EB151	42	42	5	10		Tonalite
EB167	50	25	25			Granite
EB19	45	20	30	5		Granite
EB190	30	70				Tonalite
EB195	50	40		10		Tonalite
EB25	30	40	20	10		Granodiorite
EB250	45	30	20	5		Granite
EB253	40	30	20	10		Granite
EB45	45	25	30			Granite
EB55	45	55				Tonalite
EB59	35				unidentified Matrix	
EB60	40	45	5	10		Tonalite
EB65	50	50				Tonalite
EB83	47	47	5			Tonalite
EB95					Plg and unidentified Matrix	
EB97	35	40	25			Granite
EB98	40	25	15		unidentified Matrix	
EK1	45	20	35			Granite

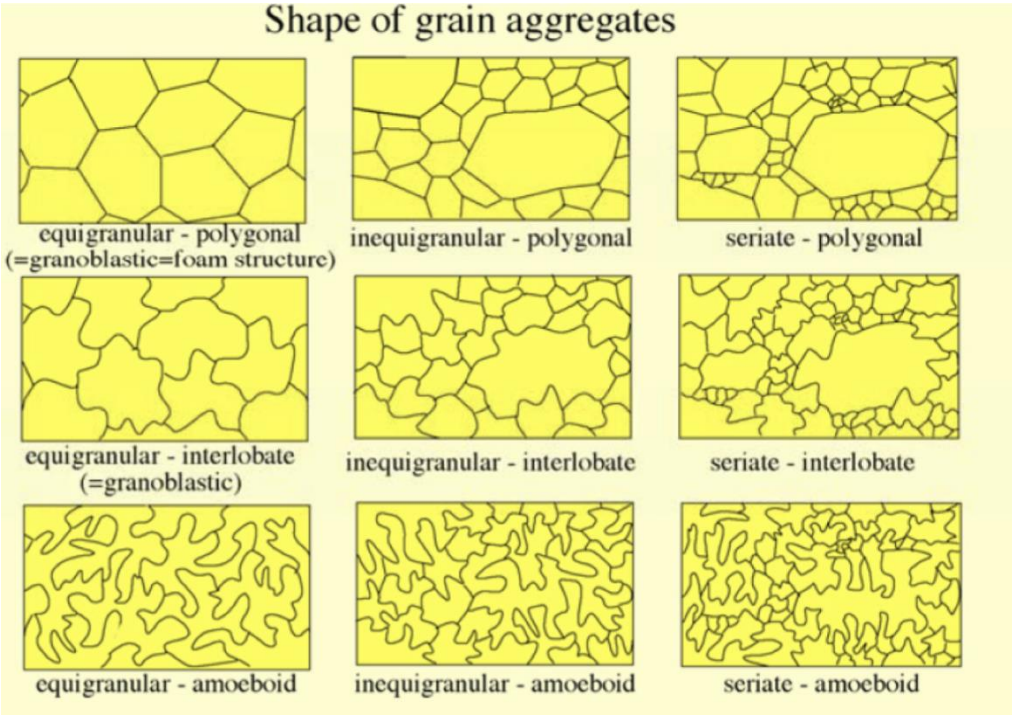

Figure 49: Different shapes of grain aggregates sent to me by Gerald Raab.

11.3. Tables from laboratory

Table 22: Tables from laboratory steps for ^{10}Be extraction.

	Owner/Project/Organization/Date:	Sebastian Schaffner						Batch 1	^{10}Be & ^{26}Al
#	Field sample name	Lab sample name	1. Mass of raw sample , g	1. Thickness of sample, cm	1. Mass after sieving, g	5. Mass before Aqua Regia, g	9. Mass after Aqua Regia, g	10. Mass before flotation, g	14. Mass after flotation, g
1	EB-190	RSG-1	2640	1.500	460.000	400.000	367.000		70.00000
2	EB-195	RSG-2	1677	2.000	550.000	400.000	356.000		75.00000
3	EB-167	RSG-3	1440	2.000	485.000	400.000	359.000		85.00000
4	EB-156	RSG-4	2385	1.750	645.000	400.000	364.000		93.00000
5	EB-151	RSG-5	1580	2.000	490.000	400.000	358.000		92.00000
6	EB-144	RSG-6	1750	2.500	510.000	400.000	365.000		75.00000
7	EB-55	RSG-7	1460	2.000	413.000	400.000	339.000		63.00000
8	EB-98	RSG-8	1830	3.000	462.000	400.000	272.000		214.00000
9	EB-95	RSG-9	2270	1.750	575.000	400.000	316.000		93.00000

	Owner/Project/Organization/Date:	Sebastian Schaffner						Batch 2	^{10}Be & ^{26}Al
#	Field sample name	Lab sample name	1. Mass of raw sample , g	1. Thickness of sample, cm	1. Mass after sieving, g	5. Mass before Aqua Regia, g	9. Mass after Aqua Regia, g	10. Mass before flotation, g	14. Mass after flotation, g
11	EB-19	RSG-10	2579	1.750	494.000	400.000	347.000		72.00000
12	EB-1(3)	RSG-11	2304	2.250	437.000	400.000	350.000		41.00000
13	EB-250	RSG-12	1907	2.000	497.000	400.000	369.000		80.00000
14	EB-253	RSG-13	1971	2.000	594.000	400.000	357.000		64.00000
15	EK-1 Drum	RSG-14	3240	2.000	465.000	400.000	339.000		72.00000
16	Bo-2	RSG-15	2500	2.000	490.000	400.000	333.000		60.00000

	Owner/Project/Organization/Date:	Sebastian Schaffner						Batch 1	^{10}Be & ^{26}Al
	Be carrier name & lot:			Concentration, g/l			Density, g/cm3		
#	Field sample name	Lab sample name	15. Mass before HF leaching, g	29. Mass after HF leaching, g	31. Mass of quartz before digest, g	32. Mass of carrier, g	Mass of 9Be, mg	43. Mass of residue after digest, g	Mass of digested quartz, g
1	EB-190	RSG-1	70	50.900	30.222	0.3042			30.222
2	EB-195	RSG-2	75	55.000	30.050	0.3053			30.050
3	EB-167	RSG-3	85	63.400	30.106	0.3036			30.106
4	EB-156	RSG-4	93	68.100	30.238	0.3038			30.238
5	EB-151	RSG-5	92	67.500	30.291	0.3017			30.291
6	EB-144	RSG-6	75	55.400	30.056	0.3045			30.056
7	EB-55	RSG-7	63	44.600	30.050	0.3044			30.050
8	EB-98	RSG-8	91	66.800	30.339	0.3045			30.339
9	EB-95	RSG-9	93						0.000
10	Be Blank 28	BI28				0.3054			

	Owner/Project/Organization/Date:	Sebastian Schaffner						Batch 2	^{10}Be &^{26}Al
	Be carrier name & lot:			Concentration, g/l			Density, g/cm3		
#	Field sample name	Lab sample name	15. Mass before HF leaching, g	29. Mass after HF leaching, g	31. Mass of quartz before digest, g	32. Mass of carrier, g	Mass of 9Be, mg	43. Mass of residue after digest, g	Mass of digested quartz, g
11	EB-19	RSG-10	72	52.800	30.119	0.3027			30.119
12	EB-1(3)	RSG-11	41	26.900	26.890	0.3038			26.890
13	EB-250	RSG-12	80	56.600	30.114	0.3043			30.114
14	EB-253	RSG-13	64	44.800	30.095	0.3043			30.095
15	EK-1 Drum	RSG-14	72	50.800	30.129	0.2995			30.129
16	Bo-2	RSG-15	60	44.700	30.050	0.3055			30.050
17	Be Blank 29	BI29							

	Owner/Project/Organization/Date:	Sebastian Schaffner						Batch 1	^{10}Be &^{26}Al
	Al carrier name & lot:			Concentration, g/l		Density, g/cm3		Mass, g	
#	Field sample name	Lab sample name	Mass of sample in 6M HCl + residue, g	Mass of aliquot for ICP-MS, g	Mass of aliquote in 20% HNO3, g	Additional dilution factor	ICP-MS Al concentration, ppm	ICP-MS Al concentration error, %	Mass of natural Al, mg
1	EB-190	RSG-1	21.5692	0.222	5.773				
2	EB-195	RSG-2	21.5245	0.221	5.774				
3	EB-167	RSG-3	21.6032	0.219	5.770				
4	EB-156	RSG-4	21.6137	0.219	5.745				
5	EB-151	RSG-5	21.714	0.221	5.754				
6	EB-144	RSG-6	21.6651	0.226	5.766				
7	EB-55	RSG-7	21.6543	0.219	5.737				
8	EB-98	RSG-8	21.6864	0.219	5.729				
9	EB-95	RSG-9							
10	Al Blank 28	BIAL28	21.5836	0.218	5.756				

	Owner/Project/Organization/Date:	Sebastian Schaffner						Batch 2	^{10}Be &^{26}Al
	Al carrier name & lot:			Concentration, g/l		Density, g/cm3		Mass, g	
#	Field sample name	Lab sample name	Mass of sample in 6M HCl + residue, g	Mass of aliquot for ICP-MS, g	Mass of aliquote in 2% HNO3, g	Additional dilution factor	ICP-MS Al concentration, ppm	ICP-MS Al concentration error, %	Mass of natural Al, mg
11	EB-19	RSG-10	21.7178	0.220	5.725				
12	EB-1(3)	RSG-11	21.7769	0.222	5.814				
13	EB-250	RSG-12	21.7056	0.220	5.771				
14	EB-253	RSG-13	21.6721	0.225	5.767				
15	EK-1 Drum	RSG-14	21.622	0.220	5.770				
16	Bo-2	RSG-15	21.699	0.221	5.762				
17	Al Blank 29	BIAL29							

Table 23: Raw result table from the AMS measurement.

user	pos	sample label	comment	^{10}Be counts	^{9}Be (LE) (nA)	Trans. (%)	^{10}Be/^{9}Be final (10^{-12})	error (%)	^{10}B (cps)	runtime (s)	carrier (mg)	weight (g)	^{10}Be (at/g) ($x10^{4}$)	err abs.	Comment (ETH)	Lab remarks
Egli	21	ZB8865	RSG-1	6,230	7052	40.1	1.608	1.5%	70	885.2	0.301	30.22	107.12	1.61		in-situ
Egli	22	ZB8866	RSG-2	1,926	5903	40.1	0.594	2.4%	36	885.5	0.302	30.05	39.92	0.94		in-situ
Egli	23	ZB8867	RSG-3	4,345	6777	40.0	1.171	2.1%	37	885.5	0.301	30.11	78.11	1.62		in-situ
Egli	24	ZB8868	RSG-4	1,088	5256	39.9	0.126	3.1%	131	2,654.7	0.301	30.24	8.40	0.26		in-situ
Egli	25	ZB8869	RSG-5	782	3792	40.2	0.125	3.6%	54	2,656.3	0.299	30.28	8.23	0.30		in-situ
Egli	27	ZB8870	RSG-6	794	6250	40.0	0.077	3.6%	102	2,655.2	0.302	30.05	5.18	0.19		in-situ
Egli	28	ZB8871	RSG-7	1,322	5460	40.3	0.094	3.2%	205	4,127.2	0.301	30.02	6.32	0.20		in-situ
Egli	29	ZB8872	RSG-8	907	5679	40.0	0.097	3.4%	254	2,652.4	0.302	30.32	6.47	0.22		in-situ
Egli	30	ZB8873	RSG-10	875	6184	40.0	0.086	3.4%	234	2,652.8	0.300	30.09	5.75	0.20		in-situ
Egli	31	ZB8874	RSG-11	799	3284	40.7	0.093	3.6%	32	4,132.6	0.301	26.87	6.99	0.25		in-situ
Egli	32	ZB8875	RSG-12	960	5997	40.0	0.097	3.3%	166	2,654.2	0.301	30.10	6.52	0.21		in-situ
Egli	34	ZB8876	RSG-13	753	3002	40.3	0.097	4.7%	132	4,129.5	0.301	30.10	6.51	0.30		in-situ
Egli	35	ZB8877	RSG-14	978	5935	40.1	0.100	3.2%	270	2,652.0	0.297	30.13	6.60	0.21		in-situ
Egli	36	ZB8878	RSG-15	910	5565	39.7	0.100	3.4%	149	2,654.5	0.303	30.05	6.75	0.23		in-situ
Egli	37	ZB8879	BI28	169	4231	40.4	0.016	9.3%	245	4,126.1	0.302	0.0003	104147.20	9672.30		in-situ, b

Table 24: LOI measurements and calculations at UZH.

Sample code:	RSG					
Lab code	Vial number	Sample name	Mass of vial [g]	Mass of sample [g]	Mass of sample + vial after ignition [g]	LOI (550 degr) [%]
276C22SS	*1*	276C22SS1	31.84392	2.00092	33.83931	0.28
	2	276C22SS2	27.79781	2.01435	29.80898	0.16
	3	276C22SS3	30.50586	2.00404	32.50379	0.30
	4	276C22SS4	33.24105	2.00791	35.23517	0.69
	5	276C22SS5	33.04203	2.02376	35.06224	0.18
	6	276C22SS6	32.92452	2.00239	34.92032	0.33
	7	276C22SS7	32.24268	2.01568	34.25017	0.41
	8	276C22SS8	33.24515	2	35.24271	0.12
	9	276C22SS9	29.14169	2.0128	31.1456	0.44
	10	276C22SS10	30.26	2.00067	32.20794	2.64
	11	276C22SS11	33.4687	2.00214	35.46212	0.44
	12	276C22SS12	32.04391	2.01504	34.0317	1.35
	13	276C22SS13	32.95219	2.0082	34.9559	0.22
	14	276C22SS14	31.95698	2.00637	33.95573	0.38
	15	276C22SS15	34.00808	2.0164	36.01982	0.23
	16	276C22SS16	32.58214	2.00723	34.5743	0.75
	17	276C22SS17	32.76428	2.02849	34.77836	0.71
	18	276C22SS18	32.29363	2.03024	34.3156	0.41
	19	276C22SS19	31.91965	2.00673	33.91695	0.47
	20	276C22SS20	32.2832	2.04994	34.32811	0.25
	21	276C22SS21	23.78138	2.0123	25.78638	0.36
	22	276C22SS22	20.60966	2.01306	22.61517	0.38
	23	276C22SS23	22.95721	2.01082	24.96118	0.34
	54	276C22SS24	22.97247	2.03378	25.00182	0.22
	25	276C22SS25	22.28823	2.05792	24.35048	-0.21
	26	276C22SS26	20.33266	2.02282	22.35068	0.24
	27	276C22SS27	21.9273	2.00253	23.90728	1.13

Personal Declaration

I hereby declare that the submitted thesis is the result of my own, independent work. All external sources are explicitly acknowledged in the thesis.

Zurich, 31.1.2023 Sebastian Schaffner